ADDRESSING PARTIAL VOLUME ARTIFACTS WITH QUANTITATIVE COMPUTED TOMOGRAPHY-BASED FINITE ELEMENT MODELING OF THE HUMAN PROXIMAL TIBIA

A Thesis Submitted to the College of

Graduate and Postdoctoral Studies

In Partial Fulfillment of the Requirements

For the Degree of Master of Science

In the Department of Mechanical Engineering

University of Saskatchewan

Saskatoon

By

Seyed Mehrdad Hosseini Kalajahi

PERMISSION TO USE

In presenting this thesis/dissertation in partial fulfillment of the requirements for a Postgraduate degree from the University of Saskatchewan, I agree that the Libraries of this University may make it freely available for inspection. I further agree that permission for copying of this thesis/dissertation in any manner, in whole or in part, for scholarly purposes may be granted by the professor or professors who supervised my thesis/dissertation work or, in their absence, by the Head of the Department or the Dean of the College in which my thesis work was done. It is understood that any copying or publication or use of this thesis/dissertation or parts thereof for financial gain shall not be allowed without my written permission. It is also understood that due recognition shall be given to me and to the University of Saskatchewan in any scholarly use which may be made of any material in my thesis/dissertation.

DISCLAIMER

Reference in this thesis/dissertation to any specific commercial products, process, or service by trade name, trademark, manufacturer, or otherwise, does not constitute or imply its endorsement, recommendation, or favoring by the University of Saskatchewan. The views and opinions of the author expressed herein do not state or reflect those of the University of Saskatchewan, and shall not be used for advertising or product endorsement purposes.

Requests for permission to copy or to make other uses of materials in this thesis/dissertation in whole or part should be addressed to:

Head of the Department of Mechanical Engineering
57 Campus Drive
University of Saskatchewan
Saskatoon, Saskatchewan S7N 5A9
Canada

OR

Dean
College of Graduate and Postdoctoral Studies
University of Saskatchewan
116 Thorvaldson Building, 110 Science Place
Saskatoon, Saskatchewan S7N 5C9
Canada

ABSTRACT

Quantitative computed tomography (QCT) based finite element modeling (FE) has potential to clarify the role of subchondral bone stiffness in osteoarthritis. The limited spatial resolution of clinical CT systems, however, results in partial volume (PV) artifacts and low contrast between the cortical and trabecular bone, which adversely affect the accuracy of QCT-FE models. Using different cortical modeling and partial volume correction algorithms, the overall aim of this research was to improve the accuracy of QCT-FE predictions of stiffness at the proximal tibial subchondral surface.

For Study #1, QCT-FE models of the human proximal tibia were developed by (1) separate modeling of cortical and trabecular bone (SM), and (2) continuum models (CM). QCT-FE models with SM and CM explained 76%-81% of the experimental stiffness variance with error ranging between 11.2% and 20.2%. SM did not offer any improvement relative to CM. The segmented cortical region indicated densities below the range reported for cortical bone, suggesting that cortical voxels were corrupted by PV artifacts. For Study #2, we corrected PV layers at the cortical bone using four different methods including: (1) Image Deblurring of all of the proximal tibia (IDA); (2) Image Deblurring of the cortical region (IDC); (3) Image Remapping (IR); and (4) Voxel Exclusion (VE). IDA resulted in low predictive accuracy with R^2=50% and error of 76.4%. IDC explained 70% of the measured stiffness variance with 23.3% error. The IR approach resulted in an R^2 of 81% with 10.6% error. VE resulted in the highest predictive accuracy with R^2=84%, and 9.8% error. For Study #3, we investigated whether PV effects could be addressed by mapping bone's elastic modulus (E) to mesh Gaussian points. Corresponding FE models using the Gauss-point method converged with larger elements when compared to the conventional method which assigned a single elastic modulus to each element (constant-E). The error at the converged mesh was similar for constant-E and Gauss-point; though, the Gauss-point method indicated this error with larger elements and less computation time (30 min vs 180 min).

This research indicated that separate modeling of cortical and trabecular bone did not improve predictions of stiffness at the subchondral surface. However, this research did indicate that PV correction has potential to improve QCT-FE models of subchondral bone. These models may help to clarify the role of subchondral bone stiffness in knee OA pathogenesis with living people.

ACKOWLEDGEMENT

Many thanks to my family members in Iran for their patience and support.

I would like to thank my supervisor, Professor James D. Johnston, for the patient guidance, encouragement, and advice through this research. Without his support this thesis would not have been completed.

I acknowledge my colleagues and group members, especially Nima Ashjaee for bone biomechanics related discussions we had.

Thanks to my advisory committee members, Dr. Emily McWalter and Dr. Joel Lanovaz, for their guidance.

I am grateful to the University of Saskatchewan and the Department of Mechanical Engineering for supporting me financially during this journey.

DEDICATION

I dedicate this thesis to my parents for their support and encouragements.

TABLE OF CONTENTS

LIST OF TABLES

LIST OF FIGURES

LIST OF TERMS, ABREVIATION, AND SYMBOLS

TERMS	DEFINITION
Anisotropic	A material with different mechanical properties in different directions
Anterior	Located nearer the front part of the body
Apparent density	Bone specimen mass/ total bone specimen volume (g/cm^3)
Ash density	Bone ash mass/ total bone specimen volume (g/cm^3)
Axial	Oriented along the axis of body
Compact bone	The bone tissue which covers the outer shell of the skeleton
Cortical bone	Synonymous with compact bone
Distal	Situated away from the center of the body
E-BMD	Density-modulus equation
Endosteum	Connective tissue that covers the inner surface of the bony tissue
Ex-vivo	Experiment done on a tissue out of the natural environment
Fabric	A second rank tensor which quantifies the anisotropy of a porous structure (e.g., trabecular bone)
Fiducial	An object which is used as a point of reference in the imaging field
Gauss point	Element integration point used to derive the element stiffness matrix
Inferior	Situated nearer the lower part of the body
In-situ	A tissue situated in its original place
In-vitro	An experiment taking place outside a living organism
In-vivo	An experiment taking place inside a living organism
Isotropic	A material with identical mechanical properties in different directions
Lateral	Situated nearer the side part of the body
Medial	Situated nearer the middle part of the body
Orthotropic material	An anisotropic material which is symmetric with respect to three mutually orthogonal planes
Periosteum	Connective tissue which covers the bone outer surface
Posterior	Situated nearer the back part of the body
Sagittal	The plane which cuts the body into right and left portions
Structural stiffness	The extent to which an object resist deformation
Subchondral bone	Bone beneath cartilage
Superior	Located nearer the upper part of the body

Trabecular bone	A spongy bone which forms the inner volume of a bony structure
Trabeculae	The primary structural element of trabecular bone
Transverse	The plane which cuts the body into top and bottom portions

ABBREVIATIONS	DEFINITION
2D	Two dimensional
3D	Three dimensional
BM/TV	Bone mineral density (bone mineral mass/total volume)
BV/TV	Bone volume fraction (bone volume/ total volume)
BMD	Bone mineral density
$BMD_{corrected}$	Corrected BMD of a voxel
CT	Computed tomography
CT-TOMASD	Computed tomography topographic mapping of subchondral density
DA	Degree of anisotropy
E	Elastic modulus
ECM	Extracellular matrix
FE	Finite element
HA	Hydroxyapatite
HU	Hounsfield unit
IDA	Image deblurring all
IDC	Image deblurring cortical
IR	Image remapping
K_2HPO_4	Dipotassium phosphate
OA	Osteoarthritis
PMMA	Poly(methyl methacrylate)
PSF	Point spread function
PV	Partial volume
PVC	Polyvinylchloride
QCT	Quantitative computed tomography
QCT-FE	Quantitative computed tomography-based finite element
RMSE	Root mean squared error
RMSE%	Root mean squared error normalized to maximum measured stiffness
SD	Standard deviation
SM	Separate model
VE	Voxel exclusion
VOI	Volume of interest

SYMBOLS	DEFINITION
ρ	Density
ρ_{app}	Apparent density
ρ_{ash}	Ash density
ρ_{QCT}	K_2HPO_4 equivalent bone mineral density
σ	Width of point spread function
d_i	Distance between the target voxel and adjacent voxels inside the bone
E	Elastic modulus
F_e	Element load vector
g	Actual intensity profile
h	Point spread function
i	Non-blurred cortical bone intensity profile
k	Number of adjacent voxels used in inverse distance weighting interpolation
K_e	Element stiffness matrix
K_{FE}	Finite element-predicted structural stiffness
K_{EXP}	Experimentally measured *in-situ* stiffness
mm	Millimeter (length unit)
N	Newton (the unit for force)
N/mm	Newton/millimeter (the unit for structural stiffness)
p	Power of distance in inverse distance weighting interpolation
Pa	Pascal (the unit of stress)
R^2	Linear regression coefficient of determination
u	Coordinate in the image space
q_e	Element displacement vector

CHAPTER 1

1 INTRODUCTION

1.1 Overview

Osteoarthritis (OA) is a debilitating joint disease affecting 13 percent of Canadians, roughly half exhibiting knee OA [1]. The direct medical cost of arthritis and joint pain in the United States was estimated to be US$580.9 billion in 2011 [2]. The disease is characterized by non-uniform and progressive loss of articular cartilage in areas of increased load [3]. However, OA cannot be solely treated as a disease of cartilage as it affects other components of the joint such as ligaments, tendons and underlying subchondral bone [3, 4]. Although there is no clear treatment for OA, understanding the role of bone in disease progression can help us to better understand the etiopathogenesis of OA and possibly in reducing joint pain.

Bone undergoes various alterations during the course of OA, both morphologically and mechanically. Sclerosis of subchondral bone (e.g., increased thickness and density), the formation of marginal osteophytes and subchondral cysts, as well as micro-crack formation in the bone tissue are dominant changes to the subchondral bone during OA progression [5, 6]. Increased thickness and stiffness of the subchondral bone leads to more energy being transferred through cartilage which would elevate internal cartilage stresses and expedite disease progression [7, 8]. Altered mechanical and morphological properties of the subchondral bone might also distort joint mechanics and cause pain [9]. Findings, however, are controversial, with some studies showing that OA lowers the stiffness at the subchondral bone [10] while others believe there is no significant difference in the mechanical properties of the OA and healthy bone [11]. These findings are based on *in-vitro* cadaveric or animal studies, while *in-vivo* studies are required to be performed on living people to further validate proposed mechanisms with OA.

Non-invasive tools such as subject-specific finite element (FE) models have potential to be used clinically on living people to measure altered subchondral bone stiffness during disease progression. Quantitative computed tomography (QCT) is commonly used to provide information for subject-specific FE models. It is well-known that the reconstructed volume from QCT images provides reasonably accurate geometrical information for FE models [12-14]. CT linear attenuation coefficient (Hounsfield units, HU) can also be calibrated to bone mineral density

(BMD) using standard QCT phantoms and is linked to bone's elastic modulus (E) via empirical density-modulus relationships known as E-BMD equations [15-21]. The approach by which FE models are constructed from QCT images is known as QCT-FE modeling. The predictive accuracy of QCT-FE models depends on accurate modeling of cortical and trabecular bone. A global cutoff value has been commonly used in the literature to detect the cortical and trabecular boundary [22-27]. While a global threshold can separate cortical and trabecular tissue at the diaphysis and metaphysis, the approach fails at regions with a thin cortical shell where limited resolution of the CT image results in low contrast (i.e., low BMD difference) between the cortical and trabecular bone. Consequently, a small elastic modulus is often assigned at these regions, which can adversely affect the predictive accuracy of the QCT-FE model. Hence, it is necessary to develop an accurate framework for identifying and modeling cortical bone.

Thin laminar structures such as cortical bone are not depicted accurately in clinical CT image because of the limited spatial resolution associated with clinical CT systems (0.33 mm to 0.5 mm voxel size). The limited resolution of the CT image results in partial volume (PV) artifacts leading to thickness overestimation and intensity underestimation [28, 29]. It has been shown that structures below 2.5 mm thickness are depicted entirely inaccurate in CT images [30] with errors exceeding 100% for sub-millimeter cortices [31]. The PV-affected bone appears as blurred edges in CT images and results in low contrast between the cortical and trabecular bone. As mentioned earlier, application of straightforward techniques such as a global threshold or half maximum height method (i.e., the 50% intensity across the cartilage and bone) [29, 32] are unreliable when the cortical thickness is low in relation to the imaging resolution. The application of semi-automatic segmentation with manual correction and separate modeling of cortical and trabecular bone might better visualize the cortical bone but will not restore intensity information at the blurred image. The corrupted PV layer indicates intensities below the range reported for cortical bone [33]. Consequently, when developing an FE model, this will result in an E which is equivalent to soft-tissue or low-density trabecular bone. Accordingly, methods are required to retrieve intensity information at the corrupted PV layer. This would make it possible to use straightforward tissue-separation techniques (e.g., threshold-based methods) and would enhance QCT-FE models of laminar-shaped thin cortical structures.

A primary step in QCT-FE modeling of long bones is to map elastic moduli at CT voxels on FE nodes and elements. This step is somewhat complicated and requires custom in-house codes.

The common approach with QCT-FE models is to assign a single elastic modulus to each element by integrating the elastic modulus field throughout tetrahedral or hexahedral elements [34]. Given the heterogeneity of bone tissue and large number of elements used to discretize bone geometry, assigning a single E for each element results in massive number of materials in the FE model which often makes FE solutions unattainable. Material binning is generally used to tackle this problem, where an elastic modulus is averaged over specific intervals. Binning results in another source of averaging within QCT-FE models which can adversely affect the predictive accuracy. A more efficient material assignment approach is required to account for spatial variation of elastic modulus over the element volume and eliminate the need for material binning.

The overall aim of my thesis is to enhance modeling of thin cortical structures at the human proximal tibia and to identify the modeling approach which best predicts *in-situ* stiffness measurements at the subchondral surface. The improved model might help clinicians and orthopedic researchers better understand the role of subchondral bone in OA initiation and progression and tailor potential treatment strategies.

1.2 Scope

Chapter 2 highlights the anatomy of the knee joint, literature related to the osteoarthritic knee, and QCT-FE modeling of long bones. In Chapter 3, research questions are outlined and objectives are defined. Chapter 4 presents a novel method for modeling cortical bone via semi-automatic segmentation with manual correction and separate modeling approach (SM). The results of SM are then compared to continuum-based methods (CM), and the best cortical modeling approach is identified in terms of the highest explained variance and lowest error in relation to experimental *in-situ* local stiffness measurements. Chapter 5 applies and compares different PV correction algorithms for restoring intensity information at the PV layer and identifies the best method in relation to experimental *in-situ* local stiffness measurements. In Chapter 6, the variation of elastic modulus within elements are taken into account using advanced QCT-FE material mapping strategies. The convergence of QCT-FE models is assessed by determining the average percent difference in stiffness between different mesh sizes. The model accuracy is assessed in terms of highest explained variance and lowest error in relation to *in-situ* local stiffness measurements. Limitations of this research and potential future work are outlined in Chapter 7.

CHAPTER 2

2 LITERATURE REVIEW

2.1 Functional anatomy of the knee joint

2.1.1 Knee joint

An anatomical view of the knee joint is shown in Figure 2-1. The knee is the largest and most complex joint in the body, comprised of three bony parts, namely: proximal tibia, distal femur, and patella. The joint has two articulations: one between femur and tibia and the other between femur and patella. The tibiofemoral joint is the most important joint in terms of load transfer, transmitting loads as high as nine times (human) body weight [35]. The proximal tibia frequently indicates OA symptoms (described in 2.2.1), and is the bone of interest for this study.

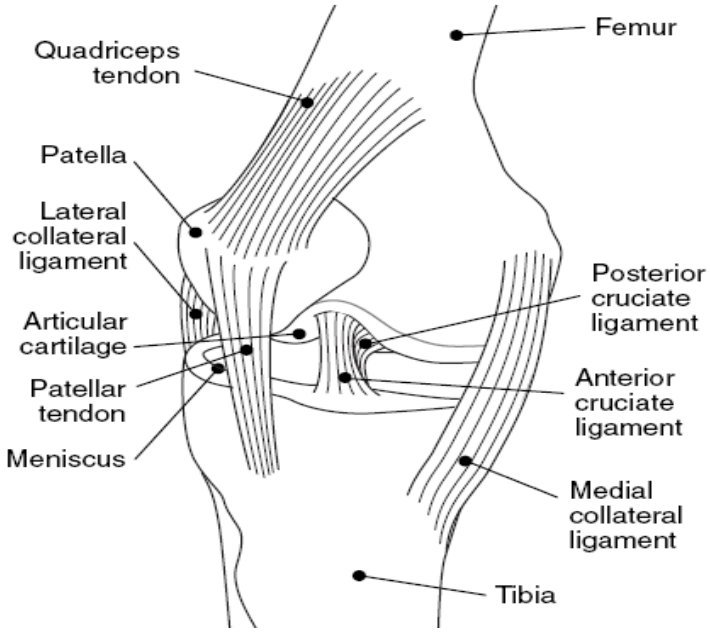

Figure 2-1. Functional anatomy of the knee joint. From Wikimedia Commons [36].

2.1.2 Articular cartilage

Cartilage is a connective tissue in the body which covers joint surfaces of the proximal tibia, distal femur as well as the posterior patella at the knee. It is a poroviscoelastic composite material which reduces friction in the joint and prevents direct contact between articulating bones. Articular

cartilage is comprised of a dense extracellular matrix (ECM) including proteoglycans (responsible for bearing compressive forces) and highly specialized cells called chondrocytes. The matrix is reinforced predominantly by type II collagen fibers which are responsible for bearing tensile and shear loads [37]. Together, these components retain water within the matrix and enable the cartilage to maintain its unique mechanical properties.

2.1.3 Subchondral bone

The bone underlying cartilage consists of five distinct layers (Figure 2-2) including: calcified cartilage, which is distinguishable from the overlying articular cartilage by the tide-mark; subchondral cortical bone with thickness of 0.01-3.3 mm [38-40], also known as the subchondral cortical endplate; subchondral trabecular bone, which is a spongy bone supporting the overlying subchondral cortical bone; and epiphyseal and metaphyseal trabecular bone which form the tibial epiphysis and metaphysis respectively. Mechanically, subchondral bone bends under dynamic impact loading and alongside the menisci helps in minimizing cartilage deflection and related internal stresses [41].

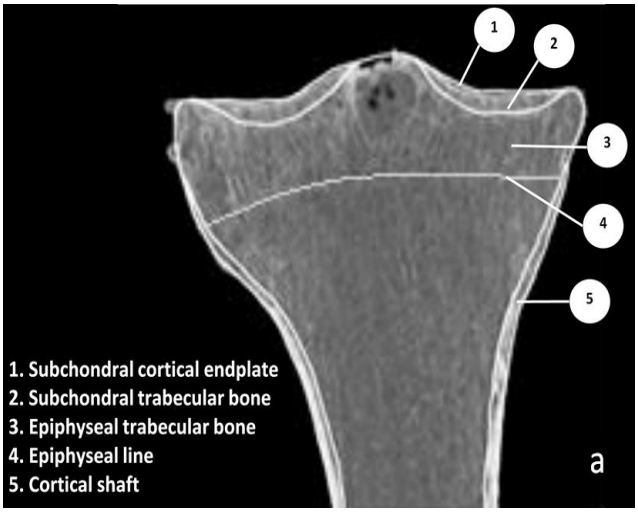

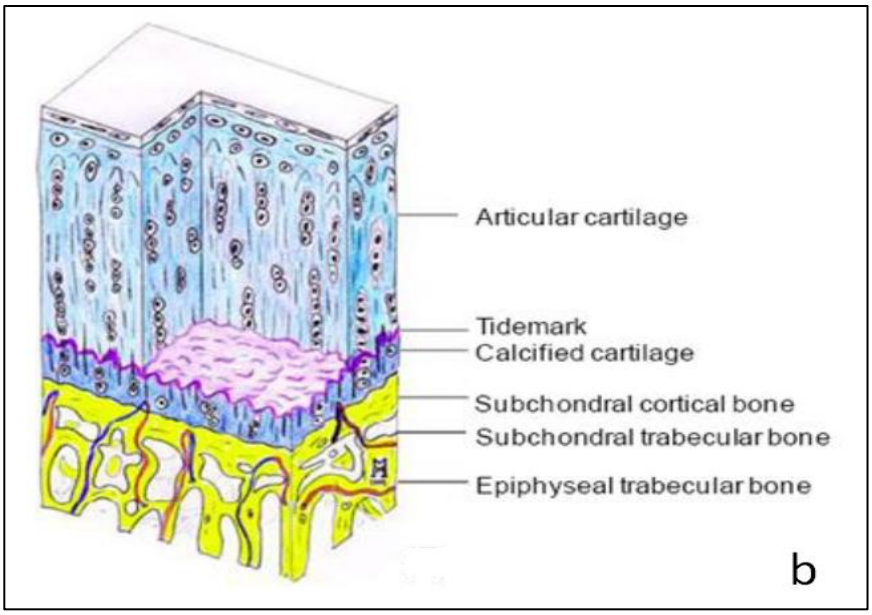

Figure 2-2. Sagittal CT image of the proximal tibia (a). Layers of the subchondral bone include subchondral cortical endplate, subchondral trabecular bone, epiphyseal and metaphyseal trabecular bone and the cortical shaft. Different layers of the cartilage-subchondral bone complex (b). Articular cartilage is distinguishable from the underlying calcified cartilage and subchondral bone by the tidemark. From Madry et al. [42] with permission from Springer.

2.2 Osteoarthritis

Osteoarthritis is a debilitating joint disease which affects both cartilage and subchondral bone. It is believed that the OA is the primary cause of pain and disability in the elderly [9, 43]. Clinically, the disease is characterized by several morphological alterations at the joint including joint

misalignment, tidemark advancement and associated cartilage thinning, altered subchondral bone thickness and stiffness, joint space narrowing and osteophytes formation [3, 4] (Figure 2-3). OA subchondral cortical and trabecular bone undergo severe structural and mechanical changes. There is increasing evidence that these alterations are associated with a change in bone turnover which results from the action of osteoblasts and osteoclasts continuously forming and removing bone [7, 11]. OA subchondral cortical and trabecular bone indicate altered bone volume fraction, tissue density, BMD and degree of anisotropy as well as different microstructural changes when compared to healthy bone [10, 11, 43-46].

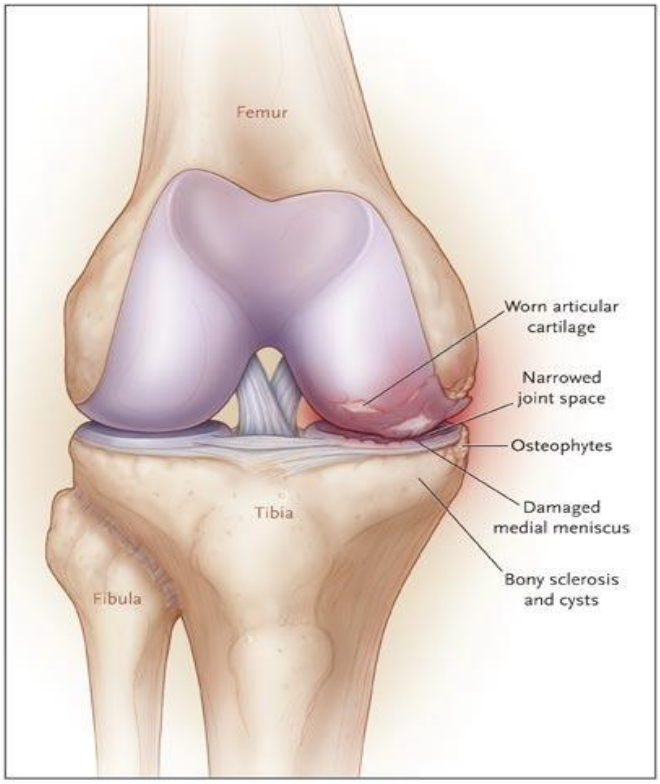

Figure 2-3. A schematic view of the osteoarthritic bone. Several morphological alterations are observed at the subchondral region. From Felson et al. [47]. Reproduced with permission from (scientific reference citation), Copyright Massachusetts Medical Society.

2.2.1 Osteoarthritic bone

To date, research on the etiology of OA has been primarily concentrated on articular cartilage deterioration. However, it is now evident that OA cannot be solely treated as a disease of cartilage as it affects other components of the joint such as subchondral cortical and trabecular bone [6, 7,

10, 48, 49]. Mechanical and microstructural alterations to bone, however, differ by the depth from the subchondral surface and the disease stage. While the OA subchondral endplate and subchondral trabecular bone indicate increased thickness, apparent density and bone volume fraction (bone volume divided by total specimen volume, BV/TV), epiphyseal bone located at a more distal region contains trabecula of lower density and thickness [10, 44]. The degree of mineralization at the bone tissue (bone mass divided by bone volume, BM/BV) is also affected by OA progression, resulting in hypo-mineralization (i.e., low mineralization) [5, 6]. The combined effect of these alterations often increases BMD (BMD = BM/TV = (BM/BV)(BV/TV)). BMD and microarchitectural parameters together have been shown to account for large variance in trabecular bone stiffness [50]. Hence, altered microarchitecture and BMD at the trabecular bone can eventually change bone stiffness at the subchondral surface. Overlying articular cartilage is a congruent material and its integrity is depended on mechanical properties of the subchondral bone. Increased stiffness and steep stiffness gradients at the subchondral bone can impose higher dynamic stresses on cartilage and expedite degeneration.

2.2.2 OA pathogenesis

The conventional research hypothesis regarding OA pathogenesis is that dynamic loading beyond normal physiological loads deteriorates chondrocytes and ECM at the cartilage. Prolonged loading is anticipated to further destroy cartilage, leading to complete cartilage loss and OA [51]. In this hypothesis, subchondral bone alterations are assumed to be secondary to OA. Conversely, more recent studies highlight the role of subchondral bone in OA progression. According to these theories, varied joint contact forces and load distribution at the subchondral surface in early OA alters bone turnover [3, 7, 8, 41]. Increased bone turnover is believed to be responsible for higher stiffness and thickness at the subchondral surface [7, 8]. The stiffened subchondral bone will be less able to deform, leading to the more energy being transferred through the cartilage. This may raise internal mechanical stresses at the cartilage and accelerate disease progression. The latter hypothesis, however, is based on *ex-vivo* animal studies and needs to be corroborated with *in-vivo* findings from living people.

2.3 Methods for assessing subchondral bone stiffness

2.3.1 *In-vitro* methods

2.3.1.1 Mechanical testing

The most common method to assess bone stiffness is mechanical testing. Excised cubic or cylindrical bone samples from the epiphyses or metaphysis are located between two platens in the material testing system to apply a tensile or compressive load [15-20, 52-54]. Uniaxial displacement is applied and read directly from the machine while the load cell measures the applied load. Stiffness is then calculated as the slope of the most linear region on the load-displacement curve. Stiffness measurement by mechanical testing, however, is not free from errors. In particular, the friction between platens and the specimen leads to increased shear stresses at the connective surface, which adversely affects measured bone stiffness. Also, reading the strain data from excised trabecular samples disconnected from the whole bone network indicate stiffness underestimation [21]. In addition, cutting and testing bone samples from the thin subchondral bone (thickness less than 5 mm [39]) is challenging and measured stiffness values from large trabecular samples do not represent net stiffness at the desired subchondral surface (the hallmark of OA).

2.3.1.2 Ultrasound

Application of ultrasound waves to measure bone elastic properties is well known [55-58]. Anisotropic elastic properties of the cortical and trabecular bone can be measured by monitoring the wave velocity/time propagating in a particular direction within the bone specimen. Ultrasonic techniques have been successfully used to derive cortical and trabecular bone orthotropic constants and has been shown to have several advantages over conventional mechanical testing [55]. The method has been applied to cylindrical or parallelepiped specimens as small as 5 mm for cortical and 10 mm for trabecular bone [55]. This makes it possible to measure stiffness from samples excised from the subchondral endplate and to study OA subchondral bone alterations. Also, a single specimen could be used to derive anisotropic properties rather than cutting and testing various samples excised from different anatomical directions. Even though using ultrasound to measure elastic properties of the cortical bone is quite straightforward, the porous structure of the trabecular bone makes it challenging to capture waves traveling through its complex network. Waves are attenuated within the porous structure, and a proper frequency setting is required to obtain meaningful values for the elastic properties of the trabecular tissue [55, 57]. Another

inherent drawback with this approach is its dependence on excised samples. Excised samples do not accurately represent mechanical properties of the tissue within the whole bone owing to the disconnected trabecular structure.

2.3.1.3 *In-situ* macro indentation

Stiffness measurements using compression tests and the ultrasound method are performed on excised bone samples from epiphyseal and metaphyseal regions located distally from the subchondral surface (greater than 5 mm) [15, 17, 54]. Hence, stiffness measurement with these methods do not represent actual stiffness at the subchondral surface which is most relevant to OA pathogenesis. *In-situ* macro indentation tests, on the other hand, can be directly performed at the subchondral surface to measure overall structural stiffness, which is more representative of the *in-vivo* condition between the bone and overlying articular cartilage. Macro indentation has been used in literature to measure stiffness from different articulating surfaces including the proximal tibia [59-63].

The destructive nature of these experiments prevents their application on living people. Hence, surrogate non-invasive tools are required to make *in-vivo* measurements from the subchondral bone in living people. *In-vivo* measurements might better elucidate the structural role of subchondral bone in initiation and progression of OA.

2.3.2 *In-vivo* methods

2.3.2.1 Imaging

Imaging techniques such as dual-energy X-ray absorptiometry (DXA) have been applied to investigate the relationship between imaged BMD and the severity of OA [64, 65]. More recently, measured volumetric BMD from computed tomography (CT) has been mapped on the joint surface via a depth-specific image processing tool (termed CT-TOMASD, computed tomography topographic mapping of subchondral density) [46]. As opposed to 2D techniques, the depth-specific approach measures complex three dimensional (3D) BMD from critically relevant regions including subchondral cortical and trabecular bone. Nonlinear power-law regression models resulted in relatively strong correlations between *in-situ* stiffness measurements at the subchondral cortical endplate with depth-specific measures of BMD to a depth of 2.5 mm beneath the subchondral surface, with R^2 between 65%-71% depending on the disease stage [60].

The depth-specific method measures BMD directly beneath the indentation site and neglects the contribution of adjacent regions on structural stiffness of the subchondral bone. This is important as trabecular orientation with respect to the applied load has also been shown to affect measured stiffness which is not accounted by measured BMD [43, 66]. Hence, other non-invasive tools are required to account for the exact geometry and heterogeneous mechanical properties of bone tissue.

2.4 Finite element (FE) modeling

2.4.1 Overview

The finite element (FE) method is a numerical approach used to calculate approximate solutions for differential equations. Physical processes can be formulated as boundary value problems using the system of differential equations alongside appropriate boundary and initial conditions. These equations are generally complex and cannot be solved analytically, with numerical methods needed to derive approximate solutions for desired field variables. FE analysis is a robust numerical method for obtaining such approximate solutions with reasonable accuracy. The principal step in FE modeling is to discretize the field of interest into small elements such that the solution in each segment is relatively traceable. The discretization procedure is known as meshing.

In structural mechanics, in order to guarantee that the elastic body is in equilibrium the total potential energy needs to be minimized with respect to the field variable (usually displacement). In other words, the extrema of the total potential energy characterize the state of equilibrium of the system. Total potential energy is the sum of elastic energy stored in the deformed body and the energy induced on the system by applied external loads. Minimizing the total potential energy means taking its derivative with respect to the displacement field. The derivation step is straightforward and is omitted here, but it can be shown that it results in the following algebraic equation which is the basis of the FE formulation.

$$K_e q_e = F_e$$

where K_e is known as the element stiffness matrix, q_e is nodal displacement and F_e is the load vector respectively. The same formulation is repeated for all elements within the discretized domain. Assembling stiffness matrices and load vectors will result in the final algebraic equation for the elastic body. Calculating the element stiffness matrix requires solving integral equations.

There exists various numerical methods to solve complicated integrals, among which the Gauss integration method is most commonly used within different FE packages. Once the global matrix is assembled, the stress and strain field can be calculated from the displacement degrees of freedom. Reducing the mesh size (h-method) or increasing the order of shape functions (p-method) will lead to more accurate approximations in expense of higher computation time.

FE analysis has been extensively used to investigate the mechanical response of biological tissues to external load. FE models can simulate the stress and strain field within the bone and are deemed as a potential clinical research tool (e.g., for assessing fracture risk, prosthetic design and to study bone adaption at the bone-implant interface [67-73]).

2.4.2 Generic FE modeling

Generic FE modeling of bone is constructed based on idealized geometry outlined from digitized control points in a QCT image or sketched estimated geometry using computer aided design (CAD) software. Homogenous material properties are often assigned to the whole model. Simplified heterogeneous models might also be constructed by partitioning the model into limited areas and/or volumes and assigning different material properties to each region. Generic FE models are relatively simple to implement and can be solved quickly, making them useful for parametric studies. Few studies have used this approach to simulate the stress and displacement state in the proximal tibia with response to tibiofemoral contact forces [61, 74]. Recently, Amini et al. [75] performed a parametric study to investigate OA-related mechanical and morphological alterations in different layers of the proximal tibia on overall stiffness of the subchondral bone. However, idealized geometry and simplified distribution of mechanical properties are inherent drawbacks associated with generic FE models. To address these limitations, more accurate subject-specific FE models are required to account for the complex geometry and inter- and intra-subject variation of mechanical properties within the bone.

2.4.3 QCT based finite element modeling

The advent of 3D imaging modalities such as QCT and more advanced FE techniques has made it possible to closely represent bone of an individual patient. So-called “subject-specific FE modeling” provides surgeons with new data (e.g., stress/strain distribution) and help them better interpret data obtained from QCT images, for example for fracture risk analysis [71, 76-84] or checking implant micro-motions [85-87]. As opposed to generic models, subject-specific FE models employ an individual patient’s bone geometry and material properties as well as the

physiological loading condition, which make this approach a potential clinical research tool. The geometry of the model can be directly acquired from segmented 3D images of bone tissue. For material definition, BMD at image voxels are first converted to apparent density via densitometric conversion equations [20, 88-90], then E-BMD relationships from the literature are used to calculate the elastic modulus for individual CT voxels. Finally, material properties are mapped to the FE model using in-house programs. More sophisticated QCT-FE models with orthotropic material properties might also be constructed using fabric-elasticity equations or a direct mechanics approach, where orthotropic constants are derived using micro-FE models of trabecular structures and the theory of homogenization [10, 91-101].

2.4.3.1 Image acquisition

An effective subject-specific FE model requires an accurate representation of bone geometry and mechanical properties. Clinical CT images with voxel size of 0.3-0.5 mm are the choice of interest to acquire this information. Most recent CT scanners are the helical type in which multi-row detectors register the x-ray attenuation of the beam emitted from the x-ray source. The x-ray source and the detector orbit simultaneously while the subject is translated in the longitudinal direction. Each detector records the "line integral" of the x-ray attenuation. The combined attenuation values from all detectors produce a projection plane at each rotation increment. The so-called sinogram image is formed from the projection planes produced after 180° rotation. The tomographic reconstruction is then used to construct the 3D image. The final image is the contrast map of different attenuation numbers known as grayscale values resulting from spatially variant material properties of the scanned object. Grayscale magnitudes are linearly scaled to Hounsfield (HU) units in which water has the value of 0 HU, and air has the value of -1000 HU. For subject specific FE modeling, HU values are then converted to BMD using a phantom with known BMD (discussed in 2.4.3.5). The change in CT protocols such as the type of scanner, tube voltage, tube current, integration time and image reconstruction algorithm will result in a statistically significant difference in grayscale values within the CT image, which can eventually alter assigned material properties to the FE model [20, 70, 89, 102, 103]. The reliability and repeatability of imaging protocols must be therefore ensured before constructing FE models.

2.4.3.2 Bone segmentation

Accurate representation of the cortical and trabecular bone is essential in FE modeling of skeletal structures. Segmentation of intricate bone profiles from the surrounding soft tissue is a challenging

step and might impose unpredictable errors that can propagate down to subsequent steps in model generation and mesh construction [70]. Further segmentation of the thin cortical bone from the inner trabecular tissue is more complicated, particularly in images with limited spatial resolution, where the low image contrast makes it challenging to delineate between the thin cortical shell and the trabecular bone. Several segmentation methods with various automation levels have been proposed in the literature, but uncertainty in the boundary definition always exists regardless of the selected approach [70]. Semi-automated threshold-based methods are commonly employed to separate bone from surrounding materials [23-27, 104, 105]. With this approach, a single threshold is used alongside a region growing algorithm [106] to separate bone from surrounding tissue and detect the cortical-trabecular boundary. Some methods such as half maximum height (HMH) have also been employed to identify the bone periosteal surface (i.e., bone outer profile) [29, 32, 46, 107]. The HMH defines a subject-specific threshold as the 50% intensity between the bone and cartilage. Even though successful in delineating between the outer bone profile and soft tissue, the HMH method is not able to identify the bone endosteal surface (i.e., cortical and trabecular boundary) due to the low contrast between the laminar cortex and inner trabecular bone. Consequently, straightforward threshold-based techniques are unreliable when the cortex is thin in relation to the image spatial resolution and generally result in unclosed profiles (Figure 2-4).

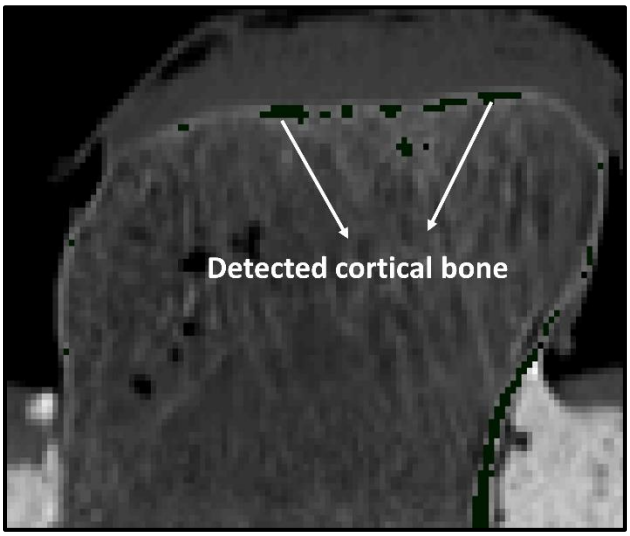

Figure 2-4. Visualized cortical region at the proximal tibial subchondral surface using a global threshold method. The BMD threshold of 550 mg/cm^3 was used to differentiate the cortex and trabecular bone, which resulted in incomplete separation of the subchondral cortical region.

Binary morphological operations (i.e., image erosion and Boolean subtraction) have been employed in the literature to improve the performance of threshold-based techniques [108]. The bone periosteal surface is first determined via the HMH or simple threshold method. The trabecular bone is then visualized with in-plane erosion of integral bone structure with a proper thickness. The cortex is subsequently identified with Boolean subtraction of trabecular tissue from the integral bone structure followed by a single global threshold. This approach may enhance the segmentation of cortical bone by restricting the cortex to the bone periphery, but the efficacy of this approach has not yet been evaluated in QCT-FE models of subchondral bone at the proximal tibia. Numerical methods such as the level-set approach have been recently introduced for fully-automated segmentation of bone periosteal and endosteal surface [14]. Numerical methods reduce human intervention and increase the segmentation repeatability. Nevertheless, these methods are still in the developing stage and require intricate parameter settings which can hinder their application in wider practice.

Various segmentation methods should be considered complementary rather than competitive and careful customization of existing algorithms is required to obtain effective methods. In this regard, one possible approach is to combine HMH, region growing and manual intervention methods (semi-automatic segmentation with manual correction) to determine cortical bone thickness. It is though unclear if using semi-automatic segmentation with manual correction can better distinguish the cortical and trabecular boundary at the subchondral region and enhance QCT-FE models of bone at joint ends.

2.4.3.3 Partial volume correction

QCT-FE estimates of local structural stiffness at the proximal tibia have been recently validated versus *in-situ* stiffness measurements at the subchondral surface [109, 110]. FE procedures yielded moderate correlations with measured subchondral bone stiffness (R^2 =54%-81%). Similar results were also obtained for FE-predicted femoral bone strength constructed from clinical QCT images and validated versus *in-vitro* strain measurements, with absolute errors as high as 1800 με [33, 67, 111-113]. This previous work noted that PV artifacts might be responsible for observed systematic and/or local errors. PV layers appear in areas with thin cortical bone, where the limited resolution of a CT system is unable to quantify the exact intensity of thin structures. The result is thickness overestimation and intensity underestimation for cortical bone such that intensity values at the cortical region are indistinguishable from surrounding soft tissue and inner trabecular bone [28,

29, 114-117]. Low-density cortical voxels in the QCT image will appear as low E elements in the FE model with values equal to soft tissue or low-density trabecular bone. Also, low density voxels create holes during the tissue segmentation stage, resulting in the broken boundary detection and an inaccurate model of cortical bone. Previous work revealed that structures with thickness below 2.5 mm are not properly presented in FE models [115].

Semi-automatic segmentation with manual correction and separate modeling of the cortical region might better distinguish the cortical structure, however, this method does not restore intensity information at the corrupted PV layer. In addition, manual segmentation is time-consuming and labor-intensive and might create biased results. To overcome this issue, thin shell elements with constant thickness and uniform material properties have been employed to cover the bone surface [33, 114, 118, 119]. Unfortunately, this simplification does not account for thickness variation throughout the cortical bone and neglects local material heterogeneity, which is essential when studying OA bone. Hence, techniques are required to retrieve and restore intensity information at the corrupted PV layer. The restored intensities will not only increase contrast between the cortical table and surrounding tissues, but also make it possible to use straightforward threshold methods to delineate between cortical and trabecular bone.

Several methods have been suggested in the literature for restoring intensity information at the corrupted PV layer. Recently, a numerical deblurring algorithm has been developed to reduce PV effects and restore geometry and intensity information of the CT image stack [116, 120]. The deblurring algorithm reconstructs image data by optimizing the point spread function (PSF) of the CT scanner. PSF is the impulse response of a CT scanner and determines final resolution of a CT image (which is different than the voxel size). Intensity information at the PV layer has also been restored based on the intensity of inner voxels unaffected by PV effects [117, 121]. Helgason et al. [121, 122] addressed PV effects during material mapping, where E was refined at corrupted surface nodes by mapping an E from nearest internal nodes. PV correction algorithms may enhance QCT-FE models of the subchondral bone. It is though unclear which PV correction method will result in the most accurate prediction of local structural stiffness at the proximal tibial subchondral surface.

2.4.3.3.1 Image Deblurring

Image deblurring follows two main steps in which PSF is estimated by restrictive models of the scanned object and imaging system followed by fitting these models to the observed intensity

profile at the cortical region. The estimated PSF is used in the deconvolution algorithm to restore spatial resolution of the CT image. The non-blurred image of cortical bone is represented by a rectangular function, and the actual image is approximated by convolving PSF with a non-blurred signal as follows:

$$g(u) = i(u) * h(u, \sigma)$$

where $g(u)$ is the actual intensity profile of the cortical bone (the black line in Figure 2-5) and $i(u)$ represents the intensity profile of the non-blurred cortical region (the rectangular function in Figure 2-5), $h(u, \sigma)$ is an orthotropic Gaussian PSF with the width of σ which can be itself decomposed to in-plane (σ_{xy}) and out-of-plane (σ_z) components. The PSF is estimated by fitting an actual extracted profile to the equation obtained by convolving rectangular and Gaussian functions. The unknowns will be cortical bone thickness (x1-x2), cortical intensity (Y2) and width of the PSF (σ). Once PSF is estimated, the image is deconvolved via Richardson Lucy deconvolution method [123] to retrieve non-blurred desired signal information.

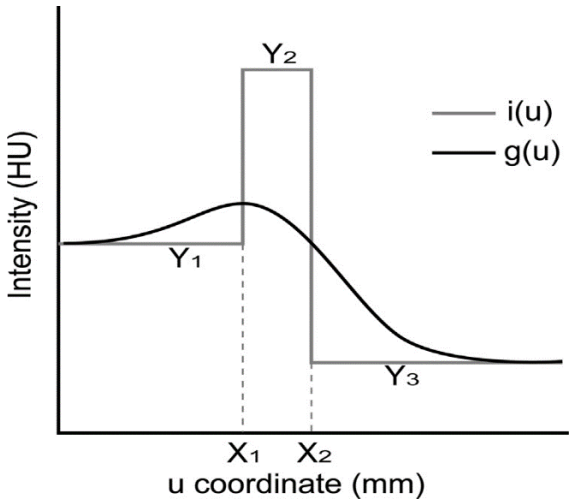

Figure 2-5. The actual intensity profile of the cortical region (black spline, g(u)) and ideal non-blurred profile of the cortex (i(u)), represented by the rectangular function. Y1, Y2, and Y3 are intensities of the trabecular bone, cortical bone, and surrounding tissue respectively, X_1-X_2 represents the cortical thickness. From Falcinelli et al. [28] with permission from Elsevier.

2.4.3.3.2 Image Remapping

In this method, low-density bone in the PV layer is replaced by denser bone using binary morphological operations and density remapping from voxels unaffected by PV artifacts (Figure 2-6). A binary mask is defined for the PV layer using morphological operations. The K-nearest neighbors (KNN) algorithm is used to find K nearest neighbors for each voxel located in the PV layer. The KNN algorithm identifies closets neighbors by calculating the Euclidian distance between the target voxel and adjacent voxels inside the bone, and returns corresponding BMD and distance values. New bone is then dilated at this region by mapping densities from underlying layers. New BMD is calculated via inverse distance weighting interpolation in order to reduce the effect of voxels located far from the PV layer as follows:

$$BMD_{corrected} = \frac{\sum_{i=1}^{K} BMD_i * 1/{d_i}^p}{\sum_{i=1}^{k} 1/{d_i}^p}$$

where $BMD_{corrected}$ is the new BMD value assigned to the PV-affected voxel, K is the number of adjacent voxels selected for BMD mapping, BMD_i is the BMD of the *ith* voxel, d_i is the Euclidean distance of the *ith* voxel from the target voxel, and p is the mapping coefficient which controls the degree to which the distance is weighted in interpolation.

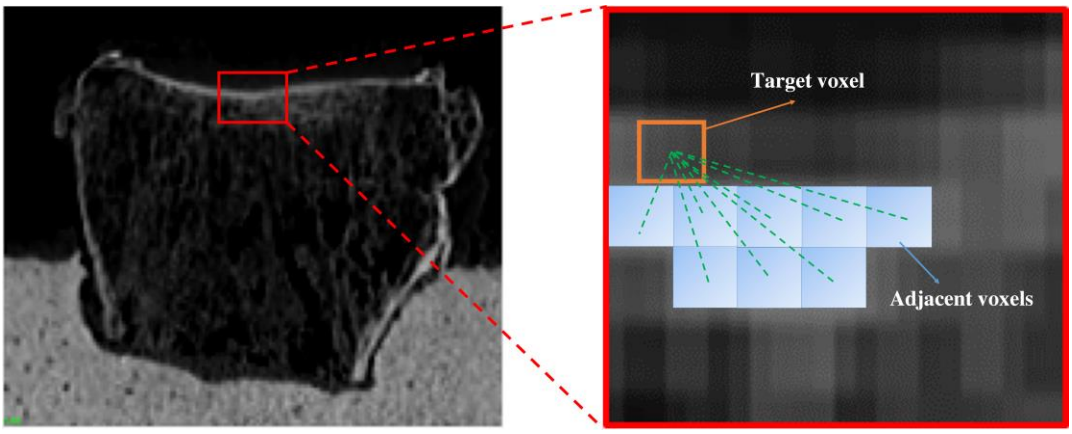

Figure 2-6. The procedure for image remapping algorithm. BMD of a target voxel in the PV layer is calculated based on BMD of adjacent voxels located inside the bone.

2.4.3.3.3 Elastic-modulus Refinement

PV layer has been also corrected inside an FE model [122, 124], where surface nodes at bone periosteal surface are identified and elastic moduli of these nodes are assigned based on E of

adjacent nodes located inside the bone. The KNN algorithm and inverse distance weighting interpolation scheme is used to refine E for each surface node (Figure 2-7).

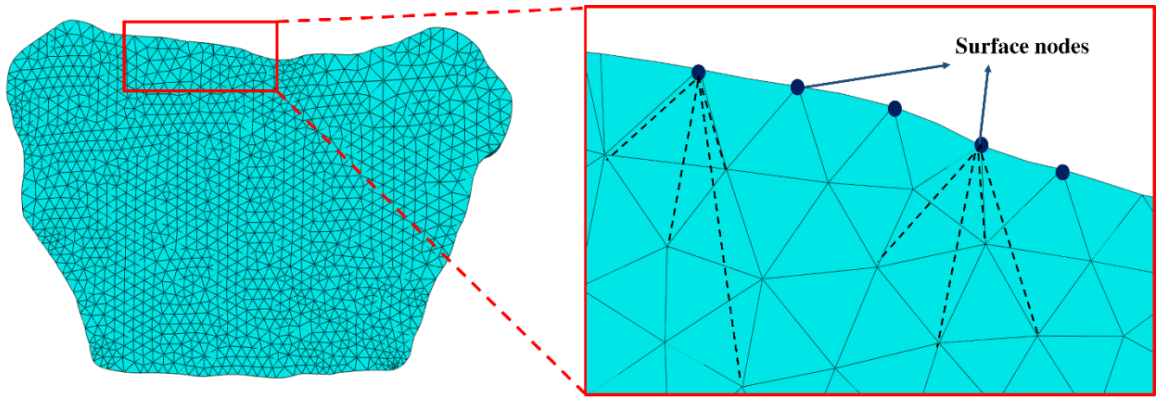

Figure 2-7. The procedure for refining elastic modulus (E) for nodes located at the periosteal surface. E of each surface node is calculated based on E of nodes located inside the bone.

2.4.3.4 Meshing

Once the region of interest is defined, an FE model could be constructed and discretized using different meshing algorithms and element types. The simplest way is to directly convert each voxel to a cubic element (voxel-based approach) [125]. The mesh is directly created from the CT image stack and avoids any geometrical surface and volume extraction. The voxel-based method has been used to construct micro-FE models of porous structures such as trabecular bone [126-130]. Fracture-risk from vertebral and femoral human whole bones have been also predicted via voxel-based QCT-FE models [131, 132]. Application of this method in FE modeling of whole bones from low-resolution image stacks has been criticized due to the creation of serrated boundaries [133]. The tiled-shape edges result in stress concentrations which make the model inappropriate to study local properties such as stiffness and strain.

Structure-based meshing, on the other hand, is applied to the constructed geometry. The volume is first created from the segmented region using marching cube algorithms. The constructed geometry is then smoothed via non-uniform rational basis splines (NURBS) and subsequently meshed with tetrahedral or hexahedral elements [67, 68, 88, 134]. Validated FE surface strain predictions of the femoral bone reveal that cubic elements result in higher accuracy compared to other mesh types [133]. Nevertheless, creating a hexahedral mesh requires significant computational effort due to intricate morphology and complex contours of the bone surface.

Conversely, a tetrahedral mesh can be easily constructed, even from geometries with irregular complexities.

FE-predicted results have also been shown to be sensitive to the order of the element shape function [23, 24, 135]. A comparison between FE-predicted femoral surface strains from linear (4 node) and quadratic (10 node) tetrahedral elements and experimental measurements suggest that the linear tetrahedral mesh should be avoided due to its higher computation time and lower predictive accuracy [135]. Higher-order elements (p-elements) alongside automatic mesh generation algorithms have been used to calculate the mechanical response of femoral bones to different physiological loads [22-25]. This method keeps the mesh unchanged and alters the polynomial order of an element shape function. The p-elements with large aspect ratios produce considerably faster convergence rates when compared with that of linear and quadratic elements. Nevertheless, application of the p-method requires custom FE formulation and cannot be performed with commercial FE packages.

2.4.3.5 Material definition

Heterogeneous and locally isotropic (i.e., same material properties in different directions) material definition for QCT-FE models starts with calibrating CT HU to BMD followed by conversion of BMD to an elastic modulus. The former is performed with standard CT calibration phantoms provided by manufacturers. Calibration phantoms contain several channels with known concentrations of hydroxyapatite (HA) or hydrogen dipotassium phosphate (K_2HPO_4). The phantom is scanned alongside a target specimen, and the HU values are normalized against known densities in phantom channels to find the calibration equation between CT Hounsfield units and BMD. The calibration step is required as measured HU numbers might differ for the same specimen by the type of scanner or short-term scanner drifts and can make a comparison of CT numbers questionable [20]. Calibrated BMD is then converted to the elastic modulus via empirical mathematical relationships known as E-BMD equations (Figure 2-8). These equations are derived by correlating the measured elastic modulus from mechanical testing to bone density. Various measures of bone density include wet/dry apparent density (i.e., hydrated/dry mass divided by bone's total volume) and ash density (i.e., the bone ash mass normalized to its total volume). Conversion equations have been proposed in the literature to convert between these densitometric measurements [20, 21, 88].

E-BMD relationships are generally in the form of power-law functions; though, other types of relationships have been reported in the literature (e.g., sigmoid functions) [136]. The E prediction for the same density range from available E-BMD equations indicate substantially different values (Figure 2-8). This could be explained by differences in applied testing protocols and employed specimen size and boundary conditions [21]. Moreover, elastic modulus measurements have been performed on samples excised from various anatomical sites with significantly different microarchitecture and tissue properties, which could further explain the observed variance in E-BMD equations.

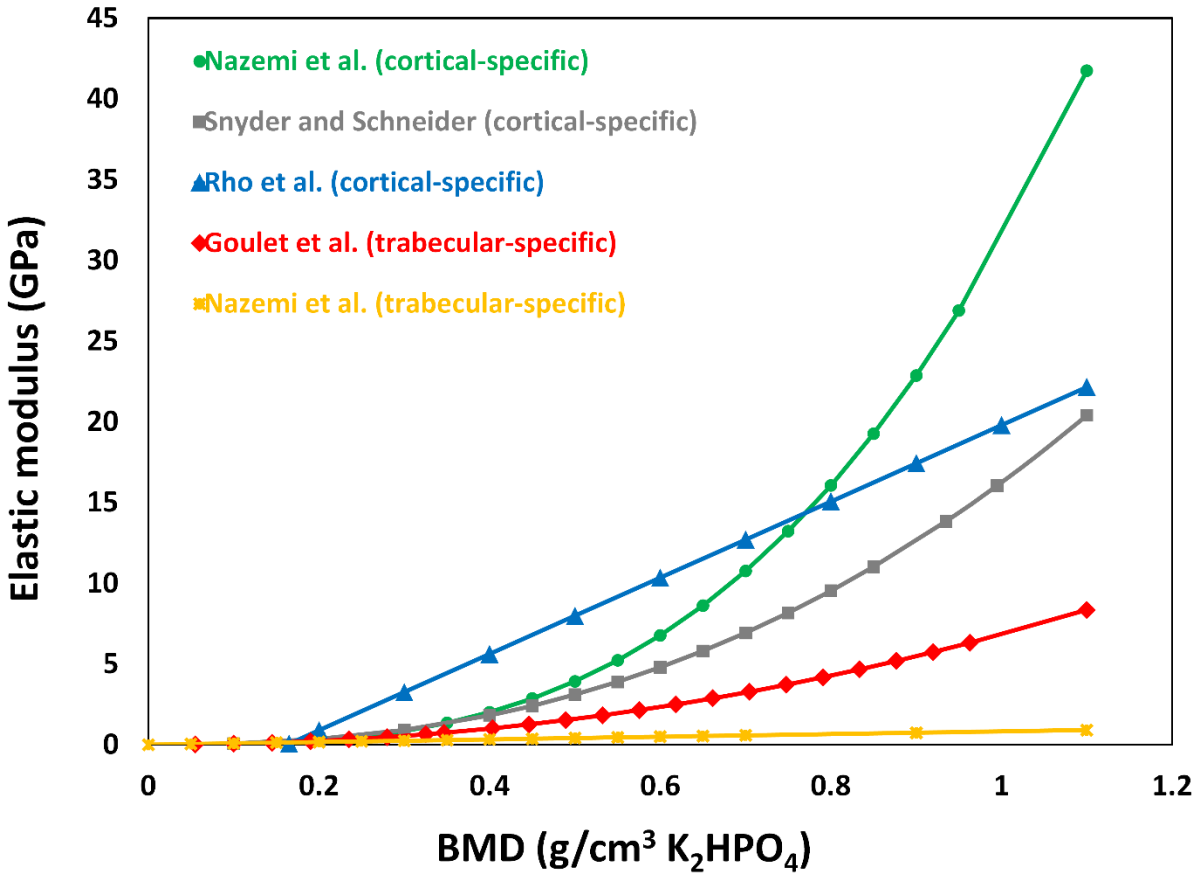

Figure 2-8. E-BMD equations reported in the literature for various anatomical sites including the proximal tibia [15, 16, 54, 110].

Different researchers have investigated the sensitivity of subject-specific FE models to adopted E-BMD equations. Schileo et al. [68] studied the effect of selected E-BMD relationships proposed by Carter and Hyes [17], Keller [137] and Morgan et al. [138] on FE predictions of local strains in

femoral bones. Morgan's E-BMD equation resulted in the least RMSE% (root mean squared error normalized to the maximum measured value) between FE-predicted and measured strains. In another study, inhomogeneous mechanical properties of the ulnar bone were defined via six different E-BMD equations and resulted in different amount of errors between the predicted and measured strains (mean prediction error ranged between 15.3% and 92.4% for different E-BMD equations) [139]. Different levels of accuracy has been also reported for FE-predicted surface strains at the distal radius using different E-BMD relationship, with RMSE% equal to 13.17%, 13.33% and 14.18% for Keller [137], Carter and Hyes [17], and Morgan et al. [138], respectively [82]. These studies employed a single E-BMD equation to calculate mechanical properties of both cortical and trabecular bone. Long bones such as the ulna and femur are mostly comprised of cortical bone, and a single E-BMD equation is sufficient to simulate the mechanical response of these structures to the applied load [67, 68, 71]. Conversely, approximately 68-73% of the proximal tibial volume is comprised of the trabecular tissue [118]. Accordingly, trabecular bone will play a large role in the mechanical response of the proximal tibia. The combination of cortical and trabecular-specific E-BMD equations, as opposed to a single relationship, has been shown to better predict the mechanical behavior of the proximal tibia. Nazemi et al. [109] found that the combination of Rho [16] and Snyder and Schneider [54] (cortical-specific) with Goulet [15] (trabecular-specific) explained the highest measured stiffness variance at the proximal tibial subchondral surface (R^2= 77% and 75%, respectively). In another study performed to simulate the failure load of proximal tibia under physiological loads, it was observed that using a constant elastic modulus (14-18 GPa) for cortical bone alongside Morgan's trabecular-specific equation [138] better predicted the fracture load of the human tibial bone [118]. Modeling cortical and trabecular bone with different E-BMD equations requires separating these structures either in the FE model or the QCT image (as described in 2.4.3.2). It is though unclear if the performance of E-BMD equations will be affected by the adopted tissue separation technique.

2.4.3.6 Material mapping

Quantified mechanical properties from QCT data need to be mapped on nodes and elements of an FE model. Different strategies employed in the literature each have their own advantages and disadvantages. Primary algorithms initially determined BMD at element nodes from the related voxel in the CT lattice and calculated the element BMD by averaging its nodal values [140]. The approach lead to inaccurate results when the element size was big and contained a large number

of voxels within its volume. In another method, the element equivalent BMD or elastic modulus was calculated by averaging voxel values inside the element volume [33, 109, 141, 142]. This method required complex coding and increased the computation time. In a more common method, BMD of the element is calculated by the integration of BMD field over the element volume [34, 121]. This technique can resolve the mentioned limitations but it does not take into account variations of BMD inside the element. Previous studies have also shown that, due to the non-linear nature of E-BMD relationships, it is more accurate to first convert voxel BMD values to E, then average this new scalar field on each element [143]. Aside from the single E assigned to each element, one major drawback with these methods is that the material needs to be averaged at specific intervals (known as material binning). A large number of elements and heterogeneous properties of the bone tissue results in a vast number of material sets in the FE package, making the numerical solution unattainable. Hence, material binning is required to reduce the number of materials and make the FE solution feasible. Binning leads to another source of averaging artifact in the QCT-FE process and might adversely affect the accuracy of the model.

Recent studies have taken into account the variation of E inside elements. Elastic moduli could be initially defined at element nodes and then interpolated on element integration points [117, 122, 144, 145]. It is also possible to map the elastic modulus directly on element integration points and use these values in numerical integration to calculate the element stiffness matrix [145, 146]. It is currently unknown if accounting for spatial variation of elastic modulus within the element and omitting element binning can lead to more accurate FE predictions of local structural stiffness at the proximal tibia.

2.5 Summary

- Even though OA is regarded as a cartilage disease, it can affect the morphology and mechanical properties of the underlying bone. An *in-vivo* noninvasive technique is required to perform longitudinal studies and assess whether the bone structural changes play a role in OA initiation and progression. Among *in-vivo* methods, QCT-FE modeling takes into account the geometrical, morphological and microstructural differences among living individuals.
- Developed QCT-FE models of the proximal tibia for assessing local stiffness at the subchondral surface indicated moderate predictive accuracy (R^2= 54%-81%, RMSE% =

10.5%-337%) [75, 99, 110]. The moderate predictive accuracy might be due to inaccurate modeling of thin cortical structures in standard QCT-FE frameworks.

- The subchondral cortical endplate of the proximal tibia contains areas with low thickness (<1 mm). The limited resolution of clinical CT systems results in low tissue contrast at areas of thin cortical bone. Hence, applying simple threshold-based methods is likely insufficient to distinguish between cortical and trabecular bone.
- Advanced techniques are required to model thin cortical structures. The cortex might be modeled with semi-automatic segmentation with manual correction followed by separate modeling of cortical and trabecular bone.
- The intensity information at CT systems could be retrieved from the CT image using different PV correction methods to enhance the contrast between cortical and trabecular bone, which will facilitate tissue separation using simple threshold methods.
- Conventional mapping methods which result in material binning and disrupt the continuity of elastic modulus have potential to be replaced with advanced element based techniques to account for E variation throughout the element volume, which could eliminate another source of averaging in QCT-FE models.

CHAPTER 3

3 RESEARCH QUESTIONS AND OBJECTIVES

My specific research questions were:

1. Which segmentation and modeling technique best differentiates cortical and trabecular tissue, leading to the most accurate QCT-FE prediction of local structural stiffness at the proximal tibial subchondral surface?
2. Can partial volume correction at thin cortical regions enhance QCT-FE predictions of local stiffness at the subchondral surface?
3. Which mapping strategies proposed in the literature results in the highest accuracy for modeling local stiffness at the proximal tibial subchondral surface?

To address these questions, my objectives were defined as follows:

1. Identify the segmenting and modeling approach which best predicts (with largest explained variance and least amount of error) local structural stiffness at the proximal tibia.
2. Evaluate QCT-FE predictions of stiffness acquired from different PV-correction algorithms in relation to experimentally derived stiffness.
3. Evaluate different material assignment strategies and identify the mapping approach with the fastest convergence behavior and highest accuracy.

CHAPTER 4

4 SEPARATE MODELING OF CORTICAL AND TRABECULAR BONE

4.1 Introduction

An essential step with QCT based FE modeling is to calculate mechanical properties based upon imaged BMD, typically via empirical E-BMD relationships available in the literature [15, 16, 54, 110]. Either a single or combination of E-BMD relationships have been used in the literature to calculate the heterogeneous mechanical properties in human bones [27, 75, 104, 139]. Previous findings showed that using site-specific E-BMD relationships for cortical and trabecular bone (as opposed to the single E-BMD equation for the entire density range) leads to the most accurate predictions of local stiffness at the proximal tibia [75]. These models, however, used a global threshold to separate cortical from trabecular bone. While global thresholding can separate cortical and trabecular tissue at diaphysis and metaphysis, the approach fails at regions with a thin cortical shell where limited resolution of clinical CT systems results in low contrast between cortical and trabecular bone. Hence, thin cortical regions are represented as trabecular bone within the FE model, and low elastic moduli are often assigned to these regions, which affects the predictive accuracy of the FE model. The typical approach in dealing with this problem is to cover the bone endosteal surface with shell elements [33, 118, 119]. However, with this method the cortical bone is modeled with a constant thickness and homogenous material properties. Unfortunately, this is undesirable for studying OA bone as it is highly heterogeneous with non-uniform thickness [4, 8, 61].

The primary objective of Study #1 was to introduce a new methodology: semi-automatic segmentation with manual correction and separate modeling (SM) for segmenting and modeling laminar shaped thin cortical structures. This methodology overcomess limitations associated with existing threshold-based methods. The secondary objective was to evaluate the proposed SM approach in relation to existing continuum modeling (CM) with threshold-based methods (i.e., global threshold (CMG) and image erosion (CME)) against *in-situ* stiffness measurements at the proximal tibial subchondral surface.

4.2 Methods

4.2.1 Samples

Sample preparation, QCT imaging and experimental testing were performed by a single researcher (James D. Johnston). The detailed information regarding specimens and sample preparation can be found elsewhere [60]. Briefly, eleven intact fresh-frozen cadaveric human knee joints were obtained from 8 donors (7 males and 1 female, age±SD: 76.2±9.2). Knee joints were exposed and all soft tissues were excised from the proximal tibia except the cartilage. Each proximal tibia was transversely cut 25 mm distal to the cartilage surface and separated to medial:lateral compartments by sagittally cutting through the tibial spine. Following tissue harvesting, each sample was visually examined by a participating surgeon and categorized based on cartilage status into the normal and degenerated categories. Samples that indicated complete cartilage loss were excluded from the study, leaving 9 lateral and 4 medial compartments. To preserve the integrity of the cartilage, the exposed surface was sealed with thin layer of polymethylacrylate bone cement (PMMA) to prevent the release of serum protease from bone marrow. Each proximal tibia was embedded in the potting system comprised of the outer shell made of polyvinylchloride (PVC) and supporting base made of gypsum potting material and the layer of PMMA. The structural support of the excised contralateral surface was simulated via a phantom compartment created out of PMMA and fixated to the sealed surface of the proximal tibia and the potting system. For registration purposes, four 1 mm diameter stainless steel fiducials markers were inserted into the outer PVC shell.

4.2.2 QCT imaging

Each potted sample was positioned centrally within the gantry of the clinical CT scanner (64-slice helical Aquilion 64, Toshiba medical systems, Tokyo, Japan) in the supine orientation and scanned alongside the calibration phantom (Figure 4-1a). A solid K_2HPO_4 phantom was used to convert between the CT gray scale values (HU) and equivalent volumetric BMD. Imaging parameters included: tube voltage: 120 kVp; tube current-time product: 150 mAs; bone standard reconstruction algorithm; 0.5 mm isotropic voxel size (0.5 mm slice thickness and 0.5×0.5 mm in-plane pixel size).

4.2.3 Mechanical testing

The stiffness at the subchondral surface was measured using macro-indentation testing. The indentation apparatus was comprised of a right-hand drill and load cell mounted on mechanical

testing system (Instron 8874, Instron Corp) (Figure 4-1b). The potted specimen was initially located in a 5 degree of freedom (DOF) positioning fixture, and the cartilage surface was oriented approximately horizontal. Attached fiducials were removed from the PVC shell, and a 3D digitizer was used to locate the concave fiducial holes, indenter tip and XYZ axes of the testing system. The indentation locations on each compartment were determined based on the anterior-posterior and central-peripheral dimensions (Figure 4-1c). To avoid potential mechanical damage to surrounding bone, at least 7 mm spacing was left between adjacent indentation sites. A total of 47 indentation locations from 13 specimens were included in this study. The bone surface was determined via compressive needle testing [147], and the subchondral bone was subsequently milled 0.1 mm beyond the defined subchondral surface to create a flat indentation surface with a diameter of 4 mm. A 3.5 mm flat-ended nonporous indenter was used to perform macro indentation. A displacement with a constant rate (2 mm/min) was applied on each indentation location while the load was continuously monitored at 1000 Hz using custom software (LabView, National Instruments, Austin, TX). The test stopped when the displacement reached 0.5 mm or the load reached 250 N (maximum limit of the load cell). The local structural stiffness was then measured as the slope of the fitted regression line to the most linear region of the load-displacement curve (Figure 4-1d).

4.2.4 Image registration

Image registration was performed using a custom Matlab code that matched imaged fiducial with physically located fiducial coordinates in the mechanical testing setup. Indentation coordinates were located in the image space based upon digitized coordinates of the indenter tip and replicated specimen orientation. Evaluation of registration accuracy resulted in errors less than 0.42 mm, which was smaller than the CT voxel size.

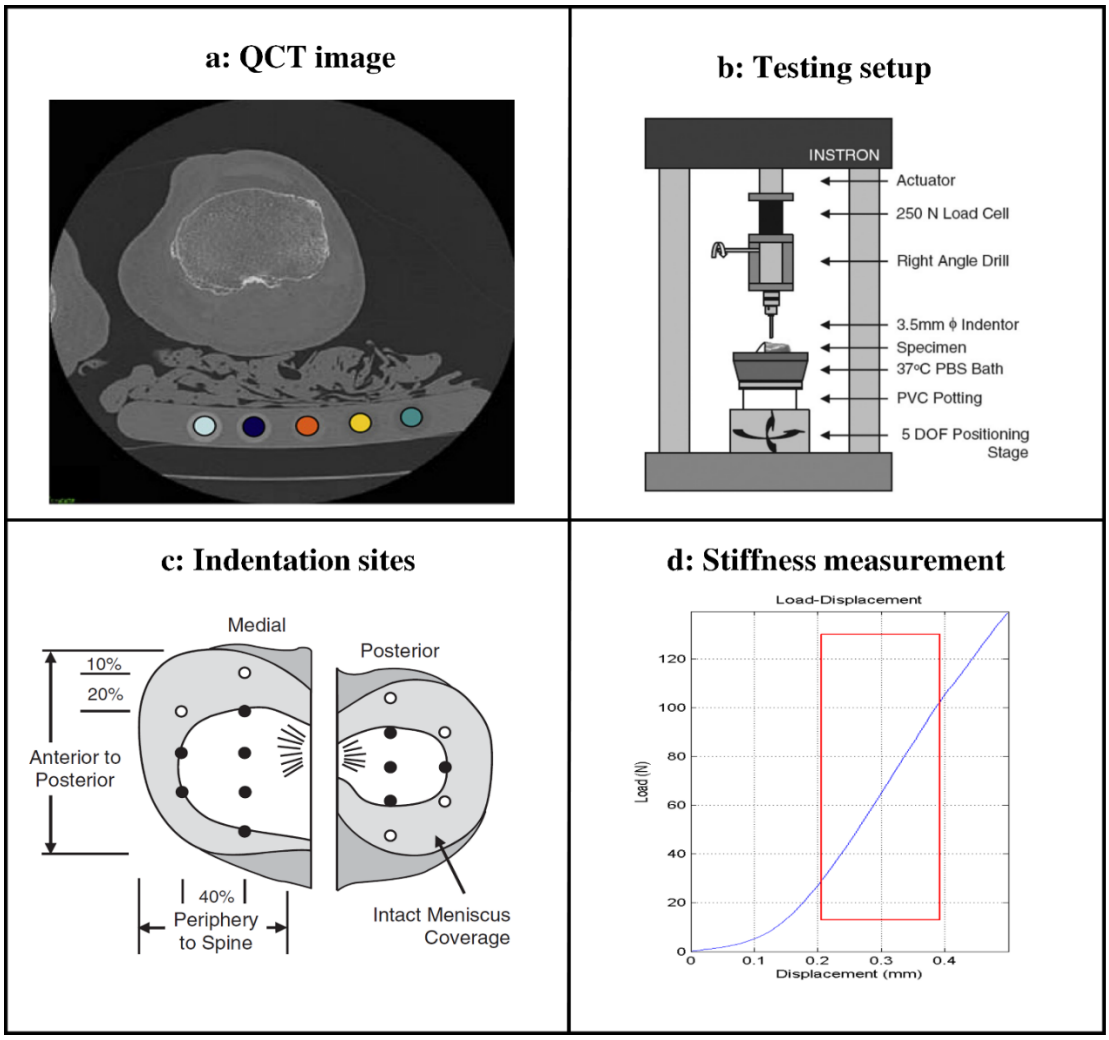

Figure 4-1. Imaging and the experimental procedure was performed by a single researcher (James D. Johnston) [46, 60]. Each proximal tibia was scanned along with a calibration phantom to convert computed tomography (CT) gray scale values (Hounsfield units, HU) to bone mineral density (BMD) (a). Potted samples were fixated in a 5 degree of freedom (DOF) positioning stage mounted on the mechanical testing system (b). Indentation locations were identified based on the anterior-posterior and central-peripheral dimensions (c). The indentation was performed with the 3.5 mm non-porous flat-ended indenter. The slope of the regression line fit to the most linear portion of the load-displacement curve was defined and reported as local structural stiffness (d).

4.2.5 Finite element modeling

4.2.5.1 Segmentation

The cortical bone was visualized by separating periosteal (i.e., the bone outer profile) and endosteal (the cortical-trabecular boundary) surfaces from surrounding soft tissue and inner trabecular structure with three different segmentation methods:

4.2.5.1.1 Semi-automatic segmentation with manual correction

Using the image processing software Analyze (Analyze6.0; Mayo Foundation, Rochester, MN, USA), each CT image slice (Figure 4-2a) was segmented in the sagittal plane with the combination of the half maximum height (HMH) method, a region growing algorithm and manual intervention via a touchscreen tablet. BMD (K_2HPO_4 equivalent density, ρ_{QCT}) was first determined from the histogram line of the bone intensity across subchondral endplate and cortical shaft for each sample using the HMH method, and used as an initial estimate for the tissue threshold (Figure 4-2b) [107]. The segmentation started with locating seed points in dense cortical regions, either at the bone shaft or subchondral surface. The threshold was set to values obtained from the HMH method and the region growing algorithm automatically identified voxels with BMD above the defined threshold. The low imaged contrast between cortex and trabecular bone resulted in the creation of unclosed boundaries (Figure 4-2c). The gaps were closed by manually linking edges belonging to the same boundary at each image slice. Care was taken to include at least two voxels in the segmentation to ensure that the separated structure could be later resolved in the FE model. Once the cortical region was identified, the trabecular structure was segmented by putting a single seed point in the proximal tibia and restricting the boundary to the defined endosteal surface (Figure 4-2d).

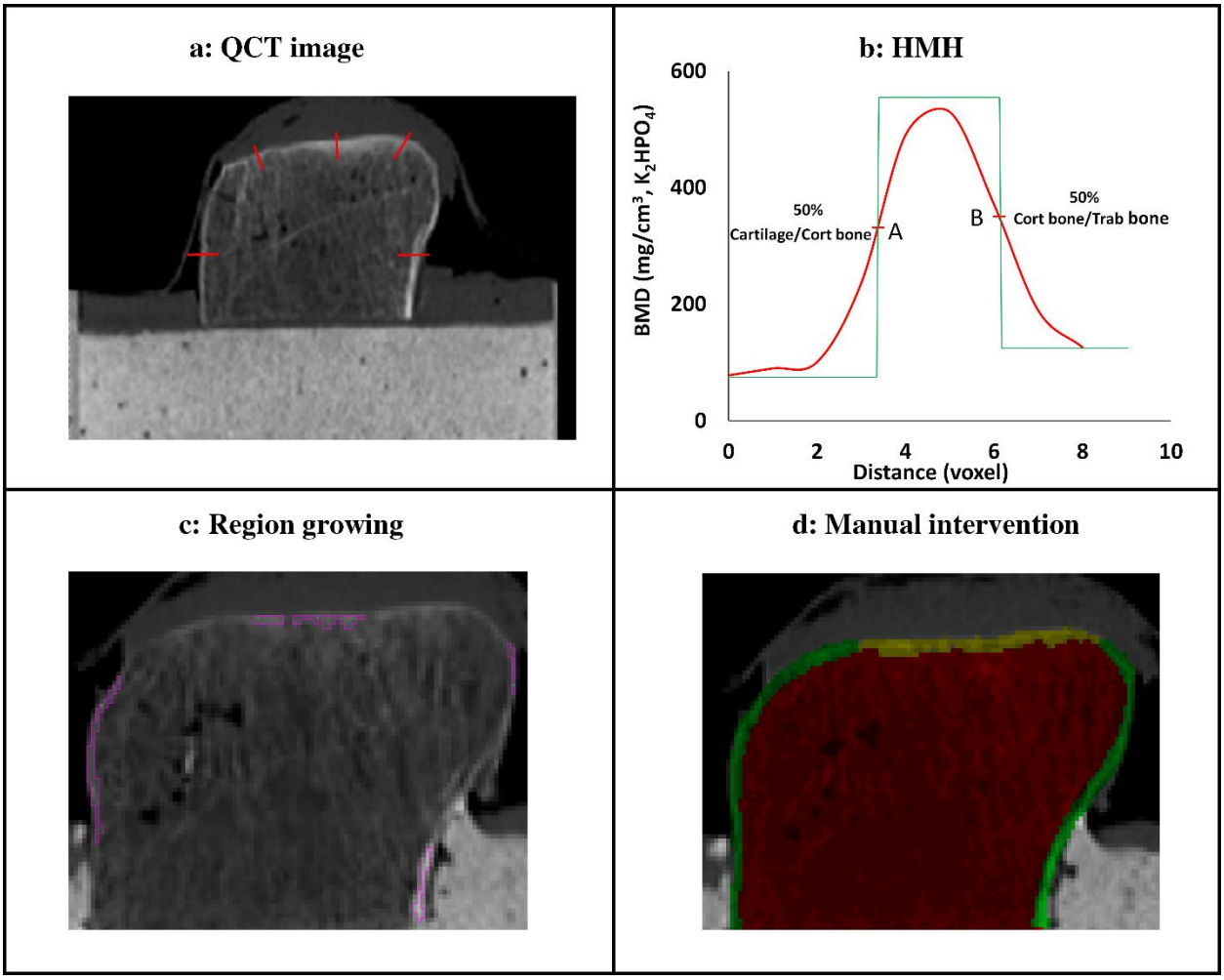

Figure 4-2. The methodological sequence for semi-automatic segmentation with manual correction of the cortical bone. Red lines were sketched across the cortical bone at different regions of the sagittal plane of CT images (a). The BMD threshold was determined from the intensity histogram of the sketched line as the 50% BMD between the low-density cartilage and high-density cortical bone at point A. Point B indicates 50% intensity between cortical and trabecular bone and green line is the ideal cortical profile (b). A region growing algorithm was used to identify the cortical bone based on calculated thresholds (c). Gaps were closed manually to visualize the cortical table and the trabecular bone (d).

4.2.5.1.2 Image erosion

The HMH and region growing methods were used as before to obtain the optimum threshold and identify the bone periosteal surface. Segmentation was though performed for the whole proximal tibia (Figure 4-3a & b). A temporary cortical region was then identified by eroding seven voxels

(3.5 mm) [108] from the bone periosteal surface using binary morphological operations (Figure 4-3c). The cortical bone within this region was subsequently detected by employing a global apparent density of 1 g/cm^3 equal to the ρ_{QCT} threshold of 550 mg/cm^3, as per Gray et al. [105] (Figure 4-3d). This approach ensured that all cortical bone was less than 3.5 mm from the periosteal surface.

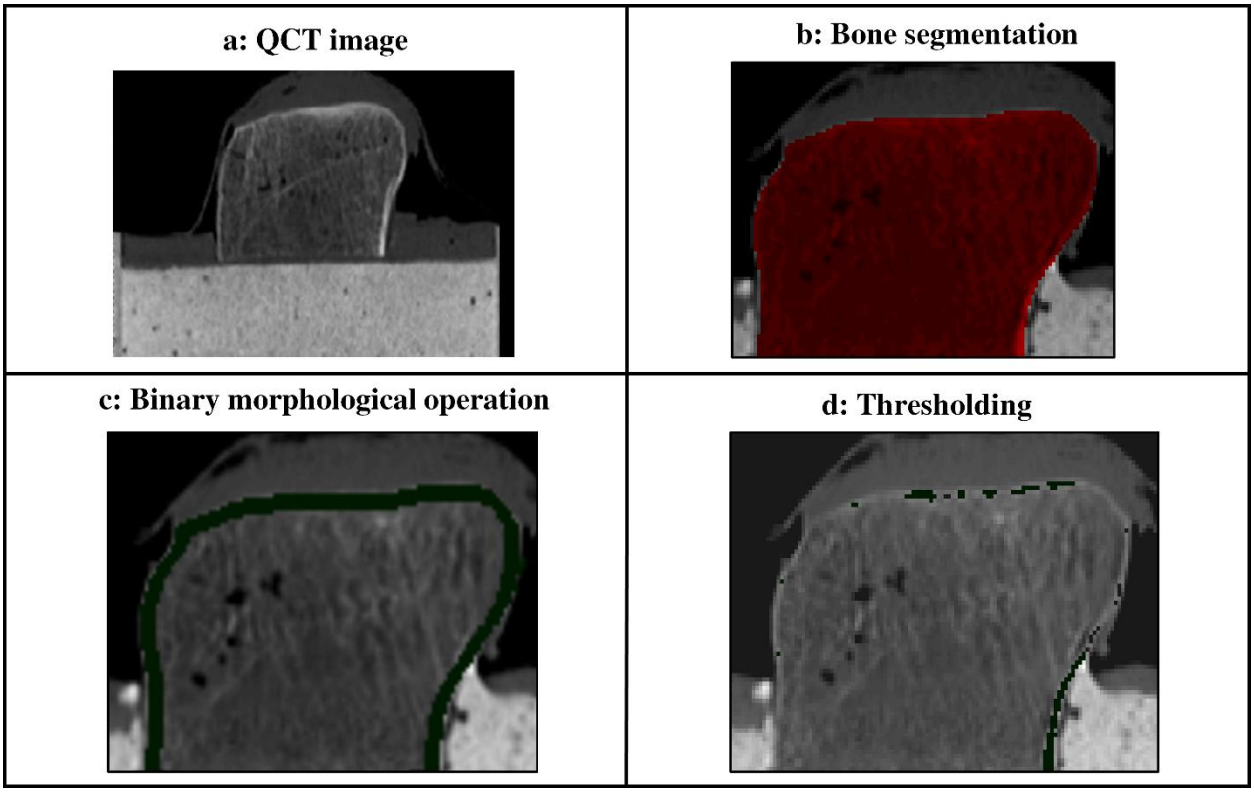

Figure 4-3. The methodological sequence for tissue separation using an image erosion technique. The CT image (a); was first segmented using the half maximum height method (HMH) and region growing algorithm (b). Binary morphological operations were then used to detect a temporary cortical region with the thickness of 3.5 mm (c); the cortical bone was then determined using the threshold of 550 mg/cm^3 within the region of interest (d).

4.2.5.1.3 Global threshold

The bone was separated from the surrounding soft tissue via the HMH method (Figure 4-4a). In this case, the cortical and trabecular bone were differentiated with a ρ_{QCT} threshold of 550 mg/cm^3 [105] (Figure 4-4b).

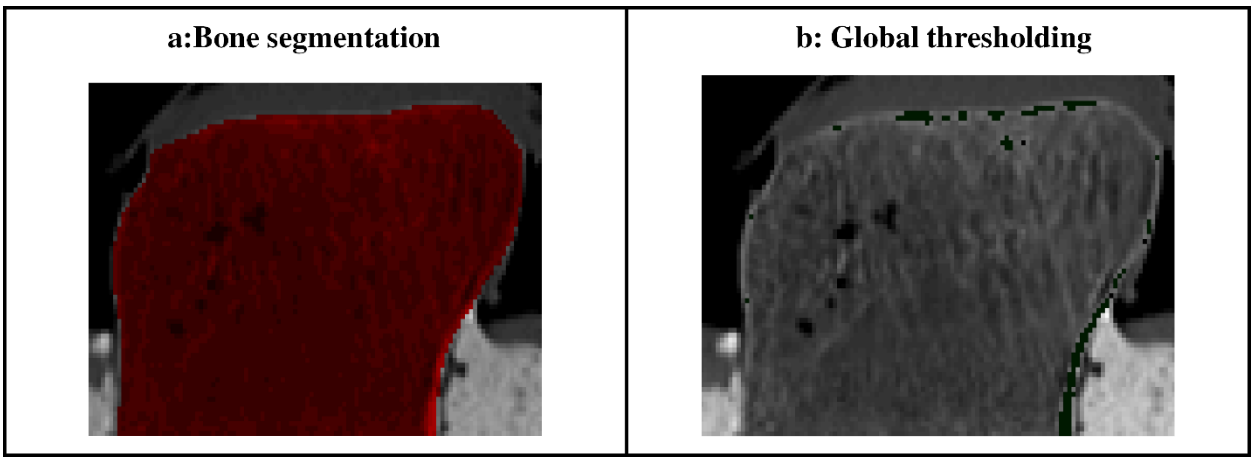

Figure 4-4. Cortical bone detection with a global threshold. The proximal tibia was segmented from surrounding tissue via the half maximum height method (HMH) and region growing algorithm (a). A cortical tissue was then identified with a single global threshold of 550 mg/cm^3 (b).

4.2.5.2 Model construction

FE models were constructed from segmented regions using two distinct methods and three different sets of E-BMD equations:

1. Separate Model (SM) - Individual meshes and models of cortical and trabecular were developed. In this case, cortical and trabecular elements composed distinct structures in the FE model.
2. Continuum Model: Image Erosion (CME) - A single mesh and model of bone was developed. In this case, cortical and trabecular elements could be interspersed next to one another within the model, and were defined based upon the image erosion segmentation method.
3. Continuum model: Global Threshold (CMG) - Similar to image erosion. In this case, cortical and trabecular elements were defined based upon the global threshold segmentation method.

4.2.5.2.1 Separate Modeling (SM)

Semi-automatic segmentation with manual correction of the cortical and trabecular bone made it possible to model these structures separately. A marching cube algorithm was used to construct a 3D volume for the cortical and trabecular bone from segmented object maps (Figure 4-5a). The constructed volumes were then healed, their surface were smoothed and converted to non-uniform

rational basis splines (NURBS) via reverse engineering software (GEOMAGIC STUDIO 12, Systems, Rock Hill, SC, USA) (Figure 4-5b). Care was taken to preserve the maximum geometrical complexity by monitoring the root mean squared error (RMSE) between original and smoothed surface. The RMSE was always kept below 0.3 mm, which was less than the voxel size. Surface smoothing alters the bone endosteal surface at cortical and trabecular bone making it rather impossible to assemble these structures within the FE model due to the presence of collisions and clearances at the contact surface. To prevent this problem and ensure a perfect fit between two structures, the trabecular bone was constructed by filling the cortex inner volume using CAD software (SOLIDWORKS, Dassault Systems, Tennessee) (Figure 4-5c). Smoothed volumes were extracted to a commercial FE package (ABAQUS, Providence, RI, USA) and geometrical operations were performed at the subchondral endplate to construct indentation sites. Flat cylindrical holes ($\Phi 4\ mm$) were created and a 3.5 mm concentric surface equal to the diameter of the indenter was partitioned from the flat surface and defined as the indentation location. Subsequently, cortical and trabecular structures were meshed independently with 10-node quadratic tetrahedral elements and assembled by coupling elements located at the cortical-trabecular boundary (Figure 4-5d). Coupling (also called tying or bonding) constrained each node at the trabecular surface to have the same DOF to its closest node at the cortex endosteal surface. All nodes at the bone surface located 25 mm distal to the subchondral endplate were constrained in all directions to mimic the bone inside the fixed pot. As well, all DOF were constrained for nodes at the sagittal cutting plane to replicate the phantom compartment. A 0.9 and 0.7 mm global mesh size was used for the trabecular and cortical region, respectively. These values were arrived upon from a convergence study, where reducing the element global size from 0.9 mm to 0.7 mm for the trabecular and 0.7 mm to 0.5 mm for the cortical bone altered stiffness predictions by less than 3%.

Linear elastic and isotropic material properties were defined for the FE model, starting with converting imaged ρ_{QCT} to ash density (ρ_{ash}) assuming $\rho_{QCT} = \rho_{ash}$ as per [79, 81, 98, 136], followed by the conversion of ash density to the elastic modulus using three sets of cortical and trabecular specific E-BMD equations summarized in Table 4-1 (Goulet-Rho [15, 16], Goulet-Snyder [15, 54], Nazemi-Nazemi [110]). The maximum elastic modulus cannot exceed the E of compact bone. Therefore, depending on the adopted cortical–specific equation, the maximum elastic modulus of the cortical bone was limited to 15 GPa and 19 GPa when the apparent density

equaled that of compact bone (1.8 g/cm3) [17]. The E of 0.1 MPa was assigned to all voxels inside the segmented region with negative BMD values. Negative densities pertained to fat, air, and marginal osteophytes (APPENDIX - Figure A-1ure A-1). Poisson's ratio was set to 0.3 [148].

Calculated elastic moduli at the CT lattice were mapped to an FE model using a custom Matlab algorithm (Figure 4-5e). The code initially mapped an E on each node from the voxel containing that node. A constant E was then calculated for each element by the integration of elastic moduli over the element volume [34]. The procedure was performed independently for cortical and trabecular elements, with values stored in separate matrices. To reduce the number of defined materials, elements with elastic moduli with a user-defined interval (20 MPa) were grouped in one bin at each matrix. Weighted volumetric averaging was then used to determine the elastic modulus for each material bin. In total, there were 450 to 750 bins for cortical and trabecular bone. In terms of the rational for the 20 MPa interval, 50, 20 and 10 MPa intervals were checked. Reducing the interval from 20 to 10 MPa changed stiffness predictions less than 3%; therefore 20 MPa was applied.

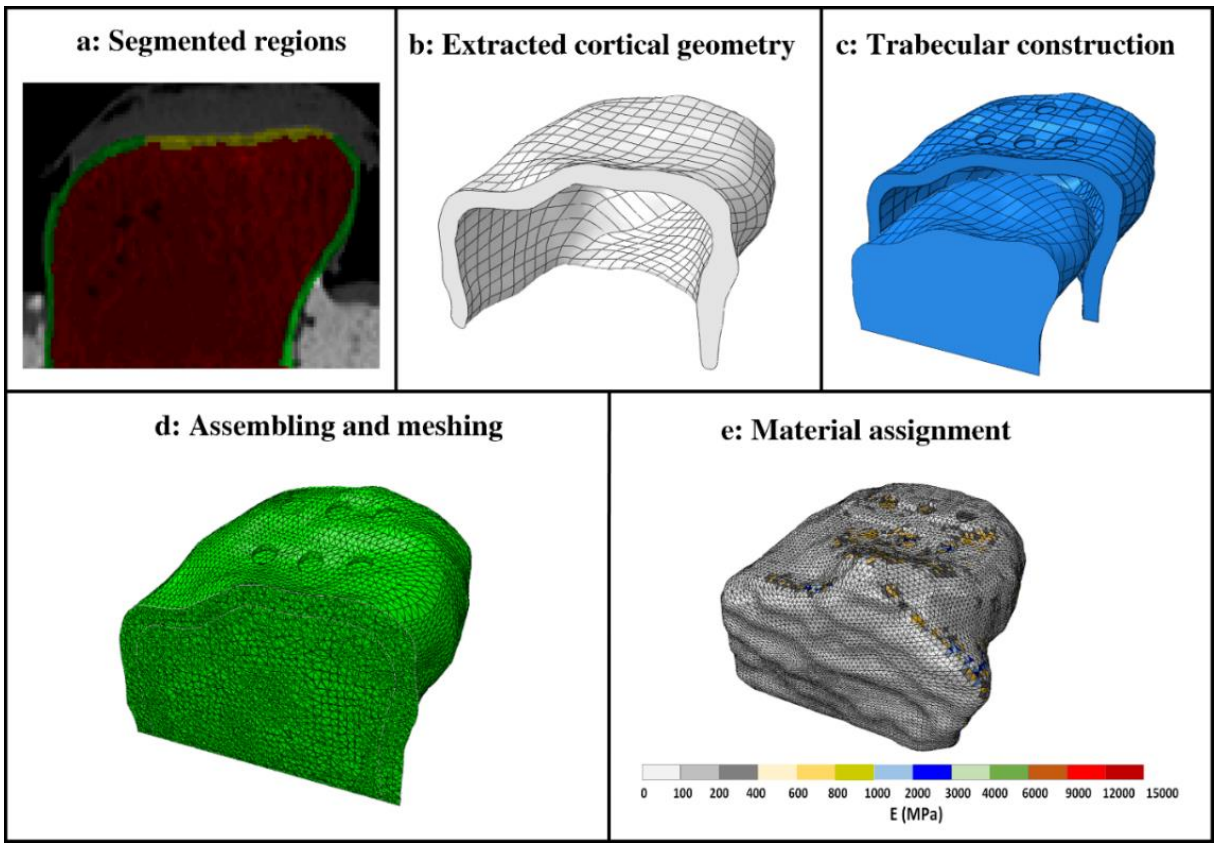

Figure 4-5. The methodological sequence for separate modeling of the proximal tibia. The segmented cortical region (a); was used to construct the cortex 3D geometry using the marching cube algorithm and smoothed via non-uniform rational basis splines (NURBS) (b). The trabecular bone was then constructed by filling the cortex inner volume with CAD software (SOLIDWORKS) (c). Cortical and trabecular bone coupled at the endosteal surface and meshed independently using quadratic tetrahedral elements (d). Material properties were mapped to the FE model by the integration of elastic moduli field over the element volume (e).

Table 4-1. Adopted density-modulus (E-BMD) relationships in this study.

E-BMD`	Bone tissue	Skeletal site	E (MPa)	Density range (g/cm^3)
Goulet et al. [15]	Trabecular	Pooled	$E = 6310(BV/TV)^{2.1}$	0.06-0.36
Nazemi et al [110]	Trabecular	Tibial subchondral bone	$820\ \rho_{QCT}$	$\rho_{QCT} < 0.5$
Rho et al. [16]	Cortical	Tibial Shaft	$13000\rho_{app} - 3842$	N.S*
Snyder and Schneider [54]	Cortical	Tibial Shaft	$E = 3891\rho_{app}^{2.39}$	1.748-1.952
Nazemi et al. [110]	Cortical	Tibial subchondral bone	$31360\ \rho_{QCT}^3$	$\rho_{QCT} > 0.5$

* Not specified

$BV/TV=\rho_{app}/1.8$ [21], $\rho_{app}=\rho_{ash}/0.55$ [21], $\rho_{QCT}=\rho_{ash}$ [79, 81, 98, 136]

4.2.5.2.2 Continuum Modeling (CM)

The proximal tibia was modeled using the standard framework for bone QCT-FE modeling (known as the Bonemat approach) [34, 141, 143]. In this case, bone was treated as a continuum and cortical and trabecular tissues were differentiated in the material mapping stage using either image erosion or a global threshold. For CME and CMG, the voxels with BMD above the predefined threshold (i.e., 550 mg/cm^3) were treated as cortex and modeled with a cortical-specific equation and those below the cutoff value regarded as trabecular bone and modeled with a trabecular-specific equation. The same E-BMD relationships and material mapping strategy were used to define material properties for the FE model except that in this case all steps performed for the whole bone structure. The geometry construction and model preparation was similar to the SM approach and is summarized in Figure 4-6. The convergence analysis resulted in global mesh size of 0.9 mm for the whole structure. Identical to SM, 20 MPa intervals were used for binning and reducing the number of material groups.

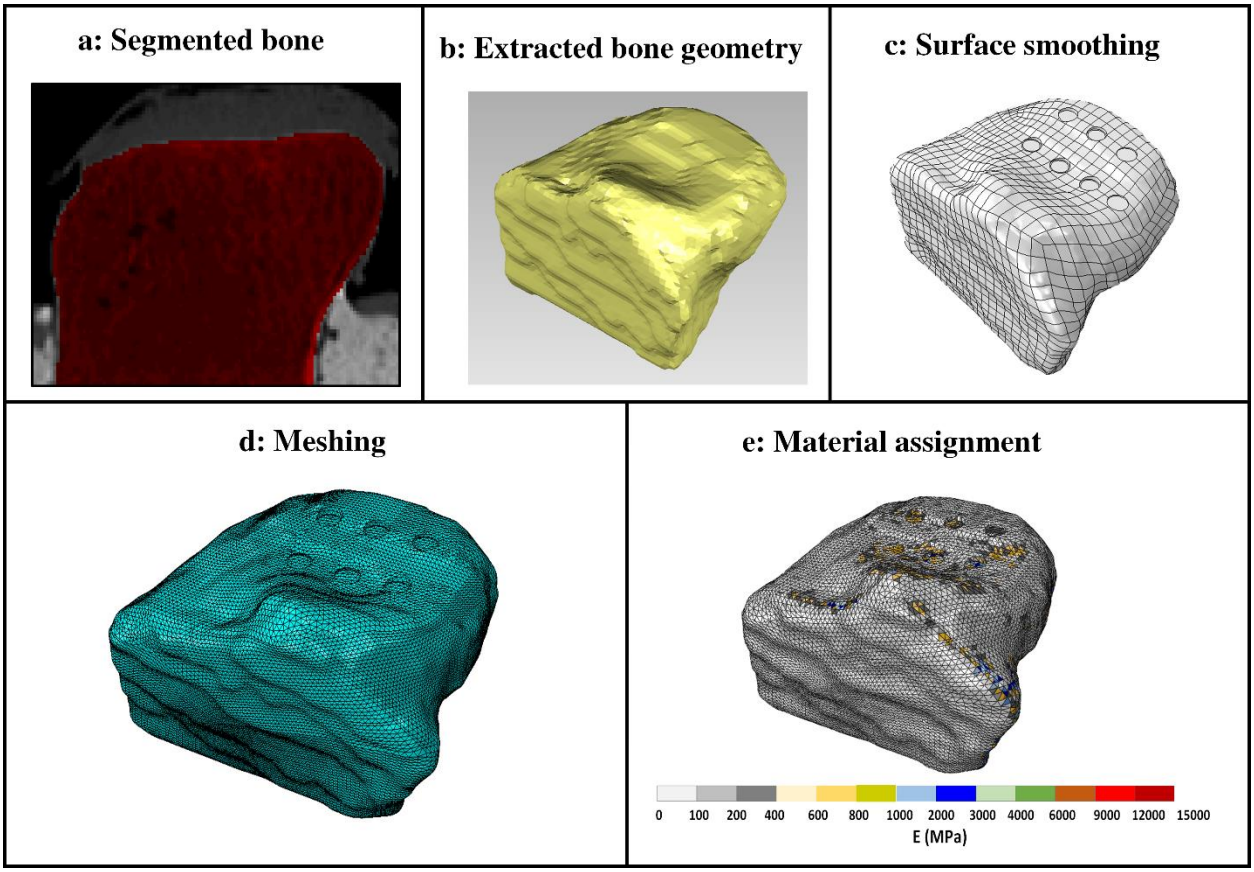

Figure 4-6. The procedure used to construct continuum QCT-FE models of the proximal tibia. The segmented bone (a); was converted to 3D models using the marching cube algorithm (b); and smoothed with NURBS (c). As opposed to separate modeling, in this case, bone was treated as a continuum, and meshed with a uniform global mesh size (d); and material mapped on the FE model by the integration of E field over the element volume (e).

4.3 FE analysis and validation

A unit axial displacement was applied over the 3.5 mm diameter surface, and a static analysis was performed using the ABAQUS FE package. For each proximal tibia, calculations were performed via 12 cores of the two 2.30 GHz processors Intel (R) Xeon (R) with 64 Gbytes of internal memory. A custom Python code was developed to read and sum FE-derived nodal reaction forces at the indentation surface. At each indentation site, local structural stiffness was calculated as total reaction force divided by applied displacement.

4.4 Statistical Analysis

Linear regression was used to assess FE predictions in predicting variance (coefficient of determination, R^2) in experimentally derived stiffness. Root mean squared error (RMSE), normalized in relation to maximum experimental stiffness (RMSE%), was used to assess model accuracy. Student's t-tests were used to identify whether the slope and intercept of the fitted regression line were different from unity and zero, respectively. Bland-Altman plots were used for residual analysis.

4.5 Results

With the SM approach, QCT-FE models explained 78% to 81% of the measured stiffness variance, with RMSE% ranging between 11.2% and 20.2%. (Table 4-2 & Figure 4-7). The slope of the regression line differed significantly from unity for all E-BMD equations evaluated in this study ($p < 0.05$), except for the subchondral-specific equations by Nazemi et al. ($p > 0.05$). Similarly, the mean difference between predicted and measured stiffness on Bland-Altman plot was significantly different from zero for all evaluated E-BMD equations and indicated the overestimation of stiffness ($p < 0.05$), except for Nazemi et al. (Figure 4-7).

With the CME approach, FE models explained 76%-80% of the variance, with RMSE% ranging between 11.7% and 15.4% (Table 4-2 & Figure 4-8). The mean difference between FE-predicted and measured stiffness on Bland-Altman plots was significantly different from zero for Nazemi et al., but not the other two equations (Figure 4-8).

With the CMG approach FE models resulted in the R2 ranging between 77% and 81%, with RMSE% of 11.6% to 14.8% (Table 4-2 & Figure 4-9) Similar to image erosion, the mean difference between FE-predicted and measured stiffness was significantly different from zero for Nazemi et al. ($p < 0.05$) but not for the other two equations (Figure 4-9).

Table 4-2. Coefficient of determination (R^2) and normalized root mean squared error in relation to maximum measured stiffness (RMSE%) for evaluated modeling approaches and E-BMD equations in this study.

Modeling approach	E-BMD					
	Goulet & Snyder		Goulet & Rho		Nazemi & Nazemi	
	R^2	RMSE%	R^2	RMSE%	R^2	RMSE%
Separate Model (SM)	0.79	12.4	0.78	20.2	0.81	11.2
Continuum - Image Erosion (CME)	0.76	11.7	0.77	12.9	0.80	15.4
Continuum - Global Threshold (CMG)	0.77	11.6	0.78	13.2	0.81	14.8

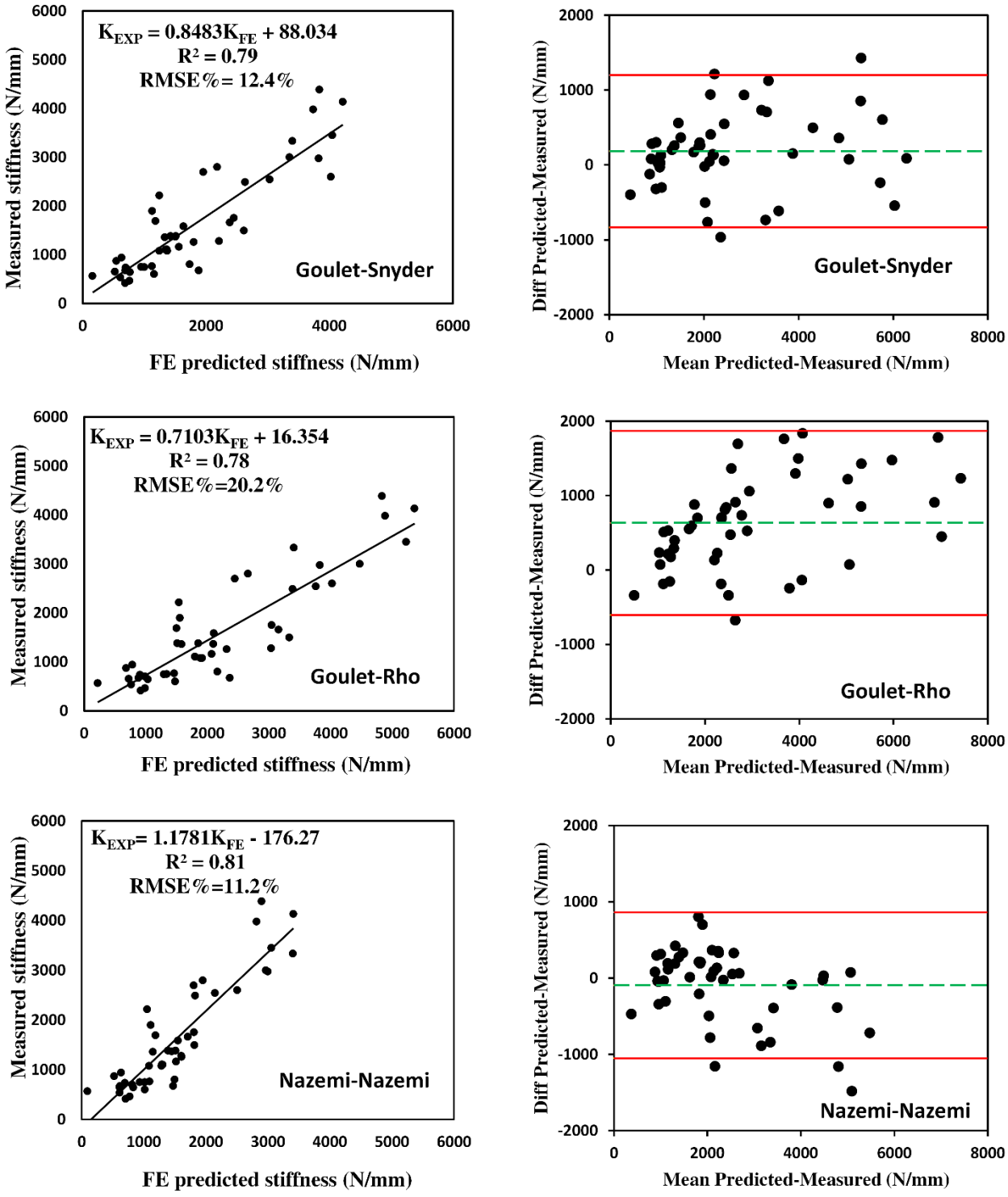

Figure 4-7. Linear regression analysis and Bland-Altman plots between FE-predicted and measured stiffness for separate modeling approach (SM) and different E-BMD equations evaluated in this study. In Bland-Altman plots, the green dashed line represents the mean difference between FE-predicted and experimental stiffness. Red lines are 95% limits of agreement.

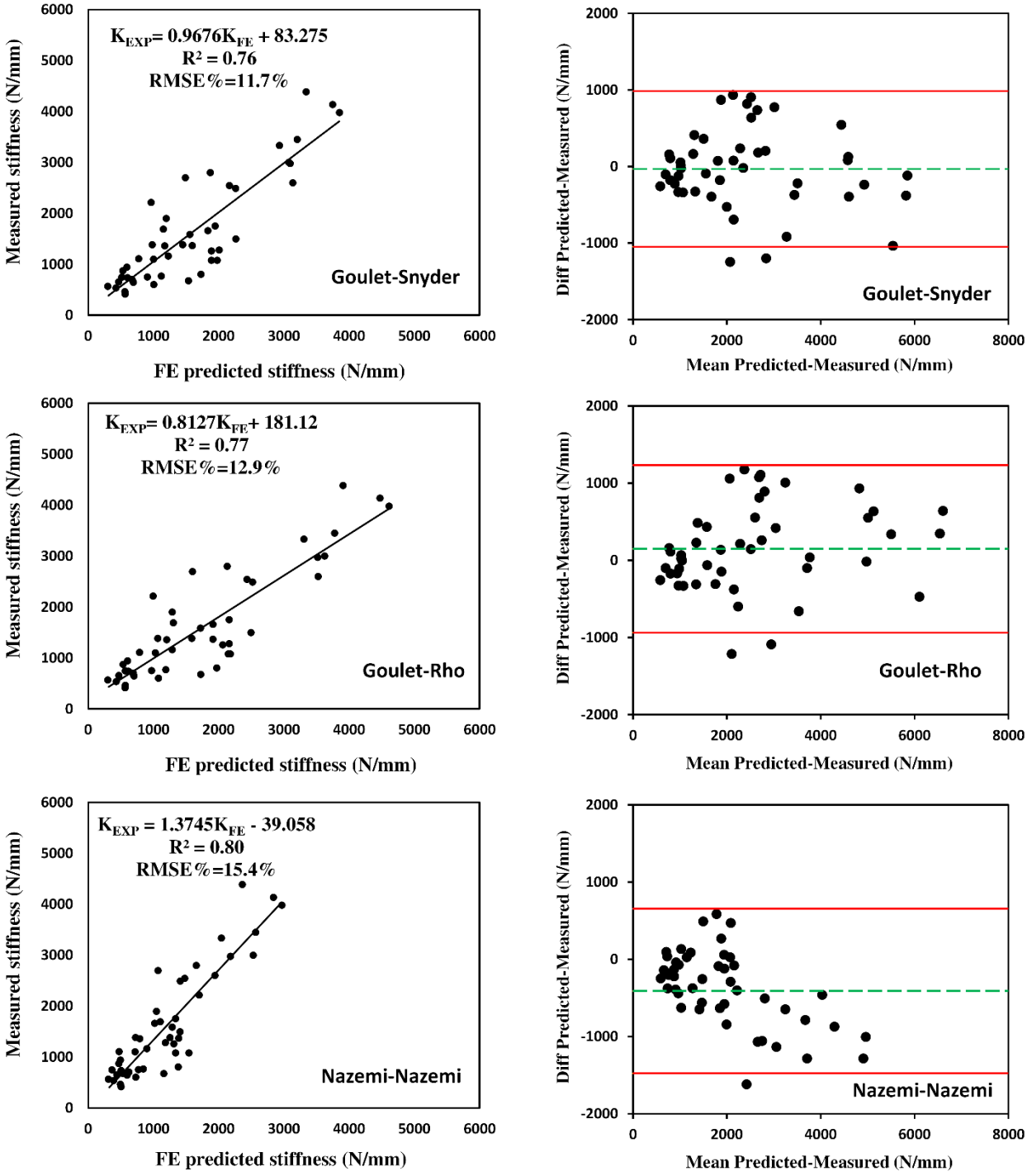

Figure 4-8. Linear regression analysis and Bland-Altman plots between FE-predicted and measured stiffness for continuum models with image erosion (CME) and different E-BMD equations evaluated in this study.

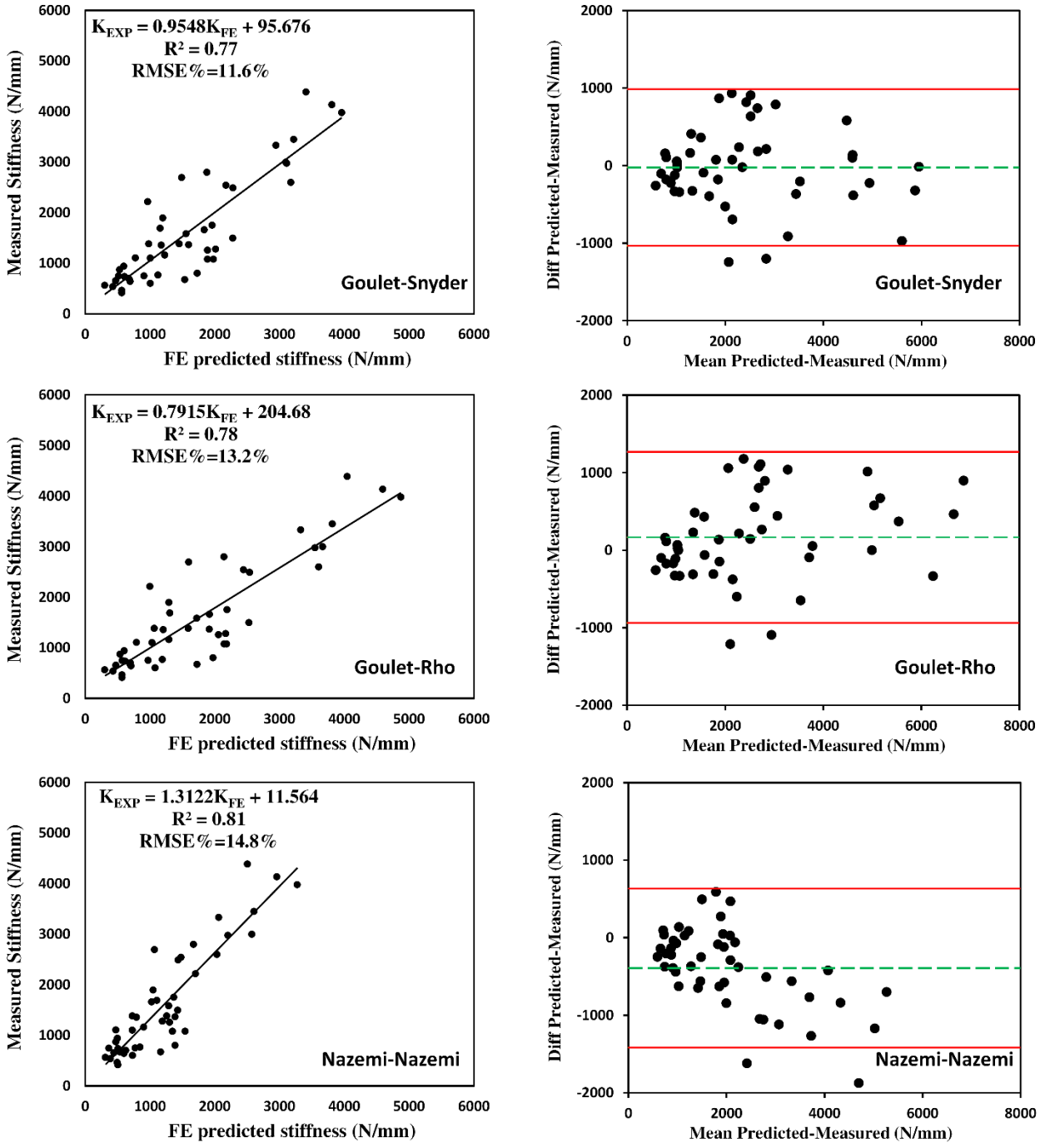

Figure 4-9. Linear regression analysis and Bland-Altman plots between FE-predicted and measured stiffness for continuum models with a global threshold (CMG) and different E-BMD equations evaluated in this study.

4.6 Discussion

This study presented a new technique (SM) for modeling laminar thin cortical structures. The predicted stiffness at the proximal tibial subchondral surface based on SM was evaluated in relation to continuum-based QCT-FE models with standard tissue separation algorithms (global threshold and image erosion) against *in-situ* stiffness measurements. It was observed that the performance of SM depended on the selected E-BMD relationship. SM modestly outperformed (2-3%) both global threshold and image erosion when cortical and trabecular bone modeled with Snyder and Goulet E-BMD equations, respectively. We did not observe any improvement from SM when it was applied alongside other E-BMD equations used in this study. The explained variance, and RMSE % of continuum QCT-FE models with a global threshold and image erosion was quite similar, with a global threshold method offering a slight improvement. Among evaluated density-modulus relationships, subchondral specific equations reported by Nazemi et al. explained the highest variance in experimentally measured stiffness, irrespective of the applied modeling approach.

Surprisingly, SM did not offer improved predictions of subchondral stiffness relative to continuum-based modeling methods. As opposed to the continuum modeling, the cortical bone was completely separated with SM via the semi-automatic segmentation with manual correction. Thereby, it was ensured that all cortical voxels were modeled using cortical-specific equations. In addition, SM allowed application of smaller elements at cortex and better resolved this region. The SM approach also prevented averaging of material properties in the meshing stage by separate modeling of cortical and trabecular structures. In general, apparent density of cortical bone varies between 1.2-1.8 g/cm^3 [17, 54, 55]. Within this density range, the difference in predicted E from cortical- and trabecular- specific E-BMD equations is several orders of magnitude. Similar stiffness predictions from SM and continuum-based QCT-FE models suggested that our defined subchondral bone via semi-automatic segmentation with manual correction contained voxels with BMD below the standard range reported for cortex. A density histogram of the image data at the segmented cortical region revealed that approximately seventy percent of voxels at the segmented cortical bone contained BMD lower than 0.4 g/cm^3 (APPENDIX – Figure A-2). Cortical and trabecular E-BMD equations start converging below this density range, and there is only a small difference (less than 3 GPa) in the predicted E from these equations. We believe the presence of low-density voxels in the cortical bone can be described by PV artifacts associated with low-

resolution clinical CT systems. The relatively large voxel size (0.5 mm) of the CT image could not resolve thin cortical structures at the subchondral surface (0.01-3.3 mm) [38-40]. Consequently, PV averaging between cartilage, cortex and trabecular bone resulted in low BMD voxels and blurred edges at the cortical region. These voxels appeared as low E elements in the FE model and adversely affected the predictive accuracy. Even though the SM better visualizes and models the cortical region compared to standard QCT-FE procedures, it is considered as a post-hoc analysis on the PV corrupted image and does not restore the intensity information at the PV layer. Hence, we believe that algorithms are required to retrieve the unblurred intensities at corrupted PV layers.

The continuum models were constructed with two different methods for tissue separation (image erosion & global threshold). The predictive accuracy of two models were similar, regardless of the employed E-BMD equation with a slight advantage to global thresholding. Neither of the methods was able to completely separate the cortical tissue. These methods also result in averaging of material properties in meshing stage due to their larger element size (0.9 mm) in relation to the cortical thickness. With the erosion approach, however, it was possible to restrict the detected cortical tissue to the bone periphery. As opposed to SM, both methods were performed in the material mapping stage and were relatively easy to implement. The time required for model implementation was less than that of SM as manual delimitation and assembly were not needed with continuum modeling procedures.

Among E-BMD equations evaluated in this study, subchondral specific equations by Nazemi et al. resulted in the highest R^2 for all modeling methods. The slope of the regression line between the SM predicted and measured stiffness and Bland-Altman plots indicated overestimation of stiffness for all E-BMD equations, except for Nazemi et al. This was expected as Nazemi's equations have been specifically derived for the subchondral region, whereas other equations were based on trabecular and cortical samples excised from epiphysis or metaphysis. The trabecular bone in these regions exhibited a higher degree of anisotropy (DA $\cong$ 4) with trabecular struts oriented along the longitudinal axis of the proximal tibia [43]. On the other hand, the subchondral trabecular bone exhibited a lower degree of anisotropy (DA $\cong$ 1.5) with dispersed trabecular orientation [45] and had higher BMD but lower E in the longitudinal direction. As such, extrapolating E-BMD equations specific to the epiphyseal and metaphyseal bone to the subchondral region gave higher E and resulted in stiffness overestimation. The calculated RMSE% in this study for Goulet-Snyder and Goulet-Rho was lower than the reported value in the literature

for FE-predicted stiffness from continuum models with same E-BMD equations (11.3% vs 19.4% for Goulet-Snyder and 13.2% vs 28.8% for Goulet-Rho) [109]. The predicted variance was also improved for both equations, 77% vs 75% for Goulet- Snyder and 78% vs 0.77% for Goulet-Rho [99, 109]. We also obtained higher errors for subchondral-specific equations compared to previous findings (14.8% vs 10.5%) [110]. These changes are most likely due to the different densitometric conversion equation used in this study. Specifically, the previous study employed an equation reported by Keyak [20] to convert between ash density and BMD, whereas here it was assumed that BMD and ash density were equal, as per [79, 81, 136]. This assumption altered the ρ_{QCT} threshold and thus altered the predictive accuracy of the QCT-FE model. Other studies with continuum QCT-FE models used global ρ_{QCT} thresholds ranging between 0.45-0.8 g/cm^3 to delineate between cortical and trabecular tissues in the tibia or femur [24, 27, 68, 104, 121, 139]. Given the substantial BMD variation in proximal tibial samples, it may be necessary to calculate an optimized conversion equation and a specific ρ_{QCT} threshold for each sample or even each indentation location.

It is important to consider the limitations of this study. First, the isotropic voxel size used in this study (0.5 mm) was relatively large with respect to the subchondral bone thickness (0.01-3.3 mm) [38, 39] and resulted in the PV averaging of voxels and blurred edges at the cortex. Obtaining small voxel sizes requires smaller x-ray beams accompanied with high beam energy flux or increasing the scanning time (exposure time). Both of these, however, would increase the radiation dose and would likely not be clinically feasible. With current clinical CT systems, it is not uncommon though to reconstruct voxel sizes as small as 0.33 mm [91, 149]. The smaller voxel size would better resolve thin laminar structures in the proximal tibia and lead to the higher contrast between tissues. Nevertheless, when our specimens were imaged (2008), 0.5 mm isotropic voxel size was gold standard for clinical CT systems. Second, we used simplified isotropic material properties for modeling the trabecular bone. Trabecular tissue though has been shown to be at least orthotropic in mechanical properties [10, 50, 66, 148]. More recent studies, however, found moderate improvements in QCT-FE predictions of local stiffness and surface strains by accounting for trabecular anisotropy [98, 99, 150]. Third, subchondral-specific equations by Nazemi et al. explained the highest variance as these equations were back-calculated for samples employed in this study [110, 151]. Accordingly, it is required to further validate these equations with new samples. Fourth, the integration approach that we used to assign E to elements resulted in a

constant E for each element and disrupted the material continuity within the element volume. Accounting for material variability inside elements may enhance the performance of QCT-FE models [117, 122, 144-146]. Nevertheless, given the small size of elements used in study (0.9 mm edge length), we do not believe that the difference in predicted variance would be large.

There were also some limitations related to mechanical tests performed earlier by Johnston et al [60]. First, the needle testing used to detect the subchondral surface may have been performed at regions with high porosity and/or low stiffness and led to inaccurate detection of the subchondral endplate. However, both visual tests and tactile feedbacks (e.g., ‘‘knocking” with blunt-ended forceps) verified the presence of cortical bone at indentation locations. Besides, imaged BMD values underneath detected indentation sites were in the range reported for cortex which further confirmed that indentation was performed at cortical regions. Second, needle testing may have imposed local plastic deformation at the subchondral surface and adversely affected stiffness measurements. Nevertheless, the localized deformation would be likely occurred surrounding the small needle tip and limited to the shallow depths beyond the subchondral surface. Moreover, cortical bone was later milled for 0.1 mm beyond the subchondral surface to create indentation sites, which would be also removed the damaged bone at the subchondral surface. Third, macro-indentation at one site may have damaged adjacent indentation locations and altered stiffness values. However, it has been shown that the damage is limited within 0.2 mm of the side of the indenter [61], which is much less than the distance between our defined indentations sites (at least 7 mm). Finally, indentation was performed on limited number of samples. More samples are required to further corroborate our findings.

In conclusion, our results showed that separate modeling of cortical bone offered little improvement in QCT-FE-predicted stiffness at the proximal tibial subchondral surface (0% to +3%). The performance of the SM approach was dependent on the adopted E-BMD relationship, and the subchondral-specific equations by Nazemi et al. described the highest variance in measured stiffness with low errors. Based on the results of this study, we cannot recommend the SM approach for future studies and continuum-based modeling methods can be still regarded as appropriate for QCT-FE modeling of skeletal structures. It is though useful to employ continuum modeling alongside the image erosion algorithm to restrict detected cortical tissue to the bone peripheral region. Also, visualized cortical bone via SM revealed that PV artifacts corrupted the

cortical voxels. Techniques are required to restore intensity information at the PV layer, which is the objective of our future research.

CHAPTER 5

5 EFFECT OF PARTIAL VOLUME CORRECTION

5.1 Introduction

Validation of QCT-FE models of subchondral bone has indicated moderate predictive accuracy [99, 109, 110]. This may be due to PV artifacts at the bone-cartilage interface, which results in blurring with CT images. The limited spatial resolution of clinical CT systems cannot resolve thin cortical structures as it has been shown that structures with thickness below 2.5 mm do not appear correctly within the CT image, with errors exceeding 100% for submillimeter cortices [31]. This is important because, with QCT-FE models, image blurring cause errors both in geometry construction and material assignment. Averaging E for elements at the PV layer results in an E which is equivalent to soft-tissue or low-density trabecular bone, leading to inaccurate QCT-FE models of cortical structures. This is key because the anatomical distribution of cortical bone is a critical component in determining the response of the subchondral surface to joint contact forces and mediates the structural integrity of the overlying cartilage [8, 110]. Continuum QCT-FE models based on thresholding methods are unreliable for modeling the cortex when the structure is thin in relation to imaging resolution. Several methods have been proposed in the literature for restoring intensity information at the corrupted PV layer. Recently, a sophisticated numerical method "deblurring" has been suggested that produces improved estimates of cortical thickness below 0.3 mm for the craniomaxillofacial cortical network (CMFS) [116, 120]. QCT-FE models of CMFS skeleton based on this algorithm enhanced correlation between FE-predicted and *in-vitro* measurements of local strains (R^2 from 73% to 86%) [114, 117]. It has been also suggested that intensity information at the PV layer could be restored based on characteristics of adjacent voxels unaffected by PV effects [117, 121]. The E at surface nodes has been also refined based on characteristics of inner nodes inside the FE model [122, 124]. Given the thickness of the PV layer at low resolution CT images, it may be also beneficial to refine E for all nodes located inside the PV layer. This can be accomplished by excluding PV corrupted voxels while mapping material properties from the CT lattice to the FE model.

The objective of this study was to evaluate QCT-FE predictions of stiffness acquired from different PV-corrected algorithms and original (uncorrected) images in relation to experimentally-derived *in-situ* stiffness.

5.2 Methods

5.2.1 Samples

The same specimens employed in Chapter 4 were used in this study.

5.2.2 Partial volume correction

Four different PV correction approaches were used to address PV artifacts at low-resolution CT images. The first approach employed blurred QCT images and used an image deblurring algorithm to address PV artifacts. The algorithm was applied to entire proximal tibia (Image Deblurring All, IDA). The second method applied the same algorithm but only to the cortical region (Image Deblurring Cortical, IDC). The third method also employed blurred QCT images, but in this case, an Image Remapping (IR) method was used to correct PV layers. The fourth algorithm addressed the PV layer while assigning mechanical properties from the CT lattice to an FE model. This method is referred to as Voxel Exclusion (VE), and is discussed in the FE modeling section of this chapter.

5.2.2.1 Image Deblurring All (IDA)

The image deblurring algorithm used in this study has been developed at the Sunnybrook Research Institute (University of Toronto), and integrated in open source image processing software 3D-Slicer [116, 120]. Theoretically, this technique can be used to improve the image quality of any image given that the point spread function (PSF) is uniformly distributed throughout the image. The deblurring method follows two main steps: (i) the intensity of cortical bone is assumed to be a rectangular function and a Gaussian PSF is estimated by minimizing the error between predicted and actual intensity pattern at the cortical region; and (ii) once the PSF is estimated, the image is deconvolved to retrieve non-blurred desired signal information. Using the deblurring module in 3D-Slicer, in-plane PSF was first estimated by sketching three 1D perpendicular lines across thin cortical segments in an arbitrary x-y plane (the sagittal plane in our case). It was ensured that selected cortical segment was thin and that the intensity was constant throughout the thickness so that the intensity profile could be modeled by a rectangular function. Once an in-plane PSF was estimated (σ_{xy}), the procedure was repeated in an arbitrary out-of-plane slice orthogonal to the x-

y plane to estimate the out-of-plane component of PSF (σ_z). Estimated PSF was later used in Richardson Lucy deconvolution [120, 123] in order to retrieve non-blurred intensity information for the whole image.

5.2.2.2 Image Deblurring Cortical (IDC)

Similar to IDA, non-blurred intensity information was initially obtained for the whole QCT image. In this case, however, deblurred data was used to model the cortical bone, whereas intensity information for trabecular bone was acquired based on the original CT image. A binary mask was created for the deblurred image using the half maximum height (HMH) method and region growing algorithm. Binary morphological operations (i.e., image erosion and Boolean subtraction) were employed to erode the binary mask with thickness of 3.5 mm [108] from the bone periosteal surface. We then detected cortical voxels within the eroded region with a global cutoff value of 500 mg/cm^3 [110]. The rest of voxels falling outside of the detected region were regarded as trabecular bone.

5.2.2.3 Image Remapping (IR)

Initially, original CT slices (Figure 5-1a) were segmented using the HMH method [107] to create a binary mask of the bony region. The PV-affected layer was eroded using the image erosion algorithm (3-by-3 structuring element) in the sagittal plane (Figure 5-1b). Boolean subtraction was then performed to create new binary masks for the PV layer and underlying bone. The BMD of the PV layer was calculated based on values of inner voxels which were presumably far enough from the corrupted PV layer. The K-nearest neighbors (KNN) algorithm [152] was adopted to find K closest neighbors to each voxel in the PV layer, and their BMD and distance were stored in separate matrices. The KNN algorithm identifies closets neighbors by calculating the Euclidian distance between the target voxel and adjacent voxels inside the bone, and returns corresponding BMD and distance values. The inverse distance weighting approach, with interpolation power of p [153], was then used to restore the PV layer by assigning a new BMD to each corrupted voxel (Figure 5-1c). The inverse distance weighting method was chosen to mitigate the effect of voxels located far from the cortical region as follows:

$$BMD_{corrected} = \frac{\sum_{i=1}^{K} BMD_i * 1/{d_i}^p}{\sum_{i=1}^{k} 1/{d_i}^p}$$

where $BMD_{corrected}$ is the new BMD value assigned to the PV-affected voxel, K is the number of adjacent voxels selected for BMD mapping, BMD_i is the BMD of the *ith* voxel, d_i is the Euclidean distance of the *ith* voxel from the target voxel, and p is the mapping coefficient which controls the degree to which the distance is weighted in interpolation.

Given the wide inter- and intra-thickness variation of the PV layer in the proximal tibia, it was not possible to determine the exact number of voxels corrupted with PV artifacts. Therefore, we eroded up to three layers (i.e., three voxels from the periosteal surface) and evaluated FE predictions in relation to measured stiffness. Similarly, we evaluated different values of K (10, 15, 20, 25 voxels) and p (2, 4, 6, 8) to reach the highest correlation between predicted and measured stiffness.

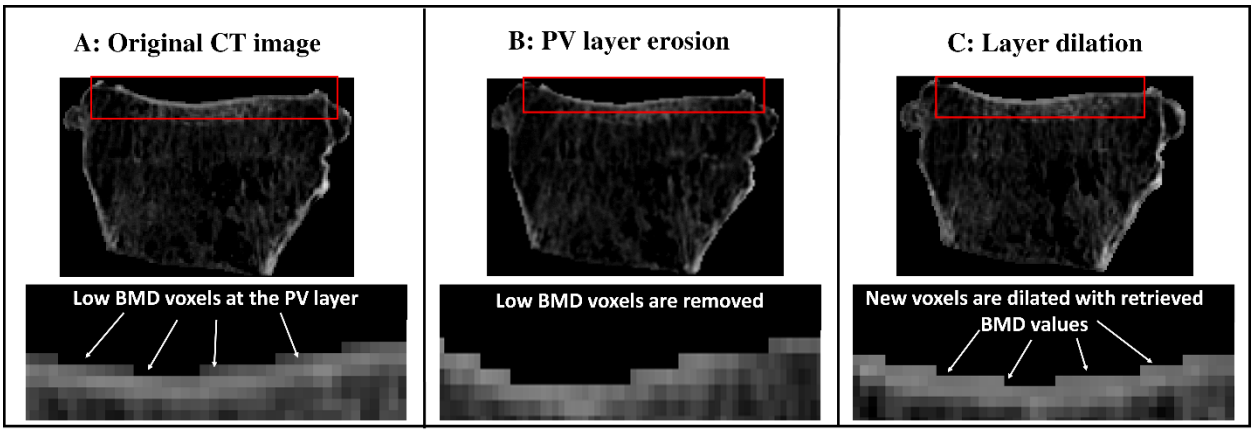

Figure 5-1. The process flow for correcting BMD at the PV layer using an Image Remapping approach (IR). The PV layer (a); was first eroded using morphological operators (b). The BMD at the PV layer was then restored based on characteristics of inner voxels unaffected by PV effects (c).

5.3 Model construction

The procedure for model construction is similar to steps presented in Chapter 4 of this thesis for continuum QCT-FE modeling. Five models of each proximal tibia were created in this study either based on PV-corrected or original CT images:

1. The first FE model of each proximal tibia was constructed based on intact original CT images (reference models).
2. The second FE model of each sample was constructed based on deblurred images using IDA (Figure 5-2).

3. The third model was constructed based on deblurred images using IDC.
4. The fourth model of each sample was constructed based on images obtained from IR.
5. The last FE model was constructed based on a new QCT-FE mapping approach, termed the Voxel Exclusion (VE) method, as described in 5.3.2.

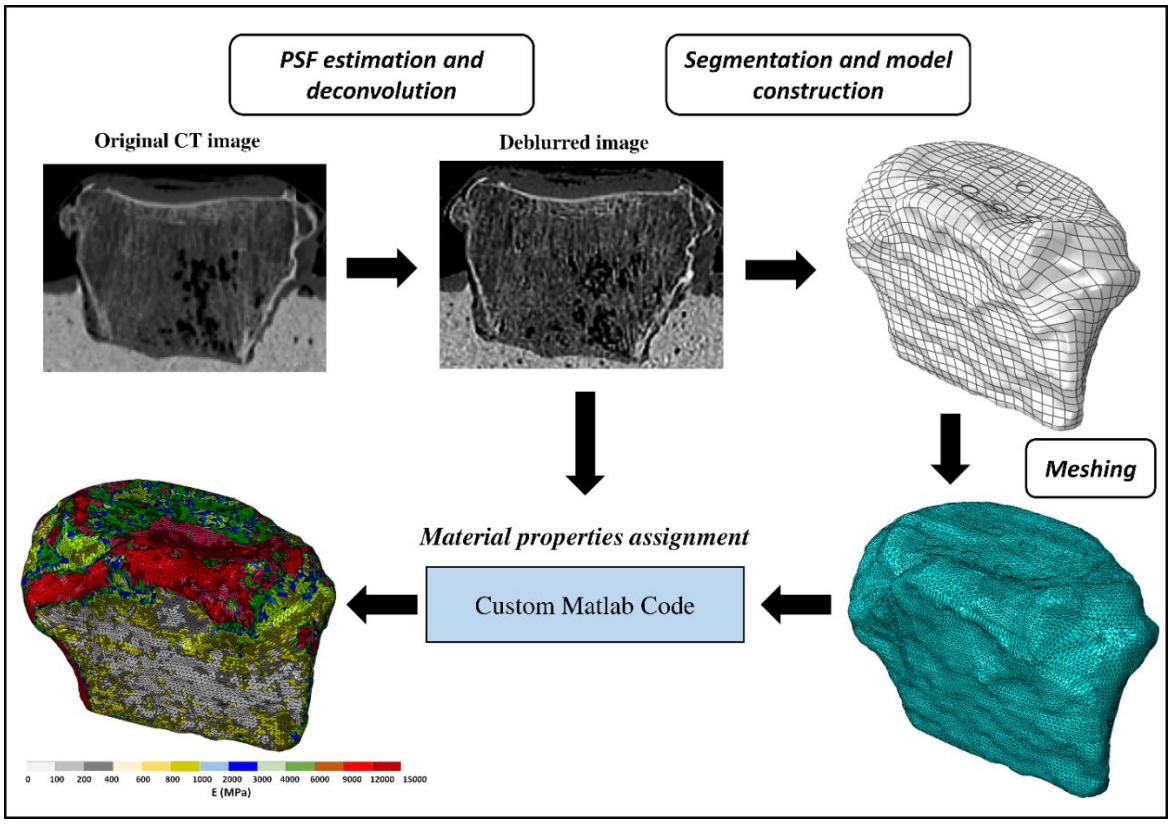

Figure 5-2. The methodological sequence used in this study to construct FE models out of deblurred images (IDA). The image was deblurred by the estimation of point spread function (PSF) for the CT system followed by the Richardson Lucy deconvolution. The deblurred image was then used to constructed FE models using standard procedures. Quadratic tetrahedral elements were used to discretize the model before mapping material properties from the CT image to the FE model.

5.3.1 Material definition

Nazemi's Subchondral specific equations for cortical ($31360\rho_{QCT}^{3}$ [110]) and trabecular bone ($820\rho_{QCT}$ [110]) were used to assign material properties from CT lattice data to the FE model. A global BMD threshold of 500 mg/cm^3 was used to distinguish between the cortical and trabecular tissue [110].

5.3.2 FE modeling-Voxel Exclusion (VE)

The voxel exclusion method (VE) allows PV correction in the material mapping stage and it is performed on intact original images. The model construction was similar to those described earlier for continuum QCT-FE modeling. The mapping, however, was performed such that PV corrupted voxels were excluded during integration (Figure 5-3). Image erosion and Boolean subtraction were used to erode the bone periosteal surface and create a binary mask for voxels located at the bone periphery (4 voxels equal to 2 mm). The visualized region contained low BMD cortical voxels affected by PV artifacts. The nodes located in the eroded region were identified, and their coordinate and number were stored in separate matrices. We subsequently determined voxels containing these nodes and a 1.5 mm^3 volume of interest (VOI) was defined surrounding each voxel. The elastic modulus of the target node was calculated by the interpolation of E at surrounding voxels (within VOI) via the inverse distance weighting approach and excluding voxels with an E less than the user-defined threshold (4 GPa, equal to cortical BMD of 500 mg/cm^3 [110]). If the VOI did not contain voxels above the user-defined threshold, the elastic modulus of 4 GPa was automatically assigned to the target node. The procedure repeated to assign E to all nodes of quadratic tetrahedral elements located at the eroded region. A constant E was then calculated for each element by the integration of elastic modulus field throughout the element volume. We followed standard procedures to assign E on nodes located outside of the eroded region (inside the bone): the elastic modulus of each node was calculated from the voxel containing that node, and a constant E was assigned to the element by integration.

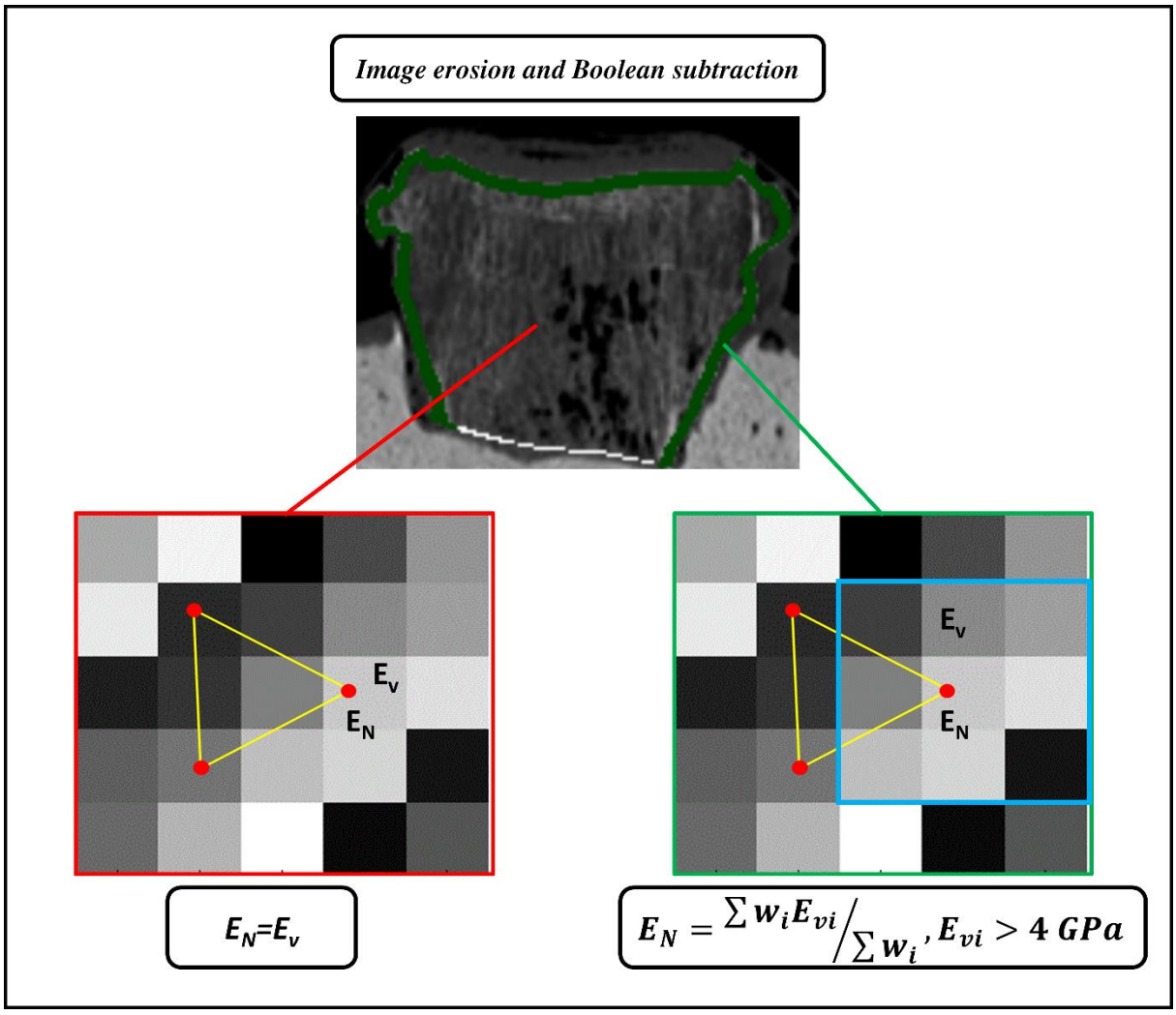

Figure 5-3. The procedure used in this study to address PV artifacts with voxel exclusion (VE). Image erosion and Boolean subtraction were used to detect 2 mm of bone tissue at the bone periphery. The nodes located inside the detected region were identified, and a 1.5 mm volume of interest (VOI) was defined surrounding each node (cyan square). The inverse distance weighting approach was then used to calculate the node elastic modulus (E_N) based on E of voxels located inside the VOI (E_V). Voxels with E less than 4 GPa were excluded from interpolation. The elastic modulus of nodes outside of the detected region (inside the bone) were calculated based on elastic modulus of the voxel containing that node.

5.4 Model validation

The calculated stiffness from reference models, IDA, IDC, IR, and VE were compared to measured stiffness in terms of R^2 and RMSE%.

5.5 Results

The reference model explained 81% of the measured stiffness variance with 12.4% error (Table 5-1 and Figure 5-4). The slope of the regression line between FE-predicted and measured stiffness was not significantly different from unity ($p > 0.05$). Bland-Altman plots (Figure 5-4) indicated an underestimation of stiffness (the mean difference was significantly different from zero, $p < 0.05$). The slope of the regression line fitted on the Bland-Altman plot did not show any systematic error (The slope was not significantly different from zero; $p > 0.05$).

The PV-corrected models with IDA explained 50% of measured stiffness variance with 76.4% error (Table 5-1 and Figure 5-5). The slope of the regression line was significantly different from unity ($p < 0.05$). The mean difference between FE-predicted and measured stiffness on Bland-Altman plot indicated stiffness overestimation ($p < 0.05$). The slope of the regression line fitted on the Bland-Altman plot indicated systematic overestimation ($p < 0.05$).

The IDC model explained 70% of measured stiffness variance with RMSE% of 23.3% (Table 5-1 and Figure 5-5). The slope of the regression line was significantly different from unity ($p < 0.05$). The Bland-Altman plots indicated that corresponding QCT-FE models overestimated measured stiffness, with increasing over-prediction at higher stiffness (mean difference and regression line slope both significantly different from zero, $p < 0.05$).

With the IR method, the erosion of one layer (one voxel) from the bone surface, and the values of K=20 voxels and p=6 resulted in the highest predictive accuracy, with R^2=81% and RMSE%=10.6% (Table 5-1 and Figure 5-5). The slope of the regression line was not significantly different from unity ($p > 0.05$). Bland-Altman plots indicated that corresponding QCT-FE models neither over- nor under-estimated measured stiffness ($p > 0.05$). The slope of the regression line in Bland-Altman plots was not significantly different from zero and did not show systematic errors ($p > 0.05$).

The VE approach provided the R^2 of 84% with 9.8% error (Table 5-1 and Figure 5-5). The slope of the regression line did not differ from unity ($p > 0.05$). Corresponding QCT-FE models neither over- nor under-estimated measured stiffness ($p > 0.05$). These models did not show any systematic errors ($p > 0.05$).

Table 5-1. R^2 and RMSE% for the reference and PV-corrected models. PV-corrected models were constructed based on different PV-correction algorithms including: Image Deblurring All (IDA), Image Deblurring Cortical (IDC), Image Remapping (IR), and Voxel Exclusion (VE).

Model	R^2	RMSE%
Reference	81%	12.4%
IDA	50%	76.4%
IDC	70%	23.3%
IR	81%	10.6%
VE	84%	9.8%

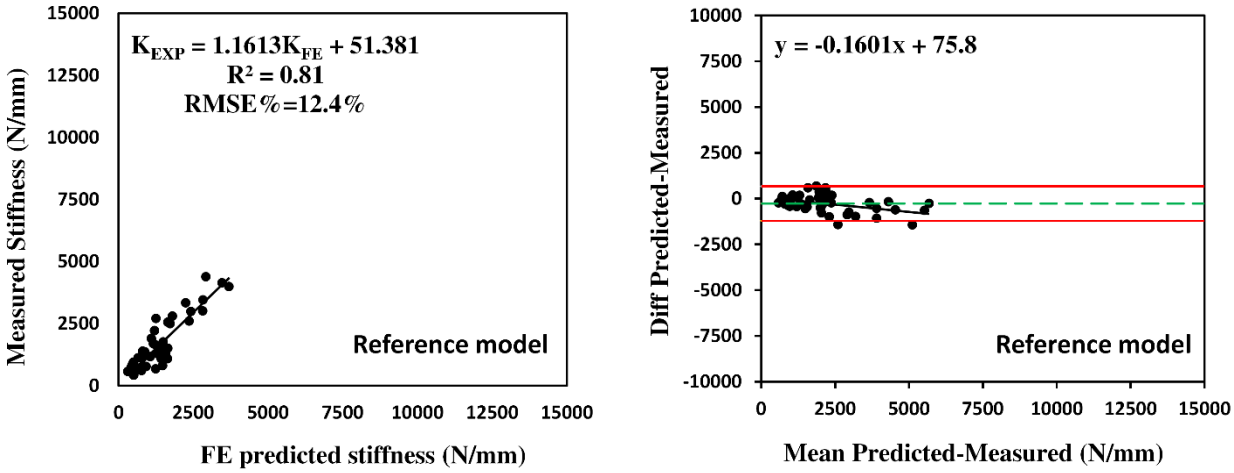

Figure 5-4. The linear regression analysis and Bland-Altman plot between FE-predicted and measured stiffness for the reference model.

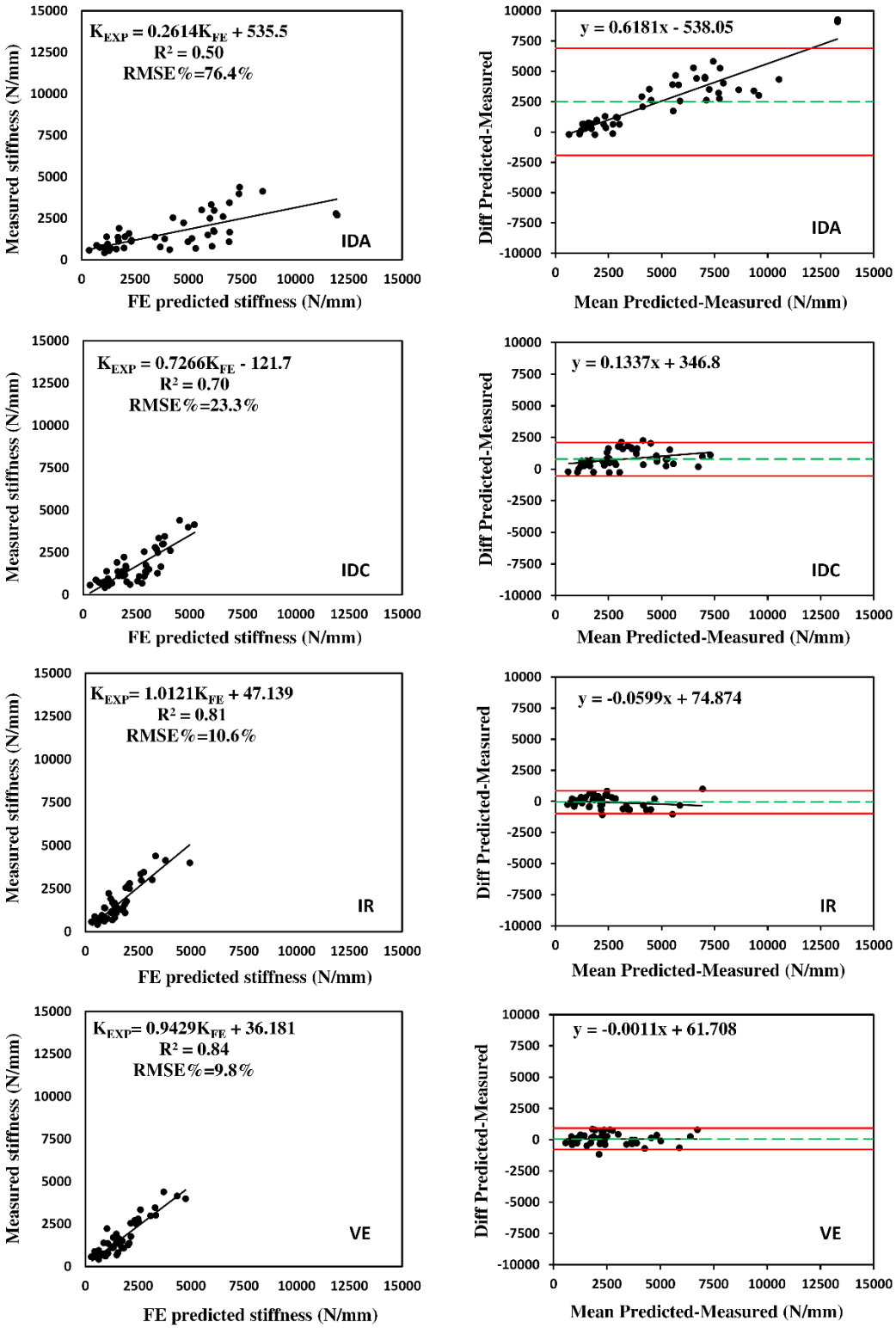

Figure 5-5. The linear regression analysis and Bland-Altman plot between FE-predicted and measured stiffness for different PV correction methods evaluated in this study; Image Deblurring All (IDA), Image Deblurring Cortical (IDC), Image Remapping (IR), and Voxel Exclusion (VE).

5.6 Discussion

This study evaluated different PV correction algorithms for QCT-FE modeling of local stiffness at the proximal tibia. Among algorithms evaluated in this study, exclusion of corrupted voxels while material mapping (VE) resulted in the highest predictions of measured stiffness for the following reasons: (1) this approach explained the highest variance in measured stiffness (R^2= 84%) with lowest errors (RMSE%=9.8%); (2) the slope of the regression line was not significantly different from unity; (3) the mean difference between FE-predicted and measured stiffness on the Bland-Altman plot was not significantly different from zero; (4) the slope of the regression line fitted on the Bland-Altman plot was not significantly different from zero.

Our results indicated that the reference model underestimated measured stiffness. This could be explained by incomplete modeling of the subchondral bone in reference models, which resulted in low E elements at thin cortical regions and negatively affected the predictive accuracy. Correcting PV artifacts resulted in increased stiffness predictions at the subchondral surface as the weak cortical bone at the PV layer was replaced with a denser bone. Our findings are aligned with previous research which outlined the importance of PV correction in low-resolution CT images [14, 28, 29, 115, 117, 120, 154, 155]. Of the different PV correction methods, IDA resulted in the lowest accuracy and significantly overestimated measured stiffness. This contradicts previous findings which showed improved predictions of local strains using the same algorithm for CMFS and femoral structures [28, 117]. IDA estimated the PSF based on characteristics of cortical bone. The optimized PSF was then used in deconvolution to deblur the whole bone structure including cortical and trabecular regions. The deblurred image of trabecular bone indicated densities which were higher than the range reported for trabecular bone in the literature (0.8-1.7 g/cm^3 vs 0.1-0.5 g/cm^3) [21, 110]. Given that we separated cortical and trabecular tissues with a global threshold of 500 mg/cm^3, all trabecular voxels were modeled with a cortical-specific equation which resulted in an E of 14-19 GPa. Stiffness at the proximal tibial subchondral surface is a structural property affected by both cortical and trabecular tissue, hence high densities at the trabecular region adversely affected FE-predicted stiffness at the subchondral surface. Conversely, the CMFS structure is comprised of thin cortical networks with trabecular bone forming only the small portion of the whole structure. Also, FE predictions at femoral bones were validated against *in-vitro* strain measurements at bone metaphysis and diaphysis which contained dense cortical regions and are less affected by properties of the trabecular bone. To address this issue, we modeled

trabecular bone based on the original CT image and used the deblurred image to extract density information of the cortical region via the IDC method. IDC provided improved predictive accuracy with R^2 of 70% and RMSE% of 23.3%. The performance of image deblurring method could be further improved by deriving an optimized PSF for trabecular bone and independently deconvolving cortical and trabecular structures.

The accuracy of the image remapping method (IR) was similar to the reference model (R^2=81% vs 81%) with slightly lesser errors (RMSE%= 10.6% vs 12.4%). As opposed to the reference model, this approach did not indicate any underestimation of stiffness. IR corrected the PV layer by mapping densities from adjacent voxels unaffected by PV artifacts. The thickness of PV layer used in image erosion, the number of voxels used for density mapping (K), and the power of interpolation (p) affected predictive accuracy acquired with this approach. These parameters, were evaluated independently. More robust optimization schemes (e.g., neural network and Nelder-Mead optimization [151]) could be performed to consider interaction effects between these parameters and derive optimal values. Optimization could also be performed on each proximal tibia independently to derive subject-specific values for each sample. Our findings are similar to previous studies which employed the same algorithm to address PV artifacts in CMFS and femoral structures though the improvements are small [117, 121]. Nevertheless, our results showed that this method had potential use for improved QCT-FE modeling of the subchondral bone region.

Voxel exclusion (VE) outperformed other models evaluated in the study. VE is a novel approach for PV correction which corrects PV layers in the mapping stage, hence this method does not require complex PV correction algorithms to be performed on CT data. VE moderately improved predictive accuracy (+3%) and resulted in the lowest RMSE% (9.8%). Similar algorithms have been presented in the literature to correct PV artifacts while material mapping. For instance, surface nodes were identified, and mechanical properties were assigned based on E of inner nodes [122, 124]. This approach, however, does not necessarily address PV artifacts in the FE model but more likely addresses geometrical uncertainties which result in surface nodes falling outside of the CT lattice. Here, we defined the binary mask for the cortical bone by 2 mm in-plane erosion of the bone periosteal surface. We then applied VE on nodes located in this region for PV correction. The thickness of the defined binary mask was relatively large in relation to thickness of cortex in the proximal tibia. This resulted in assigning a relatively high E on voxels

at the cortical-trabecular boundary. Nevertheless, the elastic modulus was the average of cortical and trabecular bone and close to the upper range of E reported for trabecular tissue (4 GPa) [33].

In addition to limitations outlined in Chapter 4, this study has limitations related to our element size, choice of E-BMD equations, physical validation, and the mapping strategy. First, we used a global element edge length of 0.9 mm to discretize our FE models. The 0.9 mm element edge length is high relative to thickness observed in the cortical region (0.01-3.3 mm) [38, 39] and might negate improvements from PV correction. It is possible to use automatic meshing algorithms with small elements at bone periphery and larger elements in the trabecular region. Though, when applying this meshing method on reference QCT-FE models, we did not observe any improvement in predictive accuracy. It is though necessary to evaluate this meshing algorithm along with PV corrected models in the future. The proposed separate modeling approach (SM) in Chapter 4 of this thesis could be also applied to address this limitation and is worth investigation in future studies. Second, we only used one set of E-BMD equation for modeling the cortical and trabecular bone and employed a single global threshold to differentiate between these regions. The performance of PV correction algorithms has been shown to be dependent on the adopted E-BMD relationship [121]. However, equations used in this study were specifically derived for the subchondral region [99], and we do not believe that using E-BMD equations specific to other anatomical sites will outperform subchondral specific equations. Nevertheless, optimizing E-BMD equations and a threshold value for each sample or each indentation location might enhance QCT-FE predicted stiffness at the subchondral surface. Third, we did not directly validate thickness and intensity of cortical bone acquired from different PV correction algorithms. It is required to do this using high-resolution images or standard phantoms. Our validation though was based on *in-situ* stiffness measurement at the subchondral surface, which was directly affected by properties of underlying cortical bone. Hence, this validation procedure provides an adequate metric for evaluating accuracy of acquired cortical segments. Fourth, the material mapping used in this study resulted in a constant E assignment for each element. The variation of elastic modulus across the element volume can be accounted by directly mapping an E on element integration points, which is the direction of our future study.

In conclusion, PV correction has potential to improve QCT-FE predictions of stiffness at the subchondral region. Among different PV correction algorithms compared in this study, excluding corrupted voxels during the material mapping stage (VE) led to the highest predictions of local

subchondral bone stiffness at the proximal tibia. However, more validation work is required to confirm the thickness and intensity profile of acquired cortical segments with high-resolution images. Further enhancement might be achieved by using smaller voxel sizes and automatic mesh generation algorithms with smaller elements.

CHAPTER 6

6 EFFECT OF MATERIAL MAPPING: A FEASIBILITY STUDY

6.1 Introduction

QCT-based FE modeling of human bones is increasingly used to study the biomechanical behavior of skeletal structures [27, 84, 102]. BMD is related to E using E-BMD relationships available in the literature [21], with E assigned to the FE model using a proper mapping method. The adopted mapping approach might alter mechanical properties of the FE model and, therefore it affects the overall predictive accuracy [156]. Early algorithms averaged the values at element nodes to calculate an element elastic modulus [133, 140]. This method resulted in ill-conditioned FE models when the element was larger than the voxel size. The second approach averaged E of voxels inside an element volume in order to assign a constant E to each element. This approach was fairly difficult to implement and increased the computation time [141]. A more recent method is to identify an E at element nodes and integrate the elastic modulus field throughout the element volume (referred to as constant-E method) [34]. This improved interpolation scheme has been shown to enhance the accuracy of FE-predicted strains in femoral bones [143]. We recently developed and validated QCT-FE models of the human proximal tibia to predict local subchondral bone stiffness (Chapter 4 & 5). We used the constant-E approach to assign mechanical properties to the FE model. While QCT-FE-predicted stiffness indicated good predictive accuracy in measured stiffness variance (R^2=84%, RMSE%=9.8%), it required a large number of elements to reconstruct the complex bone geometry and resolve heterogeneous mechanical properties, making these models rather impractical for clinical applications. One potential solution was to average elastic moduli within certain intervals (known as material binning) to reduce material groups within the FE package. Though, this resulted in averaging of E in elements and smoothed the mechanical properties. Also, application of the constant-E method disrupts continuity of material properties and may adversely affect the final predictive accuracy. More advanced mapping methods have been recently proposed to address these limitations by assigning mechanical properties directly to the element Gauss integration points (referred to as the Gauss-point method) [145, 146, 157]. This method may allow the application of larger elements by accounting for spatial variation of mechanical properties throughout the element volume. The approach has been

successfully validated against surface strain predictions with QCT-FE models of skeletal structures such as the pelvis and femur [145, 157-159]. However, it is unclear if this advanced mapping method can enhance the accuracy and convergence behavior of QCT-FE predicted stiffness at proximal tibial subchondral surface. The objective of this study was to evaluate convergence and accuracy of constant-E and Gauss-point mapping methods in relation to the experimentally measured stiffness at the proximal tibial subchondral surface.

6.2 Methods

6.2.1 Specimens

A selection of specimens were acquired from the dataset summarized in Chapter 4. Our previous findings indicated large variability in QCT-FE predicted stiffness with lateral compartments. Hence, for this study, four proximal tibia medial compartments were used (3 males and 1 female, age±SD: 77.7±5.1).

6.2.2 Finite element modeling

A smoothed volume was generated and imported into ABAQUS. FE models of tibial compartments were constructed using quadratic tetrahedral elements with uniform edge length ranging from 2.5 mm to 0.9 mm. Cortical and trabecular bone were modeled using the subchondral specific equations reported by Nazemi et al. [110] and separated using a global BMD threshold of 500 mg/cm^3. Two different material mapping strategies were used to import material properties from QCT images into FE models; (1) *Constant-E approach*: This approach was performed by modifying the ABAQUS source file (input file) using an in-house Matlab code. The FE nodal values were initially identified from voxels containing these nodes. The constant elastic modulus was subsequently calculated for the element by integrating the elastic modulus field throughout the element volume. The elastic modulus field was defined using element shape functions, and the integration was performed in volume coordinates for simplicity; and (2) *Gauss-point method:* With this approach, material properties were directly assigned to each Gauss integration point. As the number of Gauss points inside each element was more than one (four Gauss points for quadratic tetrahedral elements), the spatial variation of elastic modulus was accounted for. The elastic modulus at voxels was calculated and read into ABAQUS via user-defined subroutine (UEXTERNALDB) at the beginning of the analysis. The coordinates of element Gauss points were extracted using the "UMAT" subroutine. The elastic modulus at element Gauss points was

subsequently assigned from voxels containing these points. The "UMAT" subroutine was programmed in FORTRAN and stiffness, strain, and stress were calculated at each integration point via the static analysis.

6.3 Analysis

The convergence behaviour was assessed by determining the average absolute percent difference in stiffness between different element sizes. A difference less than 3% was set as the convergence limit [136]. The percent difference was calculated via:

$$\left(\sum \left|\frac{stiffness_{SMALL} - stiffness_{LARGE}}{stiffness_{LARGE}}\right|\right)/N$$

where $stiffness_{SMALL}$ and $stiffness_{LARGE}$ denote predicted stiffness at each indentation location with a small and large mesh size, respectively, and N is the number of indentation locations.

The calculated stiffness from different mapping methods was compared to measured stiffness in terms of R^2 and RMSE% to assess model accuracy.

6.4 Results

The average number of elements ranged between 35000 and 280000 for the coarsest and finest mesh, respectively. Figure 6-1 indicates the evolution of error calculated between consecutive mesh sizes. The constant-E approach converged with a mesh size of 1 mm with a percentage difference of 2.6%. The percentage difference for the Gauss-point method was continuously below 3% for edge lengths smaller than 2.5 mm. Hence, the edge length of 2 mm was deemed as the converged mesh size for these models. The RMSE% with respect to measured stiffness was ranging between 8.9%-13% and 8.5%-9.3% for constant-E and Gauss-point methods, respectively (Figure 6-2). The R^2 varied between 89%-91% and 90%-92% for constant-E and Gauss-point methods, respectively.

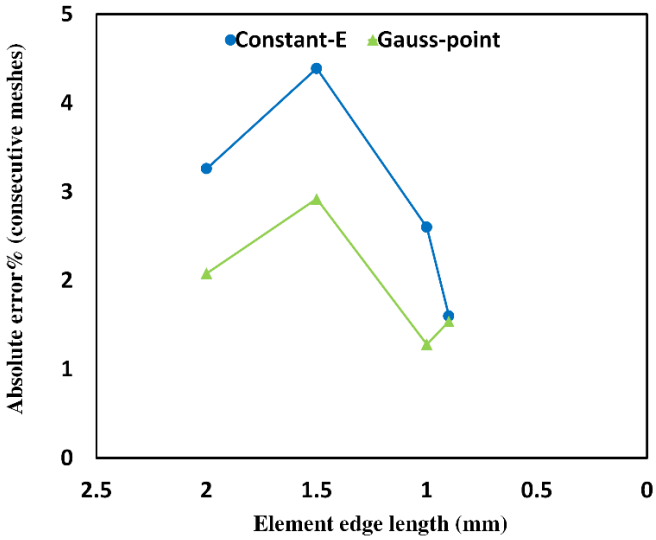

Figure 6-1. Average absolute percent difference between two consecutive mesh sizes for constant-E and Gauss-point models. The percentage of less than 3% was considered as the convergence criteria.

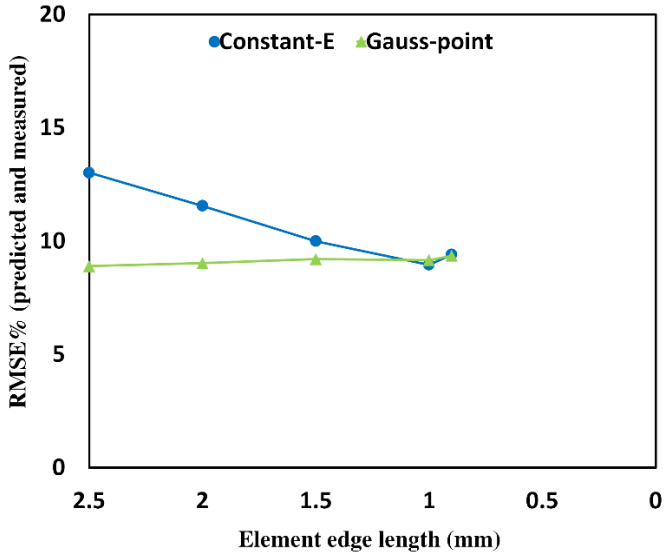

Figure 6-2. The root mean squared error (RMSE) between FE-predicted and measured stiffness normalized to the maximum measured stiffness (RMSE %) for different mesh sizes and mapping methods evaluated in this study.

6.5 Discussion

Two different mapping methods were used in this study to construct QCT-FE models of the human proximal tibia. The first method mapped material properties on FE nodes and assigned a constant value to each element. The second approach mapped an E directly on Gauss integration points. The predicted local stiffness from both models was compared to *in-situ* stiffness measurement to assess model accuracy. Both methods successfully predicted stiffness at the subchondral surface.

The constant-E and Gauss-point methods reached converged solution with the mesh size of 1 mm and 2 mm respectively. The computation time for the 2 mm mesh was an order of magnitude less than that of the 1 mm mesh size (30 min for 2 mm mesh size vs 180 min for 1 mm mesh size). Hence, Gauss-point approach has potential to reduce the computation cost for QCT-FE modeling of complex skeletal structures.

The predictive accuracy was similar for both methods at the converged mesh size. However, the Gauss-point method indicated a high degree of accuracy with a coarser mesh (2 mm vs 1 mm) and less computation time. This is more likely due to the continuity of mechanical properties inside the elements with the Gauss-point method which allows the FE model to capture abrupt material changes in the subchondral bone with larger elements. Our results are comparable with other studies which mapped mechanical properties directly to the element Gauss points and reported superior convergence and predictive accuracy of the Gauss-point method relative to the constant-E approach [145, 157-159].

Besides shorter computation time, there were also other advantages to assigning material properties to element Gauss point. First, model implementation was more straightforward as this approach took advantage of the FE solver subroutines and did not require custom programming. Second, with the Gauss-point method, both material mapping and the FE solution were carried out within the FE package, whereas with the constant-E approach it was required to first generate the main input file using an in-house code and then submit this new file for analysis in the FE package, which added to the overall analysis time. Third, Gauss point density could be altered without changing the mesh making the model modification easier. Fourth, the approach did not require material binning and prevented averaging of material properties in the FE model.

It is noteworthy to say that ABAQUS employs four Gauss points to derive the stiffness matrix for the quadratic tetrahedral element. This is the minimum number of Gauss points required for numerical integration to reach the exact solution. Increasing the number of Gauss points might

lead to converged results with larger elements. However, care should be taken to ensure that geometrical details are resolved with the employed coarser mesh.

In conclusion, our analysis showed that mapping material properties directly on Gauss integration points was a good surrogate for conventional constant-E methods. The approach reduced computational cost and reached higher predictive accuracy with large elements by accounting for material variability throughout the element volume. It is though required to conduct more validation studies with larger samples and on different structures to further assess the predictive accuracy.

CHAPTER 7

7 DISCUSSION

7.1 Overview of findings

Among non-invasive tools, QCT-FE models have indicated a high potential to measure the local structural stiffness of proximal tibia in living people [99, 109, 110]. When modeling bone at joint ends, however, limited resolution and relatively large voxel size of clinical CT systems make it challenging to resolve thin cortical regions leading to PV artifacts and low contrast between the cortical and trabecular bone. Hence, thin cortical areas do not appear correctly in the standard QCT-FE models [115, 117]. This research sought to address this problem.

A key accomplishment of **Chapter 4** (separate modeling of cortical and trabecular bone) was to present and validate a framework for segmentation and modeling of thin cortical structures to non-invasively predict local structural stiffness at the subchondral surface. Surprisingly, separate modeling offered little improvement in predicting variance in measured stiffness. Our results also indicated that the performance of this approach depended on employed E-BMD relationships, with the largest variance explained by subchondral-specific equations [110]. This research also indicated that continuum QCT-FE models based on thresholding could be regarded as sufficient for modeling long bones.

A key achievement of **Chapter 5** (effect of partial volume correction) was that we indicated that PV-correction has potential use for improving QCT-FE modeling of the subchondral bone region. Another accomplishment was the presentation of a new and convenient technique for PV correction at thin cortical regions of the subchondral bone, specifically the voxel exclusion (VE) method. Importantly, voxel exclusion method described the largest variance in measured stiffness and was relatively easy to implement when compared to the algorithms which restored the QCT image volume.

A key accomplishment of **Chapter 6** (effect of material mapping approach) was that we indicated the feasibility of the Gauss-point QCT-FE mapping technique for modeling subchondral bone stiffness. This approach accounted for the spatial variation of elastic modulus inside elements, and thereby converged with a larger mesh size. The predictive accuracy at the converged mesh was comparable to conventional mapping methods; though, the Gauss-point approach

achieved this accuracy with larger element sizes. This is important as QCT-FE models with larger elements require lesser computation time, making this technique a potential clinical research tool.

7.2 Comparison to existing findings

The previously mentioned depth-specific imaging method and continuum QCT-FE models are existing non-invasive tools to assess subchondral bone stiffness in the literature [46, 75]. Compared to depth-specific imaging method, QCT-FE models with partial volume correction improved stiffness prediction up to +17%.

PV-corrected QCT-FE models explained 50%-84% of the variance with RMSE% between 9.8% and 76.4%, depending on the employed algorithm for PV correction. There is no similar study in the literature for direct comparison. Nevertheless, our findings are aligned with studies performed on CMFS and femoral structures that indicated the importance of PV correction in thin cortical regions [28, 117].

Mapping the elastic modulus directly on element integration points enhanced convergence behavior and predictive accuracy of QCT-FE models. Compared to the constant-E method generally used with standard QCT-FE models, the Gauss-point approach converged with larger elements (2 mm vs 1 mm) and indicated comparable accuracy (in terms of R^2 and RMSE%) to the constant-E approach. The computation time for the Gauss-point method was less than constant-E approach (30 min vs 180 min). Our results indicated the high feasibility of Gauss-point approach and corresponding QCT-FE models in predicting subchondral bone stiffness at the proximal tibia. Our findings are aligned with previous research which reported the superior convergence behavior and accuracy of Gauss-point approach for modeling femoral and pelvic structures [145, 146, 157, 159].

7.3 Strengths and limitations

This research has several strengths. First, our defined SM approach was able to visualize the cortical region and ensured modeling of thin cortical structures with cortical-specific equations. SM also prevented averaging in meshing as the cortical and trabecular structures were modeled and meshed independently. The second strength of this thesis pertains to the broad evaluation of existing tissue separation and modeling methods to evaluate local structural stiffness at the proximal tibial subchondral surface. We evaluated three different tissue separation (semi-automatic segmentation with manual correction, global threshold, and image erosion) and two different modeling methods (separate modeling and continuum modeling) alongside three sets of

E-BMD relationships from the literature. To our best knowledge, this is the first study that directly compares different segmentation and QCT-FE modeling methods for studying structural properties in long bones. Third, visualizing the cortical bone allowed us to directly assess the density range in this structure. The existence of low-density voxels in our visualized region directed us to our second objective which aimed to correct PV artifacts at the cortical region. Fourth, we performed an extensive evaluation of existing PV correction algorithms and PV-corrected QCT-FE models in relation to standard modeling methods and *in-situ* stiffness measurements. Also, we proposed a new approach to correct PV artifacts at QCT-FE models constructed form low-resolution CT data: the Voxel Exclusion (VE) method. Our approach outperformed existing PV-correction methods and did not require sophisticated image processing analysis. Fifth, for the first time, we applied the element-based material mapping method to construct QCT-FE models of the proximal tibia. We indicated high feasibility of this approach in modeling local structural stiffness at the subchondral surface.

This thesis suffers from limitations not previously mentioned. First, we used a single threshold with continuum QCT-FE modeling to delineate between cortical and trabecular tissues for all our samples. The performance of E-BMD relationships is linked to the adopted cutoff value. Hence, optimizing the threshold value for each sample or each indentation location may lead to improved predictions of local stiffness at the proximal tibia. Though, it is unclear how this might be accomplished. Also, the threshold value pertains to the densitometric conversion equation between the ash density and BMD. Here, we assumed equivalence between these densities; though, the equation for each sample may vary depending on the amount of fat or blood at the bone tissue. We suggest deriving subject-specific conversion equation and threshold value for future studies (e.g., via the back calculation approach). Second, the image deblurring algorithm used in this study was specifically developed for CMFS structures. The PSF for the CT system was optimized based on characteristics of the cortical region and then used to deconvolve the whole image. This might be responsible for the observed out-of-range trabecular densities in the deblurred image. Optimizing PSF for trabecular bone and independent deconvolution of two regions may enhance the performance of image deblurring method in deblurring structures with significant trabecular bone such as the proximal tibia. Third, the density mapping method used in this study employed the inverse distance weighting interpolation to map densities from inner layers to the subchondral bone. The performance of the interpolation depended on several parameters (thickness of eroded

PV layer, number of adjacent voxels, and the power of interpolation). We altered individual settings to reach the highest R^2 between FE-predicted and measured stiffness. A more robust optimization scheme is required to consider interaction effects between parameters to derive subject-specific optimized values. Fourth, the thickness of bone tissue used in voxel exclusion method (4 voxels, 2 mm) was relatively large compared to the thickness of cortex at the subchondral surface, which resulted in the appearance of high E elements at the cortical-trabecular boundary. Nevertheless, the E was close to the upper range reported for the trabecular tissue in the literature (4 GPa) [15, 21, 110]. Finally, parameter settings for PV-correction algorithms were specifically adjusted for the samples used in this study. Applying the same methods on other set of samples may need specific parameter adjustments.

7.4 Conclusions

1- The proposed SM approach in this study for modeling cortical regions is time-consuming and offers little improvement in FE-predicted subchondral stiffness. Hence, standard procedures (continuum models with thresholding) could be still considered as acceptable for QCT-FE modeling of long bones.

2- Among evaluated PV correction algorithms in this study, the voxel exclusion method resulted in the highest explained variance and lowest errors for predicting stiffness at the subchondral surface. This method was easy to implement and did not require complicated image processing steps. We suggest using this algorithm in future studies to construct QCT-FE models of long bones.

3- The image deblurring algorithm is not efficient for correcting PV artifacts at the proximal tibia which is mostly comprised of trabecular tissue.

4- When compared alongside the standard constant-E mapping approach, the Gauss-point technique is an effective QCT-FE mapping method, and resulted in a high degree of accuracy and less computation time in predicting stiffness at the proximal tibial subchondral bone

7.5 Future work

1- In this study cortical and trabecular bone were differentiated using a single BMD threshold. It was observed that the choice of threshold altered the level of accuracy and errors obtained from different E-BMD equations. In future studies, it is necessary to derive threshold values specific to each sample or each indentation location. This can be performed using a

back calculation method against experimental measurements to achieve optimal threshold values.

2- The performance of image remapping method (IR) employed in this study depended on parameters used in interpolation (i.e., number of adjacent voxels and power of interpolation). We altered these parameters independently to achieve the highest correlation between FE-predicted and measured stiffness. Future work can derive optimized values using robust optimization techniques (e.g., Nelder-Mead).

3- In this study we used a global mesh size of 0.9 mm to discretize our models. This mesh size was relatively large compared to the cortical bone thickness at the subchondral region and may have negated improvements from PV correction. For future studies, we suggest the application of automatic meshing algorithms with small elements at bone periphery and larger elements inside the bone.

4- This study assumed isotropic mechanical properties for the trabecular bone. Previous research indicated moderate improvement in predictive accuracy when accounting for trabecular anisotropy [98, 99, 150]. However, previous anisotropic models were constructed with blurred images. For future studies, it worthwhile developing anisotropic models based on PV-corrected CT images.

5- This study validated QCT-FE models against *in-situ* stiffness measurements at the subchondral bone. It is unknown if developed QCT-FE models can represent full-field deformation inside the bone. Internal strains can be measured using image registration techniques such as Digital Volume Correlation (DVC). This method employs time-lapsed high-resolution images and seeks the affine transformation matrix between image stacks. DVC provides good experimental framework to estimate full-field strain distribution which could be then used to validate QCT-FE models. These measurements will shed more light on deformation mechanism at the proximal tibia and may lead to more robust QCT-FE models of bone at joint ends.

APPENDIX

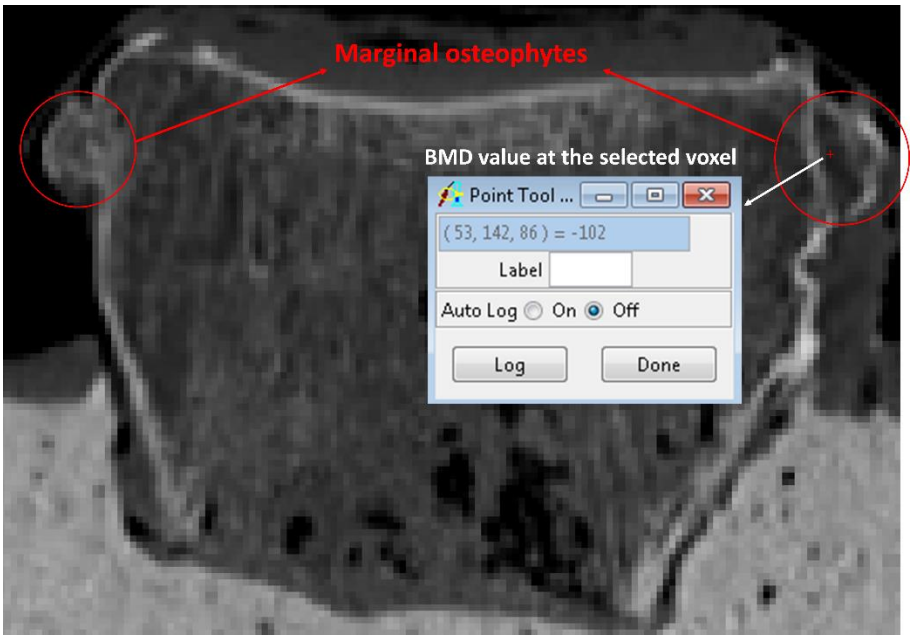

Figure A-1. Marginal osteophytes at the bone periphery. These regions contained voxels with negative BMD. The elastic modulus of 0.1 MPa was assigned to these voxels.

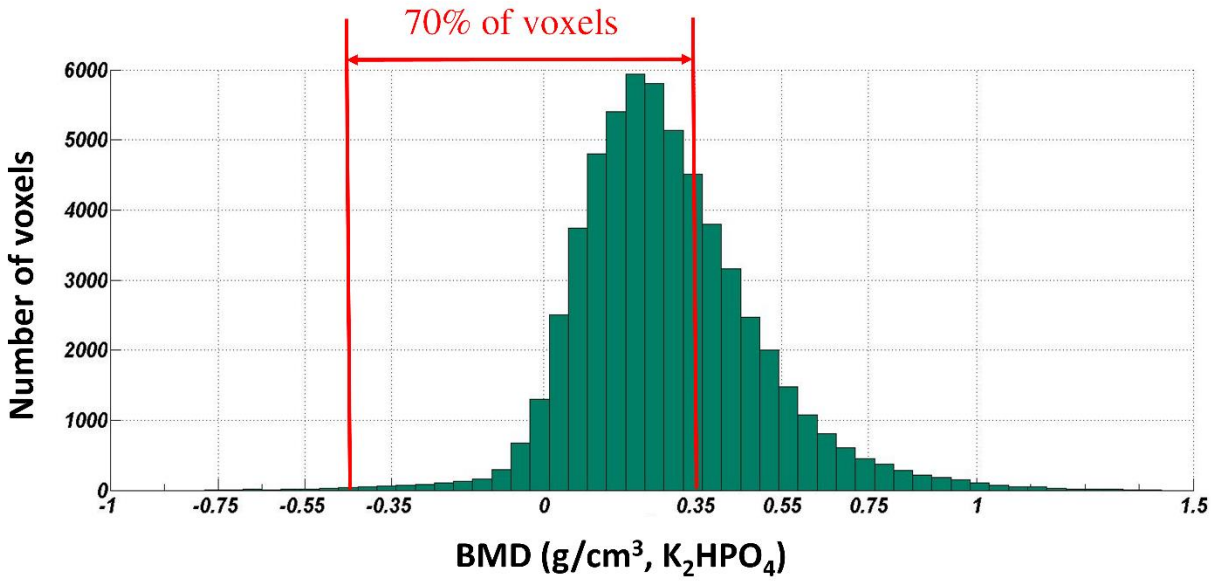

Figure A-2. The density histogram of segmented cortical regions delimitated via semi-automatic segmentation with manual correction. Approximately 70% of voxels had BMD values below 0.4 g/cm3. Voxels with negative BMD pertained to air and marginal osteophytes. These voxels were not included in E-BMD conversion, and their E was set as 0.1 MPa.

REFERENCES

1. Bone and Joint Canada. (http://boneandjointcanada.com/osteoarthritis/).
2. Charles G. Helmick, M., CDC Team, The Burden of Musculoskeletal Diseases in the United States. 2011.
3. Brandt, K.D., P. Dieppe, and E.L. Radin, Etiopathogenesis of Osteoarthritis. Rheumatic Disease Clinics of North America, 2008. 34(3): p. 531-559.
4. Goldring, S.R., Role of Bone in Osteoarthritis Pathogenesis. Medical Clinics. 93(1): p. 25-35.
5. Burr, D.B., Anatomy and physiology of the mineralized tissues: Role in the pathogenesis of osteoarthrosis. Osteoarthritis and Cartilage, 2004. 12, Supplement: p. 20-30.
6. Burr, D.B. and M.B. Schaffler, The involvement of subchondral mineralized tissues in osteoarthrosis: quantitative microscopic evidence. Microscopy research and technique, 1997. 37(4): p. 343-357.
7. Radin, E., I. Paul, and R. Rose, Role of mechanical factors in pathogenesis of primary osteoarthritis. The Lancet, 1972. 299(7749): p. 519-522.
8. Radin, E.L. and R.M. Rose, Role of subchondral bone in the initiation and progression of cartilage damage. Clinical orthopaedics and related research, 1986. 213: p. 34-40.
9. Burnett, W.D., et al., Knee osteoarthritis patients with severe nocturnal pain have altered proximal tibial subchondral bone mineral density. Osteoarthritis and Cartilage, 2015. 23(9): p. 1483-1490.
10. Zysset, P.K., M. Sonny, and W.C. Hayes, Morphology-mechanical property relations in trabecular bone of the osteoarthritic proximal tibia. The Journal of Arthroplasty, 1994. 9(2): p. 203-216.
11. Ding, M., et al., Changes in the stiffness of the human tibial cartilage-bone complex in early-stage osteoarthrosis. Acta Orthopaedica Scandinavica, 1998. 69(4): p. 358-362.
12. Au, A.G., et al., A NURBS-based technique for subject-specific construction of knee bone geometry. Computer Methods and Programs in Biomedicine, 2008. 92(1): p. 20-34.
13. Lengsfeld, M., et al., Comparison of geometry-based and CT voxel-based finite element modelling and experimental validation. Medical Engineering & Physics, 1998. 20(7): p. 515-522.

14. Szwedowski, T.D., et al., An optimized process flow for rapid segmentation of cortical bones of the craniofacial skeleton using the level-set method. Dentomaxillofacial Radiology, 2013. 42(4): p. 20120208.
15. Goulet, R.W., et al., The relationship between the structural and orthogonal compressive properties of trabecular bone. Journal of Biomechanics, 1994. 27(4): p. 375-389.
16. Rho, J.Y., M.C. Hobatho, and R.B. Ashman, Relations of mechanical properties to density and CT numbers in human bone. Medical Engineering & Physics, 1995. 17(5): p. 347-355.
17. Carter, D.R. and W.C. Hayes, The compressive behavior of bone as a two-phase porous structure. The Journal of Bone & Joint Surgery, 1977. 59(7): p. 954-962.
18. Linde, F., et al., Three-axial strain controlled testing applied to bone specimens from the proximal tibial epiphysis. Journal of Biomechanics, 1990. 23(11): p. 1167-1172.
19. Hodgskinson, R. and J.D. Currey, Young's modulus, density and material properties in cancellous bone over a large density range. Journal of Materials Science: Materials in Medicine, 1992. 3(5): p. 377-381.
20. Keyak, J., I. Lee, and H. Skinner, Correlations between orthogonal mechanical properties and density of trabecular bone: use of different densitometric measures. Journal of biomedical materials research, 1994. 28(11): p. 1329-1336.
21. Helgason, B., et al., Mathematical relationships between bone density and mechanical properties: A literature review. Clinical Biomechanics, 2008. 23(2): p. 135-146.
22. Yosibash, Z., et al., A CT-Based High-Order Finite Element Analysis of the Human Proximal Femur Compared to In-vitro Experiments. Journal of Biomechanical Engineering, 2006. 129(3): p. 297-309.
23. Yosibash, Z., N. Trabelsi, and C. Milgrom, Reliable simulations of the human proximal femur by high-order finite element analysis validated by experimental observations. Journal of Biomechanics, 2007. 40(16): p. 3688-3699.
24. Trabelsi, N., Z. Yosibash, and C. Milgrom, Validation of subject-specific automated p-FE analysis of the proximal femur. Journal of Biomechanics, 2009. 42(3): p. 234-241.
25. Trabelsi, N. and Z. Yosibash, Patient-Specific Finite-Element Analyses of the Proximal Femur with Orthotropic Material Properties Validated by Experiments. Journal of Biomechanical Engineering, 2011. 133(6): p. 061001-061001.

26. Venäläinen, M.S., et al., Importance of Material Properties and Porosity of Bone on Mechanical Response of Articular Cartilage in Human Knee Joint—A Two-Dimensional Finite Element Study. Journal of Biomechanical Engineering, 2014. 136(12): p. 121005-121005.
27. Venäläinen, M.S., et al., Effect of bone inhomogeneity on tibiofemoral contact mechanics during physiological loading. Journal of Biomechanics, 2016. 49(7): p. 1111-1120.
28. Falcinelli, C., et al., Can CT image deblurring improve finite element predictions at the proximal femur? Journal of the Mechanical Behavior of Biomedical Materials, 2016. 63: p. 337-351.
29. Treece, G.M., K.E.S. Poole, and A.H. Gee, Imaging the femoral cortex: Thickness, density and mass from clinical CT. Medical Image Analysis, 2012. 16(5): p. 952-965.
30. Dougherty, G. and D. Newman, Measurement of thickness and density of thin structures by computed tomography: A simulation study. Medical physics, 1999. 26(7): p. 1341-1348.
31. Prevrhal, S., et al., Accuracy of CT-based thickness measurement of thin structures: Modeling of limited spatial resolution in all three dimensions. Medical physics, 2003. 30(1): p. 1-8.
32. Kontulainen, S., et al., Analyzing Cortical Bone Cross-Sectional Geometry by Peripheral QCT: Comparison With Bone Histomorphometry. Journal of Clinical Densitometry, 2007. 10(1): p. 86-92.
33. Bessho, M., et al., Prediction of strength and strain of the proximal femur by a CT-based finite element method. Journal of Biomechanics. 40(8): p. 1745-1753.
34. Taddei, F., A. Pancanti, and M. Viceconti, An improved method for the automatic mapping of computed tomography numbers onto finite element models. Medical Engineering & Physics, 2004. 26(1): p. 61-69.
35. Nisell, R., et al., Tibiofemoral joint forces during isokinetic knee extension. The American Journal of Sports Medicine, 1989. 17(1): p. 49-54.
36. File: Knee medial view.gif. (2018, J.W.C., the free media repository. Retrieved 19:04, March 6, 2018 from https://commons.wikimedia.org/w/index.php?title=File:Knee_medial_view.gif&oldid=275824671.

37. Sophia Fox, A.J., A. Bedi, and S.A. Rodeo, The Basic Science of Articular Cartilage: Structure, Composition, and Function. Sports Health, 2009. 1(6): p. 461-468.
38. Milz, S. and R. Putz, Quantitative morphology of the subchondral plate of the tibial plateau. Journal of anatomy, 1994. 185(Pt 1): p. 103.
39. Yamada, K., et al., Subchondral bone of the human knee joint in aging and osteoarthritis. Osteoarthritis and Cartilage, 2002. 10(5): p. 360-369.
40. Clark, J. and J. Huber, The structure of the human subchondral plate. Bone & Joint Journal, 1990. 72(5): p. 866-873.
41. Radin, E.L. and J.L. Paul, Importance of Bone in Sparing Articular Cartilage from Impact. Clinical orthopaedics and related research, 1971. 78: p. 342-344.
42. Madry, H., C.N. van Dijk, and M. Mueller-Gerbl, The basic science of the subchondral bone. Knee Surgery, Sports Traumatology, Arthroscopy, 2010. 18(4): p. 419-433.
43. Ding, M., A. Odgaard, and I. Hvid, Changes in the three-dimensional microstructure of human tibial cancellous bone in early osteoarthritis. Bone & Joint Journal, 2003. 85(6): p. 906-912.
44. Li, B. and R.M. Aspden, Composition and mechanical properties of cancellous bone from the femoral head of patients with osteoporosis or osteoarthritis. Journal of Bone and Mineral Research, 1997. 12(4): p. 641-651.
45. Chappard, C., et al., Subchondral bone micro-architectural alterations in osteoarthritis: a synchrotron micro-computed tomography study. Osteoarthritis and Cartilage, 2006. 14(3): p. 215-223.
46. Johnston, J.D., B.A. Masri, and D.R. Wilson, Computed tomography topographic mapping of subchondral density (CT-TOMASD) in osteoarthritic and normal knees: methodological development and preliminary findings. Osteoarthritis and Cartilage, 2009. 17(10): p. 1319-1326.
47. Felson, D.T., Osteoarthritis of the Knee. New England Journal of Medicine, 2006. 354(8): p. 841-848.
48. Bailey, A.J. and J.P. Mansell, Do subchondral bone changes exacerbate or precede articular cartilage destruction in osteoarthritis of the elderly? Gerontology, 1997. 43(5): p. 296-304.
49. Radin, E.L., et al., Response of joints to impact loading — III. Journal of Biomechanics, 1973. 6(1): p. 51-57.

50. Maquer, G., et al., Bone Volume Fraction and Fabric Anisotropy Are Better Determinants of Trabecular Bone Stiffness Than Other Morphological Variables. Journal of Bone and Mineral Research, 2015. 30(6): p. 1000-1008.
51. Aigner, T. and L. McKenna, Molecular pathology and pathobiology of osteoarthritic cartilage. Cellular and molecular life sciences, 2002. 59(1): p. 5-18.
52. Anderson, M.J., J.H. Keyak, and H.B. Skinner, Compressive mechanical properties of human cancellous bone after gamma irradiation. The Journal of Bone & Joint Surgery, 1992. 74(5): p. 747-752.
53. Ciarelli, M., et al., Evaluation of orthogonal mechanical properties and density of human trabecular bone from the major metaphyseal regions with materials testing and computed tomography. Journal of Orthopaedic Research, 1991. 9(5): p. 674-682.
54. Snyder, S.M. and E. Schneider, Estimation of mechanical properties of cortical bone by computed tomography. Journal of Orthopaedic Research, 1991. 9(3): p. 422-431.
55. Rho, J.-Y., An ultrasonic method for measuring the elastic properties of human tibial cortical and cancellous bone. Ultrasonics, 1996. 34(8): p. 777-783.
56. Ashman, R., J. Rho, and C. Turner, Anatomical variation of orthotropic elastic moduli of the proximal human tibia. Journal of Biomechanics, 1989. 22(8): p. 895-900.
57. Ashman, R.B., J.D. Corin, and C.H. Turner, Elastic properties of cancellous bone: Measurement by an ultrasonic technique. Journal of Biomechanics, 1987. 20(10): p. 979-986.
58. Ashman, R.B., et al., A continuous wave technique for the measurement of the elastic properties of cortical bone. Journal of Biomechanics, 1984. 17(5): p. 349-361.
59. Yang, J.-P., et al., Stiffness of trabecular bone of the tibial plateau in patients with rheumatoid arthritis of the knee. The Journal of Arthroplasty, 1997. 12(7): p. 798-803.
60. Johnston, J.D., et al., Predicting subchondral bone stiffness using a depth-specific CT topographic mapping technique in normal and osteoarthritic proximal tibiae. Clinical Biomechanics, 2011. 26(10): p. 1012-1018.
61. Little, R.B., et al., A Three-Dimensional Finite Element Analysis of the Upper Tibia. Journal of Biomechanical Engineering, 1986. 108(2): p. 111-119.
62. Finlay, J.B., et al., Stiffness of bone underlying the tibial plateaus of osteoarthritic and normal knees. Clinical orthopaedics and related research, 1989(247): p. 193-201.

63. Harada, Y., H.W. Wevers, and T.D.V. Cooke, Distribution of bone strength in the proximal tibia. The Journal of Arthroplasty, 1988. 3(2): p. 167-175.
64. Bruyere, O., et al., Subchondral tibial bone mineral density predicts future joint space narrowing at the medial femoro-tibial compartment in patients with knee osteoarthritis. Bone, 2003. 32(5): p. 541-545.
65. Clarke, S., et al., Dual-energy X-ray absorptiometry applied to the assessment of tibial subchondral bone mineral density in osteoarthritis of the knee. Skeletal Radiology, 2004. 33(10): p. 588-595.
66. Zysset, P.K. and A. Curnier, An alternative model for anisotropic elasticity based on fabric tensors. Mechanics of Materials, 1995. 21(4): p. 243-250.
67. Schileo, E., et al., Subject-specific finite element models implementing a maximum principal strain criterion are able to estimate failure risk and fracture location on human femurs tested in vitro. Journal of Biomechanics, 2008. 41(2): p. 356-367.
68. Schileo, E., et al., Subject-specific finite element models can accurately predict strain levels in long bones. Journal of Biomechanics, 2007. 40(13): p. 2982-2989.
69. Taddei, F., et al., Subject-specific finite element models of long bones: An in vitro evaluation of the overall accuracy. Journal of Biomechanics, 2006. 39(13): p. 2457-2467.
70. Taddei, F., et al., Finite-Element Modeling of Bones From CT Data: Sensitivity to Geometry and Material Uncertainties. IEEE Transactions on Biomedical Engineering, 2006. 53(11): p. 2194-2200.
71. Grassi, L., et al., Accuracy of finite element predictions in sideways load configurations for the proximal human femur. Journal of Biomechanics, 2012. 45(2): p. 394-399.
72. Taddei, F., et al., Mechanical strength of a femoral reconstruction in paediatric oncology: a finite element study. Proceedings of the Institution of Mechanical Engineers, Part H: Journal of Engineering in Medicine, 2003. 217(2): p. 111-119.
73. Weinans, H., et al., Sensitivity of periprosthetic stress-shielding to load and the bone density–modulus relationship in subject-specific finite element models. Journal of Biomechanics, 2000. 33(7): p. 809-817.
74. Hayes, W.C., L.W. Swenson, and D.J. Schurman, Axisymmetric finite element analysis of the lateral tibial plateau. Journal of Biomechanics, 1978. 11(1): p. 21-33.

75. Amini, M., et al., Individual and combined effects of OA-related subchondral bone alterations on proximal tibial surface stiffness: a parametric finite element modeling study. Medical Engineering & Physics, 2015. 37(8): p. 783-791.
76. Cheung, A., et al., High-Resolution Peripheral Quantitative Computed Tomography for the Assessment of Bone Strength and Structure: A Review by the Canadian Bone Strength Working Group. Current Osteoporosis Reports, 2013. 11(2): p. 136-146.
77. Christen, D., D.J. Webster, and R. Müller, Multiscale modelling and nonlinear finite element analysis as clinical tools for the assessment of fracture risk. Philosophical Transactions of the Royal Society of London A: Mathematical, Physical and Engineering Sciences, 2010. 368(1920): p. 2653-2668.
78. Crawford, R.P., C.E. Cann, and T.M. Keaveny, Finite element models predict in vitro vertebral body compressive strength better than quantitative computed tomography. Bone, 2003. 33(4): p. 744-750.
79. Dragomir-Daescu, D., et al., Robust QCT/FEA Models of Proximal Femur Stiffness and Fracture Load During a Sideways Fall on the Hip. Annals of Biomedical Engineering, 2011. 39(2): p. 742-755.
80. Dragomir-Daescu, D., et al., Proximal Cadaveric Femur Preparation for Fracture Strength Testing and Quantitative CT-based Finite Element Analysis. 2017(121): p. e54925.
81. Dragomir-Daescu, D., et al., Quantitative computed tomography-based finite element analysis predictions of femoral strength and stiffness depend on computed tomography settings. Journal of Biomechanics, 2015. 48(1): p. 153-161.
82. Edwards, W.B. and K.L. Troy, Finite element prediction of surface strain and fracture strength at the distal radius. Medical Engineering & Physics, 2012. 34(3): p. 290-298.
83. Grassi, L., et al., How accurately can subject-specific finite element models predict strains and strength of human femora? Investigation using full-field measurements. Journal of Biomechanics, 2016. 49(5): p. 802-806.
84. Enns-Bray, W.S., et al., Material Mapping Strategy to Improve the Predicted Response of the Proximal Femur to a Sideways Fall Impact. Journal of the Mechanical Behavior of Biomedical Materials, 2017.
85. Austman, R.L., et al., The Effect of Distal Ulnar Implant Stem Material and Length on Bone Strains. The Journal of Hand Surgery, 2007. 32(6): p. 848-854.

86. Austman, R.L., G.J.W. King, and C.E. Dunning, Bone stresses before and after insertion of two commercially available distal ulnar implants using finite element analysis. Journal of Orthopaedic Research, 2011. 29(9): p. 1418-1423.
87. Doblaré, M. and J.M. García, Application of an anisotropic bone-remodelling model based on a damage-repair theory to the analysis of the proximal femur before and after total hip replacement. Journal of Biomechanics, 2001. 34(9): p. 1157-1170.
88. Schileo, E., et al., An accurate estimation of bone density improves the accuracy of subject-specific finite element models. Journal of Biomechanics, 2008. 41(11): p. 2483-2491.
89. Nazarian, A., et al., Quantitative micro-computed tomography: A non-invasive method to assess equivalent bone mineral density. Bone, 2008. 43(2): p. 302-311.
90. Les, C.M., et al., Estimation of material properties in the equine metacarpus with use of quantitative computed tomography. Journal of Orthopaedic Research, 1994. 12(6): p. 822-833.
91. Kersh, M.E., et al., Measurement of structural anisotropy in femoral trabecular bone using clinical-resolution CT images. Journal of Biomechanics, 2013. 46(15): p. 2659-2666.
92. Tabor, Z., et al., The potential of multi-slice computed tomography based quantification of the structural anisotropy of vertebral trabecular bone. Medical Engineering & Physics, 2013. 35(1): p. 7-15.
93. Tabor, Z. and E. Rokita, Quantifying anisotropy of trabecular bone from gray-level images. Bone, 2007. 40(4): p. 966-972.
94. Nazemi, S.M., D.M.L. Cooper, and J.D. Johnston, Quantifying trabecular bone material anisotropy and orientation using low resolution clinical CT images: A feasibility study. Medical Engineering & Physics, 2016. 38(9): p. 978-987.
95. Cowin, S.C., The relationship between the elasticity tensor and the fabric tensor. Mechanics of Materials, 1985. 4(2): p. 137-147.
96. Latypova, A., et al., Identification of elastic properties of human patellae using micro-finite element analysis. Journal of Biomechanics, 2016. 49(13): p. 3111-3115.
97. Van Rietbergen, B., et al., Direct mechanics assessment of elastic symmetries and properties of trabecular bone architecture. Journal of Biomechanics, 1996. 29(12): p. 1653-1657.

98. Enns-Bray, W.S., et al., Mapping anisotropy of the proximal femur for enhanced image based finite element analysis. Journal of Biomechanics, 2014. 47(13): p. 3272-3278.
99. Nazemi, S.M., et al., Accounting for spatial variation of trabecular anisotropy with subject-specific finite element modeling moderately improves predictions of local subchondral bone stiffness at the proximal tibia. Journal of Biomechanics, 2017. 59: p. 101-108.
100. Hollister, S.J., et al., Application of homogenization theory to the study of trabecular bone mechanics. Journal of Biomechanics, 1991. 24(9): p. 825-839.
101. Hollister, S.J., J.M. Brennan, and N. Kikuchi, A homogenization sampling procedure for calculating trabecular bone effective stiffness and tissue level stress. Journal of Biomechanics, 1994. 27(4): p. 433-444.
102. Michalski, A.S., W.B. Edwards, and S.K. Boyd, The Influence of Reconstruction Kernel on Bone Mineral and Strength Estimates Using Quantitative Computed Tomography and Finite Element Analysis. Journal of Clinical Densitometry, 2017.
103. Oliviero, S., et al., Effect of integration time on the morphometric, densitometric and mechanical properties of the mouse tibia. Journal of Biomechanics, 2017. 65(Supplement C): p. 203-211.
104. Eberle, S., M. Göttlinger, and P. Augat, An investigation to determine if a single validated density–elasticity relationship can be used for subject specific finite element analyses of human long bones. Medical Engineering & Physics, 2013. 35(7): p. 875-883.
105. Gray, H.A., et al., Experimental Validation of a Finite Element Model of a Human Cadaveric Tibia. Journal of Biomechanical Engineering, 2008. 130(3): p. 031016-031016.
106. Adams, R. and L. Bischof, Seeded region growing. IEEE Transactions on Pattern Analysis and Machine Intelligence, 1994. 16(6): p. 641-647.
107. Sven, P., E. Klaus, and A.K. Willi, Accuracy limits for the determination of cortical width and density: the influence of object size and CT imaging parameters. Physics in Medicine & Biology, 1999. 44(3): p. 751.
108. Edwards, W.B., T.J. Schnitzer, and K.L. Troy, Torsional stiffness and strength of the proximal tibia are better predicted by finite element models than DXA or QCT. Journal of Biomechanics, 2013. 46(10): p. 1655-1662.

109. Nazemi, S.M., et al., Prediction of local proximal tibial subchondral bone structural stiffness using subject-specific finite element modeling: Effect of selected density–modulus relationship. Clinical Biomechanics, 2015. 30(7): p. 703-712.
110. Nazemi, S.M., et al., Optimizing finite element predictions of local subchondral bone structural stiffness using neural network-derived density-modulus relationships for proximal tibial subchondral cortical and trabecular bone. Clinical Biomechanics, 2017. 41: p. 1-8.
111. Dall'Ara, E., et al., A nonlinear QCT-based finite element model validation study for the human femur tested in two configurations in vitro. Bone, 2013. 52(1): p. 27-38.
112. Keyak, J.H., et al., Prediction of femoral fracture load using automated finite element modeling. Journal of Biomechanics, 1997. 31(2): p. 125-133.
113. Nishiyama, K.K., et al., Proximal femur bone strength estimated by a computationally fast finite element analysis in a sideways fall configuration. Journal of Biomechanics, 2013. 46(7): p. 1231-1236.
114. Szwedowski, T.D., J. Fialkov, and C.M. Whyne, Sensitivity Analysis of a Validated Subject-Specific Finite Element Model of the Human Craniofacial Skeleton. Proceedings of the Institution of Mechanical Engineers, Part H: Journal of Engineering in Medicine, 2010. 225(1): p. 58-67.
115. Maloul, A., J. Fialkov, and C. Whyne, The Impact of Voxel Size-Based Inaccuracies on the Mechanical Behavior of Thin Bone Structures. Annals of Biomedical Engineering, 2011. 39(3): p. 1092-1100.
116. Pakdel, A., et al., Generalized method for computation of true thickness and x-ray intensity information in highly blurred sub-millimeter bone features in clinical CT images. Physics in medicine and biology, 2012. 57(23): p. 8099.
117. Pakdel, A., J. Fialkov, and C.M. Whyne, High resolution bone material property assignment yields robust subject specific finite element models of complex thin bone structures. Journal of Biomechanics, 2016. 49(9): p. 1454-1460.
118. Tuncer, M., U.N. Hansen, and A.A. Amis, Prediction of structural failure of tibial bone models under physiological loads: Effect of CT density–modulus relationships. Medical Engineering & Physics, 2014. 36(8): p. 991-997.

119. Gupta, S., et al., Development and experimental validation of a three-dimensional finite element model of the human scapula. Proceedings of the Institution of Mechanical Engineers, Part H: Journal of Engineering in Medicine, 2004. 218(2): p. 127-142.
120. Pakdel, A., et al., Model-based PSF and MTF estimation and validation from skeletal clinical CT images. Medical physics, 2014. 41(1).
121. Helgason, B., et al., The influence of the modulus–density relationship and the material mapping method on the simulated mechanical response of the proximal femur in side-ways fall loading configuration. Medical Engineering & Physics, 2016. 38(7): p. 679-689.
122. Helgason, B., et al., A modified method for assigning material properties to FE models of bones. Medical Engineering & Physics, 2008. 30(4): p. 444-453.
123. Ingaramo, M., et al., Richardson–Lucy Deconvolution as a General Tool for Combining Images with Complementary Strengths. ChemPhysChem, 2014. 15(4): p. 794-800.
124. Peleg, E., et al., Can a partial volume edge effect reduction algorithm improve the repeatability of subject-specific finite element models of femurs obtained from CT data? Computer methods in biomechanics and biomedical engineering, 2014. 17(3): p. 204-209.
125. Keyak, J.H., et al., Automated three-dimensional finite element modelling of bone: a new method. Journal of Biomedical Engineering, 1990. 12(5): p. 389-397.
126. Chen, Y., et al., Micro-CT based finite element models of cancellous bone predict accurately displacement once the boundary condition is well replicated: A validation study. Journal of the Mechanical Behavior of Biomedical Materials, 2017. 65: p. 644-651.
127. Zauel, R., et al., Comparison of the linear finite element prediction of deformation and strain of human cancellous bone to 3D digital volume correlation measurements. Journal of Biomechanical Engineering, 2006. 128(1): p. 1-6.
128. Bay, B.K., et al., Digital volume correlation: Three-dimensional strain mapping using X-ray tomography. Experimental Mechanics, 1999. 39(3): p. 217-226.
129. Basler, S., et al., Towards validation of computational analyses of peri-implant displacements by means of experimentally obtained displacement maps. Computer methods in biomechanics and biomedical engineering, 2011. 14(02): p. 165-174.
130. Jandejsek, I., O. Jiroušek, and D. Vavřík, Precise strain measurement in complex materials using Digital Volumetric Correlation and time lapse micro-CT data. Procedia Engineering, 2011. 10: p. 1730-1735.

131. Mirzaei, M., M. Keshavarzian, and V. Naeini, Analysis of strength and failure pattern of human proximal femur using quantitative computed tomography (QCT)-based finite element method. Bone, 2014. 64: p. 108-114.
132. Keyak, J.H., Improved prediction of proximal femoral fracture load using nonlinear finite element models. Medical Engineering & Physics, 2001. 23(3): p. 165-173.
133. Viceconti, M., et al., A comparative study on different methods of automatic mesh generation of human femurs. Medical Engineering & Physics, 1998. 20(1): p. 1-10.
134. Arjmand, H., et al., Finite element modeling of proximal tibial stiffness in normal and osteoarthritic knees: in vivo precision and preliminary comparisons. Osteoarthritis and Cartilage, 2016. 24, Supplement 1: p. S309-S310.
135. Polgar, K., M. Viceconti, and J. Connor, A comparison between automatically generated linear and parabolic tetrahedra when used to mesh a human femur. Proceedings of the Institution of Mechanical Engineers, Part H: Journal of Engineering in Medicine, 2001. 215(1): p. 85-94.
136. Cong, A., J.O.D. Buijs, and D. Dragomir-Daescu, In situ parameter identification of optimal density–elastic modulus relationships in subject-specific finite element models of the proximal femur. Medical Engineering & Physics, 2011. 33(2): p. 164-173.
137. Keller, T.S., Predicting the compressive mechanical behavior of bone. Journal of Biomechanics, 1994. 27(9): p. 1159-1168.
138. Morgan, E.F., H.H. Bayraktar, and T.M. Keaveny, Trabecular bone modulus–density relationships depend on anatomic site. Journal of Biomechanics, 2003. 36(7): p. 897-904.
139. Austman, R.L., et al., The effect of the density–modulus relationship selected to apply material properties in a finite element model of long bone. Journal of Biomechanics, 2008. 41(15): p. 3171-3176.
140. Merz, B., et al., Automated Finite Element Analysis of Excised Human Femora Based on Precision-QCT. Journal of Biomechanical Engineering, 1996. 118(3): p. 387-390.
141. Zannoni, C., R. Mantovani, and M. Viceconti, Material properties assignment to finite element models of bone structures: a new method. Medical Engineering & Physics, 1999. 20(10): p. 735-740.
142. Cody, D.D., et al., Short Term In Vivo Precision of Proximal Femoral Finite Element Modeling. Annals of Biomedical Engineering, 2000. 28(4): p. 408-414.

143. Taddei, F., et al., The material mapping strategy influences the accuracy of CT-based finite element models of bones: An evaluation against experimental measurements. Medical Engineering & Physics, 2007. 29(9): p. 973-979.
144. Kluess, D., et al., A convenient approach for finite-element-analyses of orthopaedic implants in bone contact: Modeling and experimental validation. Computer Methods and Programs in Biomedicine, 2009. 95(1): p. 23-30.
145. Chen, G., et al., A new approach for assigning bone material properties from CT images into finite element models. Journal of Biomechanics, 2010. 43(5): p. 1011-1015.
146. Chen, G., et al., Comparisons of node-based and element-based approaches of assigning bone material properties onto subject-specific finite element models. Medical Engineering & Physics, 2015. 37(8): p. 808-812.
147. Herzog, W., et al., Material and functional properties of articular cartilage and patellofemoral contact mechanics in an experimental model of osteoarthritis. Journal of Biomechanics, 1998. 31(12): p. 1137-1145.
148. Wirtz, D.C., et al., Critical evaluation of known bone material properties to realize anisotropic FE-simulation of the proximal femur. Journal of Biomechanics, 2000. 33(10): p. 1325-1330.
149. Larsson, D., et al., Assessment of Transverse Isotropy in Clinical-Level CT Images of Trabecular Bone Using the Gradient Structure Tensor. Annals of Biomedical Engineering, 2014. 42(5): p. 950-959.
150. Enns-Bray, W.S., et al., Morphology based anisotropic finite element models of the proximal femur validated with experimental data. Medical Engineering & Physics, 2016. 38(11): p. 1339-1347.
151. Nelder, J.A. and R. Mead, A Simplex Method for Function Minimization. The Computer Journal, 1965. 7(4): p. 308-313.
152. Friedman, J.H., J.L. Bentley, and R.A. Finkel, An algorithm for finding best matches in logarithmic expected time. ACM TOMS, 1977. 3: p. 209-226.
153. Shepard, D., A two-dimensional interpolation function for irregularly-spaced data, in Proceedings of the 1968 23rd ACM national conference1968, ACM. p. 517-524.
154. Treece, G.M., et al., High resolution cortical bone thickness measurement from clinical CT data. Medical Image Analysis, 2010. 14(3): p. 276-290.

155. Treece, G.M., et al., Predicting hip fracture type with cortical bone mapping (CBM) in the osteoporotic fractures in men (MrOS) study. Journal of Bone and Mineral Research, 2015. 30(11): p. 2067-2077.
156. Unnikrishnan, G.U. and E.F. Morgan, A New Material Mapping Procedure for Quantitative Computed Tomography-Based, Continuum Finite Element Analyses of the Vertebra. Journal of Biomechanical Engineering, 2011. 133(7): p. 071001-071001-8.
157. Shim, V.B., et al., Validation of an efficient method of assigning material properties in finite element analysis of pelvic bone. Computer methods in biomechanics and biomedical engineering, 2015. 18(14): p. 1495-1499.
158. Shim, V., et al., Finite element analysis of acetabular fractures—development and validation with a synthetic pelvis. Journal of Biomechanics, 2010. 43(8): p. 1635-1639.
159. Shim, V.B., et al., An Efficient and Accurate Prediction of the Stability of Percutaneous Fixation of Acetabular Fractures With Finite Element Simulation. Journal of Biomechanical Engineering, 2011. 133(9): p. 094501-094501-4.